

LOW VELOCITY IMPACT ANALYSIS OF A COMPOSITE MINI UNMANNED AIR
VEHICLE DURING BELLY LANDING

A THESIS SUBMITTED TO
THE GRADUATE SCHOOL OF NATURAL AND APPLIED SCIENCES
OF
MIDDLE EAST TECHNICAL UNIVERSITY

BY

SERHAN YÜKSEL

IN PARTIAL FULFILLMENT OF THE REQUIREMENTS
FOR
THE DEGREE OF MASTER OF SCIENCE
IN
AEROSPACE ENGINEERING

MAY 2009

Approval of the thesis:

**LOW VELOCITY IMPACT ANALYSIS OF A COMPOSITE MINI UNMANNED AIR
VEHICLE DURING BELLY LANDING**

submitted by **SERHAN YÜKSEL** in partial fulfillment of the requirements for the
degree of **Master of Science in Aerospace Engineering Department, Middle
East Technical University** by,

Prof. Dr. Canan Özgen
Dean, Graduate School of **Natural and Applied Sciences**

Prof. Dr. İsmail Hakkı Tuncer
Head of Department, **Aerospace Engineering**

Assoc. Prof. Dr. Altan Kayran
Supervisor, **Aerospace Engineering Dept., METU**

Examining Committee Members:

Prof. Dr. Nafiz ALEMDAROĞLU
Aerospace Engineering Dept., METU

Assoc. Prof. Dr. Altan KAYRAN
Aerospace Engineering Dept., METU

Asst. Prof. Dr. Melin ŞAHİN
Aerospace Engineering Dept., METU

Asst. Prof. Dr. Güçlü SEBER
Aerospace Engineering Dept., METU

Asst. Prof. Dr. Ferhat AKGÜL
Engineering Sciences, METU

Date:

I hereby declare that all information in this document has been obtained and presented in accordance with academic rules and ethical conduct. I also declare that, as required by these rules and conduct, I have fully cited and referenced all material and results that are not original to this work.

Name, Last Name : **Serhan YÜKSEL**

Signature :

ABSTRACT

LOW VELOCITY IMPACT ANALYSIS OF A COMPOSITE MINI UNMANNED AIR VEHICLE DURING BELLY LANDING

Yüksel, Serhan

M.Sc., Department of Aerospace Engineering

Supervisor: Assoc. Prof. Dr. Altan KAYRAN

May 2009, 118 pages

Mini Unmanned Aerial Vehicles (UAV) have high significance among other UAV's, in different categories, due to their ease of production, flexibility of maintenance, decrease in weight due to the elimination of landing gear system and simplicity of use. They are usually built to meet "hand launching" and "belly landing" criteria in order to have easy flight and easy landing features. Due to the hand take-off and belly landing features there is no need to have a runway and this feature is a very significant advantage in operational use.

In an operation belly landing mini UAV's may encounter tough landing areas like gravel, concrete or hard soil. Such landing areas may create landing loads which are impulsive in character. The effect of the landing loads on the airframe of the mini unmanned air vehicle must be completely understood and the mini UAV be designed accordingly in order not to damage the mini UAV during belly landing. Typical impact speeds during belly landing is relatively low (<10 m/s) and in general belly landing phenomenon can be treated as low velocity impact.

The purpose of this study is to analyze the impact loads on the composite sub-structures of a mini UAV due to the belly landing. "Güventürk" Mini UAV, which is designed and built in METU Aerospace Engineering Department, is used as the analysis platform. This study is limited to the calculation of stresses and deformation that is caused by the low velocity impact forces encountered during belly landing. The main purpose of this work is to help the designer in making design decisions for a mini UAV that is tolerable to low velocity impact loads.

Initial part of the thesis includes analytical treatment of low velocity impact phenomenon. In the simplified analytical approach the loading is assumed as quasi-static and comparisons of such a simplified method of analysis is made with explicit finite element solutions on isotropic and composite plate structures to investigate the applicability of simplified analytical method of analysis.

Belly landing analyses of the mini UAV are done by MSC.Dytran, which is an explicit finite element solver. Model building and post processing are done via MSC.Patran. Stress and deformation response of the mini UAV is investigated by performing low velocity impact analysis using sub-structure built-up approach.

Keywords: Unmanned air vehicle, low velocity impact, belly landing, composite structure

ÖZ

LOW VELOCITY IMPACT ANALYSIS OF A COMPOSITE MINI UNMANNED AIR VEHICLE DURING BELLY LANDING

Yüksel, Serhan

Yüksek Lisans, Havacılık ve Uzay Mühendisliği Bölümü

Tez Yöneticisi: Doç. Dr. Altan KAYRAN

Mayıs 2009, 118 sayfa

Mini İnsansız Hava Araçları (İHA) üretim kolaylığı, bakım esnekliği, iniş takımları olmadığı için düşük ağırlığı ve kullanım kolaylığı dikkate alındığında diğer İHA'lar arasında önemli bir yere sahiptir. Kolay uçuş ve kolay iniş özelliklerine sahip olmaları için genellikle elden atılıp gövde üstüne inerler. Elden atılıp gövde üstüne iniş yaptıkları için piste ihtiyaç duymamaları operasyonel kullanımları göz önünde bulundurulduğunda büyük bir avantajdır.

Operasyonel kullanımda gövde üstüne iniş yapan İHA'lar çakıl, beton ve sert toprak gibi zorlu iniş alanları ile karşılaşabilirler. Bu tip alanlar çok yüksek iniş yüklerini ortaya çıkarırlar. Gövde üstü iniş sırasında İHA'nın iskelet yapısına hasar vermemek için bu yükler tamamen anlaşılmalı ve mini İHA bu yüklere göre tasarlanmalıdır. Gövde üstü inişlerde çarpışma hızı genellikle düşüktür (<10 m/s) ve düşük hızda darbe kapsamında değerlendirilebilir.

Bu tezin amacı gövde üstü iniş esnasında bir mini İHA'nın kompozit parçaları üzerine binen yüklerin analizidir. Analizlerde ODTÜ Havacılık ve Uzay Mühendisliği

bölümünde tasarlanıp üretilen Güventürk Mini İHA kullanılmıştır. Bu tez gövde üstü iniş sırasında ortaya çıkan gerilim ve deformasyonun hesaplanması ile sınırlıdır. Tezin temel amacı tasarımcıya düşük hızlı çarpışma yüklerine dayanıklı bir mini İHA yapılmasında karar vermesine yardımcı olmaktır.

Tezin ilk bölümü düşük hızlı çarpışmanın analitik uygulamasını içermektedir. Basitleştirilmiş analitik yaklaşımda yükleme “neredeyse statik” kabul edilmiş ve elde edilen çözümler izotropik ve kompozit plakalar üzerinde uygulanan “açık-ekspilisit” sonlu eleman çözümü ile karşılaştırılarak basitleştirilmiş analitik yaklaşımın uygulanabilirliği incelenmiştir.

Düşük hızda çarpışma analizlerinde “açık-ekspilisit” sonlu elemanlar kodu olan MSC.Dytran kullanılmıştır. Modelleme ve sonuçların analizi için MSC.Patran kullanılmıştır. Mini İHA'nın stres ve deformasyon tepkileri alt elemanların birleşimi yaklaşımı ile incelenmiştir.

Anahtar Kelimeler: İnsansız hava aracı, düşük hızda çarpışma, gövde üstü iniş, kompozit yapı

to my family...

ACKNOWLEDGEMENTS

I would like to express the deepest gratitude for Assoc. Prof. Dr. Altan Kayran whose invaluable efforts and support guided me throughout my thesis. His friendly approach together with his encouragement is simply what one could wish from a supervisor. I am also thankful to Prof. Dr. Nafiz Alemdarođlu, supervisor of METU UAV Project for the financial and facility support he provided.

Many thanks to my colleagues at METU Aerospace Engineering UAV Laboratory: Fikri Akçalı, Sercan Soysal, Volkan Kargın and Hüseyin Yiđitler. I also thank to Murat Ceylan for his work during the manufacturing process of the UAV composite parts.

Finally, never enough thanks to my family for their trust.

TABLE OF CONTENTS

ABSTRACT	iv
ÖZ	vi
ACKNOWLEDGEMENTS	ix
TABLE OF CONTENTS.....	x
LIST OF FIGURES	xvi
LIST OF NOMENCLATURES	xxii
1. INTRODUCTION AND LITERATURE REVIEW	1
1.1. Introduction to Unmanned Aerial Vehicles	1
1.2. Classification of Unmanned Aerial Vehicles.....	1
1.3. METU “Güventürk” Mini Unmanned Aerial Vehicle	3
1.4. Impact Phenomenon	4
1.5. Composite Materials.....	6
1.6. Belly Landing UAV’s.....	7
1.7. Objective of the Study	8
2. LOW VELOCITY IMPACT LOAD AND STRESS ANALYSIS	10
2.1. Low Velocity Impact	10

2.2.	Determining the Impact Load by Considering the Low Velocity Impact as “Quasi-Static”	10
2.3.	Quasi-static Low Velocity Impact Analysis of Composite Laminates.....	16
3.	LOW VELOCITY IMPACT ANALYSIS WITH FINITE ELEMENT METHOD	19
3.1.	Implicit Method	19
3.2.	Explicit Method	21
3.3.	Comparison of Implicit and Explicit Methods	23
3.4.	MSC.Patran/Nastran	24
3.5.	MSC.Dytran.....	24
3.6.	Examples of Low/High Velocity Impact Problem Solutions	26
3.6.1.	Solutions with MSC.Nastran by assuming low velocity impacts; “quasi-static” case	27
3.6.2.	Explicit finite element solutions of low velocity impact problems with MSC.Dytran	35
3.6.3.	Comparison of quasi-static and explicit finite element solutions.....	36
3.7.	Impact Analysis of Composite Plates With Different Materials and Stacking Sequences	41
4.	DESIGN AND STRUCTURAL LAYOUT OF “GÜVENTÜRK” MINI UAV.....	45
4.1.	Description and Specifications.....	45
4.2.	Belly Landing.....	47
5.	LOW VELOCITY BELLY LANDING ANALYSIS OF “GÜVENTÜRK”	50

5.1.	Fuselage Finite Element Model	50
5.2.	Impact Modeling	53
5.3.	Fuselage Shell Landing Analysis On Rigid Surface	55
	Figure 42: Stress contours at t=0.027, t=0.035, t=0.044, t=0.053 (s).....	60
	Figure 43: Stress contours at t=0.062 t=0.071, t=0.080, t=0.089 (s).....	61
5.4.	Fuselage Shell Landing Analysis On Soil	63
5.5.	Fuselage Shell with Internal Structure Landing Analysis On Rigid Surface.	66
5.6.	Fuselage Shell and Internal Structure Landing Analysis On Soil	77
5.7.	Fuselage Shell and Internal Structure with Shell Wing Landing Analysis On Rigid Surface	78
5.8.	Fuselage Shell and Inner Structure with Shell Wing Landing Analysis (On Soil)	81
5.9.	Fuselage Shell and Internal Structure with Shell Wing and Internal Structure Landing Analysis On Rigid Surface.....	83
6.	CONCLUSION.....	88
6.1.	REVIEW OF RESULTS.....	88
6.2.	RECOMMENDATIONS	91
6.3.	FUTURE WORKS	91
	REFERENCES	93
	APPENDIX A: IMPORTING CAD MODEL INTO PATRAN	96

APPENDIX B: PATRAN LAMINATE MODELER TOOL	98
APPENDIX C: SOLUTION STEPS OF AN EXAMPLE PROBLEM.....	103
APPENDIX D: EFFECT OF MESH SIZE ON THE ANALYSIS.....	117
APPENDIX E: IMPACT VELOCITY VS. MAXIMUM DEFLECTION	118

LIST OF TABLES

Table 1: Classification of UAVs [3].....	2
Table 2 Values of Parameters m , r , and s	14
Table 3: Comparison of Implicit and Explicit Methods	23
Table 4: Iteration of P for $m=0.2\text{kg}$	30
Table 5: Iteration of P for $m=2\text{kg}$	30
Table 6: Iteration of P for $m=20\text{kg}$	31
Table 7: Maximum Deflection of Steel Plate for $m_{\text{ball}} = 2\text{kg}$	36
Table 8: Maximum Deflection of Steel Plate for $m_{\text{ball}} = 0.2\text{kg}$	37
Table 9: Maximum Deflection of Steel Plate for $m_{\text{ball}} = 20\text{kg}$	37
Table 10: Maximum Deflection of Composite Plate for $m_{\text{ball}} = 0.2\text{kg}$	41
Table 11: Material Properties of Carbon-Epoxy Woven	42
Table 12: Maximum Stress and Deflection Results of Test Case	43
Table 13: Maximum Stress and Deflection Results of Test Case - 2.....	44
Table 14: Specifications of “Güventürk” Mini UAV.....	46
Table 15 Units used in MSC.Patran Model	51
Table 16 Specifications of the analysis computer.....	55
Table 17 Typical durations of analysis for different cases	55

Table 18: Fuselage Model Properties (shell and internal structure).....	68
Table 19: Effective Maximum Stress for Various Stacking Sequence Sets	70
Table 20: Location of the points of maximum stress for each case	70
Table 21: Comparison of fuselage shell and fuselage with internal structure analysis	74
Table 22: Stress results for different mesh sizes.....	117

LIST OF FIGURES

Figure 1: Examples for Different UAV Types: (a) Micro, (b) Mini, (c) Tactical, (d) Medium Altitude Long Endurance (MALE), (e) High Altitude Long Endurance (HALE)	2
Figure 2 Hand launch (top) and belly landing of “Güventürk”	3
Figure 3: Scheme of Center Impact (left) Eccentric Impact (right)	4
Figure 4: Impact velocities of sample events [9].....	5
Figure 5: General Impact Case	12
Figure 6: Cross section of an N-layered laminate.....	17
Figure 7: Explicit Method Scheme [20].....	21
Figure 8: Time Step and Stress Waves Relationship	22
Figure 9: Cost of Methods for Various Cases [8].....	23
Figure 10: Lagrange Finite Element Technology – Elements of Constant Mass.....	25
Figure 11: Euler Finite Volume Technology – Elements of Constant Volume.....	25
Figure 12: Impactor and Target.....	26
Figure 13: Local and Overall Deformation of the Target.....	28
Figure 14: Calculation of Maximum Deflection of the Plate under 100N Load	30

Figure 15: Maximum Deflection for Concentrated Load, $P=88.8\text{N}$, $m=2\text{kg}$, $V=0.1\text{m/s}$	32
Figure 16: Maximum Deflection for Distributed Load, $P=88.8\text{N}$, $m=2\text{kg}$, $V=0.1\text{m/s}$.	32
Figure 17: Meshing of Distributed Load Case	33
Figure 18: Meshing of Distributed Load Case (detail)	33
Figure 19: Maximum Deflection for Concentrated Load, $P=0.38\text{N}$, $m=0.2\text{kg}$, $V=0.1\text{m/s}$	35
Figure 20: Sample screenshot from MSC.Dytran analysis	36
Figure 21: Comparison of Different Solution Methods for $m_{\text{ball}} = 2\text{kg}$	37
Figure 22: Comparison of Different Solution Methods for $m_{\text{ball}} = 0.2\text{kg}$	38
Figure 23: Comparison of Different Solution Methods for $m_{\text{ball}} = 20\text{kg}$	38
Figure 24: Z-Position vs. Time Graph for Steel Plate ($m=2\text{kg}$, $V=0.1\text{m/s}$)	40
Figure 25: Z-Position vs. Time Graph for Steel Plate ($m=2\text{kg}$, $V=10\text{m/s}$)	40
Figure 26: Comparison of Different Solution Methods for $m_{\text{ball}} = 0.2\text{kg}$	41
Figure 27: Carbon-Epoxy Plate Model	42
Figure 28: Low velocity impact model of a ball impactor on a target plate.....	43
Figure 29 “Güventürk” in operation	45
Figure 30: Solid Model of “Güventürk”	46
Figure 31: Schematic of spar and internal structure [25]	47
Figure 32: Belly Landing of “Güventürk”	49

Figure 33 Imported fuselage geometry and the principle axes	51
Figure 34: Meshed fuselage solid model.....	52
Figure 35: Meshed fuselage hollow model	52
Figure 36: The contact instant of impact case ($t=0.009$ s).....	54
Figure 37: Composite laminate layup for the left and right hand side of the body	56
Figure 38: Location of Element 6116	57
Figure 39: Stress (MPa) vs. Time (s) graph for Element 6116.....	58
Figure 40: Analyzed fuselage model at $t=0.04$ s and overlapped original form in wireframe.....	58
Figure 41: Stress contours at $t=0$, $t=0.009$, $t=0.018$ (s)	59
Figure 42: Stress contours at $t=0.027$, $t=0.035$, $t=0.044$, $t=0.053$ (s).....	60
Figure 43: Stress contours at $t=0.062$ $t=0.071$, $t=0.080$, $t=0.089$ (s)	61
Figure 44: Location and coordination of bottom (node 6515) and top (node 1774) nodes (coordinates in mm)	62
Figure 45: Z-Position (mm) vs. Time (s) graph for top (red), bottom (blue) nodes and ground (dashed line).....	63
Figure 46: z-position vs. time graph for top (red), bottom (blue) nodes and the level of ground (dashed line).....	65
Figure 47: Stress (MPa) vs. Time (s) graph for fuselage shell impact case.....	66
Figure 48: Stress contour of skin at $t=0.039$	66
Figure 49: Internal reinforcement added to the fuselage	67

Figure 50: Internal Structure - Fuselage Skin Association.....	68
Figure 51: Internal structure in the low opacity fuselage skin	68
Figure 52: Sample Excel File of Effective Stress Distribution	69
Figure 53: Stress (MPa) vs. time graph for best layup case ($[45]_{12}$)	73
Figure 54: Analyzed Fuselage and Internal Structure Model.....	73
Figure 55: Crush damage on the tail of the UAV	76
Figure 56: Stress (MPa) contour of the fuselage between $t = 0.033$ and $t = 0.055$..	77
Figure 57: Stress (MPa) vs. time graph for $[45]_{12}$ (rigid surface and soil model)	78
Figure 58: Analyzed Fuselage with Internal Structure and Shell Wing Model.....	79
Figure 59: Wing tip deflection (mm) vs. time (s) (for no spar case)	80
Figure 60 Vertical velocity of the wingtip	80
Figure 61: Stress (MPa) vs. time graph for $[45]_{12}$ (rigid surface and soil model)	81
Figure 62: Wingtip deflection vs. time (rigid and soil surfaces)	82
Figure 63: Stress contour graphs for $t=0$, $t=0.021$, $t=0.032$ (s)	82
Figure 64: Stress contour graphs for $t=0.041$, $t=0.052$, $t=0.062$, $t=0.075$ (s)	83
Figure 65: Internal structure of wing.....	84
Figure 66: Wingtip deflection vs. time (rigid surface)	84
Figure 67 Stress (MPa) vs. time graph for $[45]_{12}$ (rigid surface).....	85
Figure 68: Stress contours at $t=0$, $t=0.022$, $t=0.045$, $t=0.056$, $t=0.075$ (s).....	85
Figure 69: Location of maximum stress	86

Figure 70: Wing-fuselage junction nodes (dashed line).....	87
Figure 71: Importing IGES files, Screenshot -1	96
Figure 72: Importing IGES files, Screenshot -2	97
Figure 73: Importing IGES files, Screenshot -3	97
Figure 74: Laminate Modeler, Screenshot -1	98
Figure 75: Laminate Modeler Screenshot -2	99
Figure 76: Laminate Modeler Screenshot -3	100
Figure 77: Laminate Modeler Screenshot -4	100
Figure 78: Laminate Modeler Screenshot - 5	101
Figure 79: Laminate Modeler Screenshot – 6	101
Figure 80: Laminate Modeler Screenshot – 7	102
Figure 81: Solution steps, Screenshot -1	103
Figure 82: Solution steps, Screenshot -2	104
Figure 83: Solution steps, Screenshot -3	104
Figure 84: Solution steps, Screenshot -4	105
Figure 85: Solution steps, Screenshot -5	106
Figure 86: Solution steps, Screenshot -6	106
Figure 87: Solution steps, Screenshot -7	107
Figure 88: Solution steps, Screenshot -8	107
Figure 89: Solution steps, Screenshot -9	108

Figure 90: Solution steps, Screenshot -10	108
Figure 91: Solution steps, Screenshot -11	109
Figure 92: Solution steps, Screenshot -12	110
Figure 93: Solution steps, Screenshot -13	110
Figure 94: Solution steps, Screenshot -14	111
Figure 95: Solution steps, Screenshot -15	112
Figure 96: Solution steps, Screenshot -16	112
Figure 97: Solution steps, Screenshot -17	113
Figure 98: Solution steps, Screenshot -18	114
Figure 99: Solution steps, Screenshot -19	114
Figure 100: Solution steps, Screenshot -20	115
Figure 101: Solution steps, Screenshot -21	116
Figure 102: Solution steps, Screenshot -22	116
Figure 103: Impact Velocity (m/s) vs. Maximum Deflection Graph (m)	118

LIST OF NOMENCLATURES

$\bar{\mathbf{A}}$	Extensional stiffness matrix
A_{ij}	Components of extensional stiffness matrix
a_{plate}	Edge length of plate
a_n	Acceleration at step n
a_{n+1}	Acceleration at step n+1
a'_{n+1}	Estimated acceleration at step n+1
α	The distance that the impactor and the target approach one another
α_{max}	Maximum distance that the impactor and the target approach one another
$\dot{\alpha}$	Time derivative of α
$\ddot{\alpha}$	Time derivative of $\dot{\alpha}$
$\bar{\mathbf{B}}$	Coupling stiffness matrix
c	Speed of sound
\mathbf{C}	Damping matrix of the structure
δ_p	Deflection of plate
$\bar{\mathbf{D}}$	Bending stiffness matrix
d'_{n+1}	Estimated displacement at step n+1
d_n^*	Known value for displacement at step n
Δt	Time step
ε_i	Strain component in i-direction
F_{n+1}^{ext}	Vector of externally applied loads at step n+1
K_p	Spring constant of plate
\mathbf{K}	Stiffness matrix of the structure
k_1'	Parameter given by Equation (6)
k_2'	Parameter given by Equation (6)
L	Minimum element length

M	Mass matrix of the structure
m	Constant related to θ . (see Table 2)
m_1	Mass of impactor
m_2	Mass of target
N_i	In plane force in i-direction
n'	Parameter given by Equation (11)
P	Impact force
q_0	Peak value of distributed force on an elliptical area
Q_{ij}	Components of stiffness matrix in principle axes
\bar{Q}_{ij}	Components of stiffness matrix in laminate axes
r	Constant related to θ . (see Table 2)
ρ	Density
R_{1M}	1 st principle radius of curvature of impactor
R_{1m}	2 nd principle radius of curvature of impactor
R_{2M}	1 st principle radius of curvature of target
R_{2m}	2 nd principle radius of curvature of target
S	Safety factor
s	Constant related to θ . (see Table 2)
σ_i	Stress component in i-direction
τ_{ij}	Shear stress component in ij-direction
u	Position variable
u_n	Position at step n
u_{n+1}	Position at step n+1
\dot{u}	Time derivative of u
\dot{u}_n	Time derivative of u_n
\dot{u}_{n+1}	Time derivative of u_{n+1}
\ddot{u}	Time derivative of \dot{u}
\ddot{u}_n	Time derivative of \dot{u}_n
\ddot{u}_{n+1}	Time derivative of \dot{u}_{n+1}

V'_{n+1}	Estimated velocity at step n+1
V_n^*	Known value for velocity at step n
v_1	Poisson's Ratio of impactor
v_2	Poisson's Ratio of target
V_1	Velocity of impactor
V_2	Velocity of target
V	Initial relative velocity of impactor
w_{\max}	The highest eigenvalue in the system
ξ	Fraction of critical damping in the highest mode

CHAPTER 1

INTRODUCTION AND LITERATURE REVIEW

1.1. Introduction to Unmanned Aerial Vehicles

Unmanned Aerial Vehicle (UAV), as the name implies, are operated autonomously or remotely, and they are used for reconnaissance purposes, as target/drone, or as experimental platform for research/development. Nowadays their civil use and military use is rapidly increasing. For instance it is claimed that in the future all the fighter aircraft will be unmanned. The roots of UAVs are the very first Remote Piloted Vehicles (RPV) in the beginning of 20th century [1]. During Second World War UAVs are used to train AA Gunners. After 1950, design and production of UAVs is accelerated and nowadays there are a number of classes of UAVs. Low cost, multipurpose capability and keeping human away from the danger zones are the most important reasons why UAV's have become so popular. Current demand on the UAV platforms and ongoing research activities into UAVs also show that in the next 15 years there will be more unmanned platforms operating in the fields. [2]

1.2. Classification of Unmanned Aerial Vehicles

Mission profile is an important parameter that can be used to classify UAVs. The duration they can operate without landing and the distance they can go is closely related to their gross weight. Flight altitude is also a significant parameter and takes place in classification. According to Unmanned Vehicle Systems International [3] the classification of UAVs is given in Table 1. Figure 1 displays some examples of unmanned air vehicle.

Table 1: Classification of UAVs [3]

UAV CATEGORIES	Range (km)	Flight Altitude (m)	Endurance (hour)	Maximum Take-Off Weight (MTOW)
Tactical UAV				
Micro	<10	250	1	<5
Mini	<10	150-300	<2	<30
Close Range Tactical	10-30	3000	2-4	150
Short Range Tactical	70-200	5000	3-6	200
Medium Range	>500	14000	6-10	1250
Medium Range Endurance	>500	8000	10-18	1250
Low Altitude Deep Penetration	>250	50-9000	0.5-1	350
Low Altitude Long Endurance	>500	3000	>24	<30
Medium Altitude Long Endurance	>500	14000	24-48	1500
Strategic UAV				
High Altitude Long Endurance	>2000	20000	24-48	12000
Special Purpose UAV				
Unmanned Combat Aerial Vehicle	approx. 1500	10000	approx. 2	10000
Lethal	300	4000	3 to 4	250
Decoy	0 to 500	5.000	< 4	250
Stratospheric	> 2000	>20000 & <30000	> 48	TBD
Exo-stratospheric	TBD	> 30000	TBD	TBD
Space	TBD	TBD	TBD	TBD

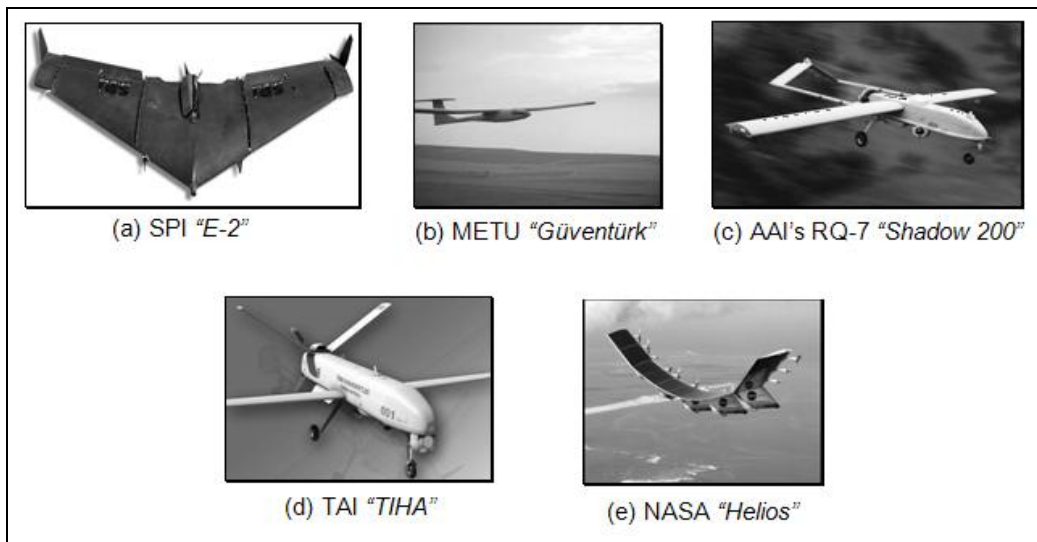


Figure 1: Examples for Different UAV Types: (a) Micro, (b) Mini, (c) Tactical, (d) Medium Altitude Long Endurance (MALE), (e) High Altitude Long Endurance (HALE)

1.3. METU “Güventürk” Mini Unmanned Aerial Vehicle

METU “Güventürk” Mini UAV System is designed and built in METU Aerospace Engineering Department UAV Laboratories with the financial support of State Planning Organization in 2005. With embedded original autopilot system, “Güventürk” is capable of flying autonomously and accomplishing a reconnaissance mission. Hand launching, extremely low noise signature and belly landing features of “Güventürk” make it easy to operate in the field.

METU Mini UAV has duration of 1 hour and minimum 10 km of operational range. Real time continuous telemetry data allows a clear view of the field from above. The wingspan is 220 cm and MTOW is about 4.5 kg. Two photographs of “Güventürk” during hand launch and belly landing are shown in Figure 2. More information about “Güventürk” is given in Chapter 4.



Figure 2 Hand launch (top) and belly landing of “Güventürk”

1.4. Impact Phenomenon

Impact is a transient physical excitation and causes a force to be applied for a very short period of time. When two bodies come into contact together with some velocity a certain amount of impulse arises at the contact zone in both bodies. For the impact of particles impulse is normal to the particles' contact plane. However, for more complex bodies there is a region of contact through which the impact loads are induced on the impactor and the target material, and deformation on both bodies occur due to the impact [4]. Impulse forces on this deformed surface are associated so that there is no interpenetration of the bodies. In other words, forces prevent overlapping of bodies.

A sample drawing of center impact and eccentric impact is given in Figure 3. In a general impact case between two bodies B and B', the term "incidence" refers to the moment at which a point C on the body B is in contact with a point C' on the body B'. Incidence time is the initial instant of the impact. If at least one of the two bodies have a smooth surface at C or C', there is a tangential plane passing through C and/or C'.

Referring to Figure 3, if r_c is the vector from G to C and $r_{c'}$ is the vector from G' to C'; the impact is called "Center Impact" if r_c and $r_{c'}$ are perpendicular to the tangential plane. Otherwise, the impact phenomenon is called "Eccentric Impact".

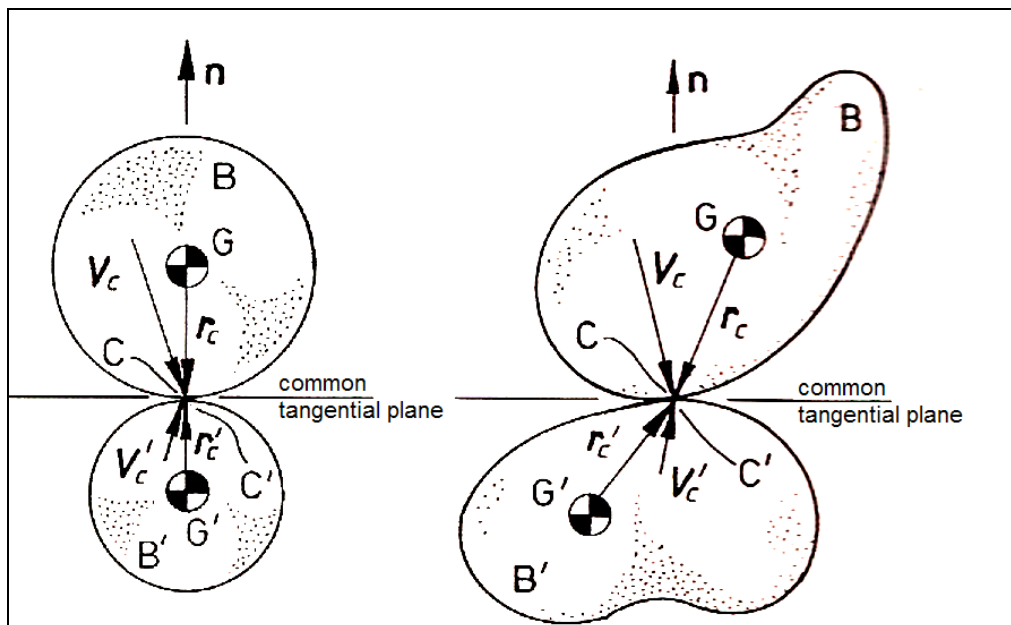


Figure 3: Scheme of Center Impact (left) Eccentric Impact (right)

The impulse caused by the impact of bodies results in a deformation at the contact area. Impact induced deformation is dependent on the impact velocity, contact area, contact duration and material hardness. Unquestionably, the relative velocity of the bodies is the most important parameter when characterizing an impact case. Hyper speed impacts; for instance, involves projection velocities of more than 10km/s [5]. Such high velocities can be achieved by gas guns or electromagnetic guns; however, experiments are limited after 9km/s since it is impractical to measure pressure waves with the current technology of devices. To give an example; hyper velocities address strain rates to be as much as 10^6 s^{-1} ; whereas, car accidents have a strain rate from 10^{-2} s^{-1} to 10^2 s^{-1} [6]. Figure 4 shows a simple diagram of the relation between sample event and impact velocity.

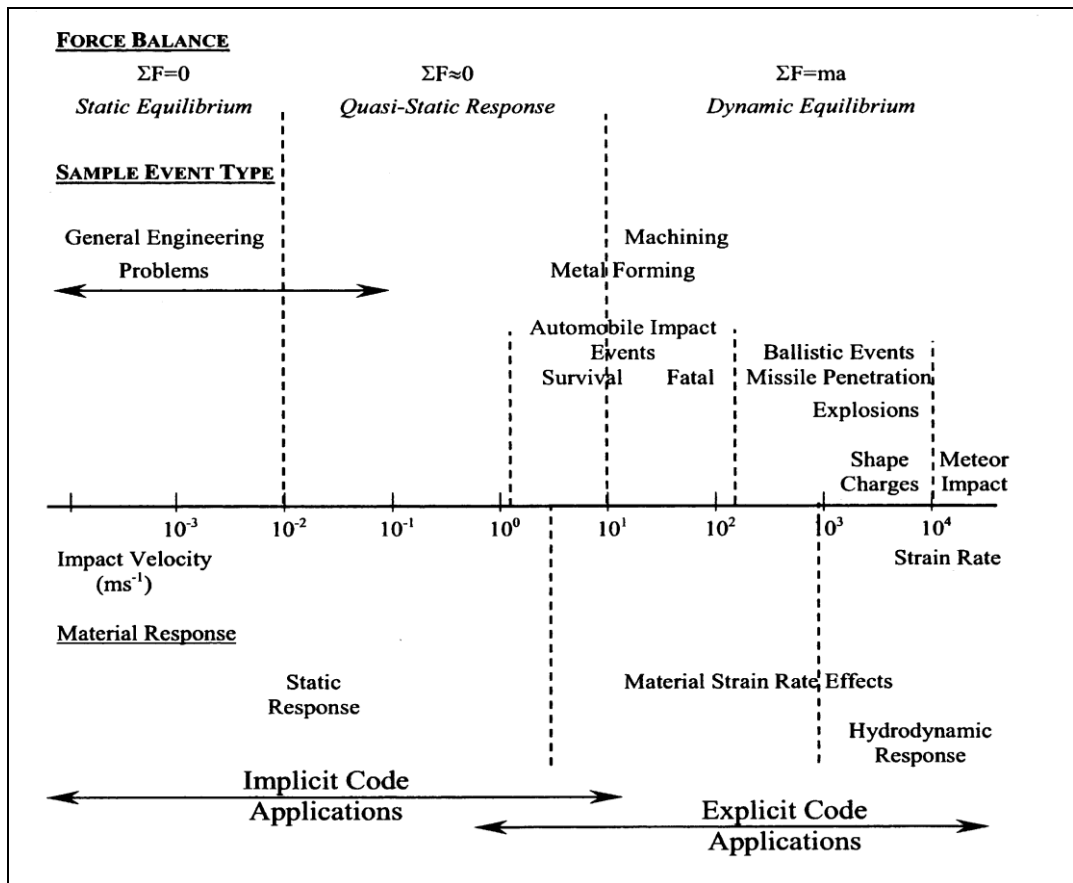


Figure 4: Impact velocities of sample events [9]

Due to the low strain rates, low velocity impacts are easier to examine. If the relative velocity of two bodies is less than 10 m/s then the impact phenomenon is considered to be low velocity impact. Although high velocity impacts result in high strain rates and high damage on the composite structure, the importance of low level impact should not be underestimated. Low level impacts may result in internal damage on the composite that may not be visible by naked eye [7]. Internal damage caused by low velocity impact can be examined in two categories: interlaminar damage which is called “delamination”; and intralaminar damage which is transverse ply cracking [8].

Belly landing cases of mini UAVs are in low velocity impact class; therefore, designers should spend enough time on analyzing landing loads and their possible effects. According to the operational use of the UAV necessary improvements should be made on the composite parts.

1.5. Composite Materials

Composite material refers to the material systems that are made from two or more materials with different material properties. Fiber reinforced composite materials are widely used in aerospace industry. In fiber reinforced composites fibers and the matrix material form the two main constituents of the composite material. Fiber gives the strength of the product whereas matrix builds up the integrity. The use of two main constituents causes the composite material to behave anisotropically.

There are many fiber material types used in composite materials. Carbon, E-glass and Kevlar are the most often used fabrics in aircraft structures. When these fabrics are cured with a resin system such as epoxy, the resulting structure becomes stiff and lightweight compared to metal counterparts. Different combinations (i.e. layups) of these fabrics result in different composites parts and they have different mechanical properties in terms of strength, stiffness, wear resistance, fatigue life, thermal insulation, thermal conductivity, weight, acoustical insulation and temperature dependent behavior [7]. Impact behavior of composites is under investigation of researchers since the beginning of 1980's [8]. After the year 2000, the research is accelerated. A number of experiments are conducted in order to understand the buckling, cracking, delamination, shear-out and fiber fracture characteristics of composite laminates [9]. Effect of laminate thickness and

resin/fibre volume fraction on impact is also studied widely [10], [11]. Experiments on glass-fiber-epoxy-matrix are almost completed [12].

The studies so far showed that by having a good design, use of composite materials can be very advantageous. Laminated patterns can be built up so that necessary stiffness in the required direction can be obtained. High stiffness-to-weight and high strength-to-weight results can be achieved.

A final important feature about the composites is their high corrosion resistance and excessive outdoor weathering ability.

.

1.6. Belly Landing UAV's

For mini UAVs, belly landing is a good solution for weight and cost reduction and simple operation. Firstly, the weight of the UAV can be decreased while maintaining the integrity since the landing gears and gear struts are omitted. Moreover, there is no need to stiffen the regions of fuselage where landing gear struts are attached. Secondly, landing gear carries impact loads and needs to be designed and manufactured accordingly. Omitting landing gear shortcuts the important design and manufacturing process; to put differently, it is cost effective to employ belly landing UAV's. Even high speed UAVs are using this feature. For a turbine powered UAV designed by University of Salt Lake City belly landing is decided since conventional configuration has a drag and weight penalty [16]. Finally, belly landing enables the UAV to take off and land from anywhere; in other words, a proper runway is not needed. A simple hand launch allows the UAV to climb to operating altitude and perform the mission. When the mission is completed, the UAV simply lands on the grass or gravel.

Due to the advantages mentioned above there are numerous belly landing UAVs in the market.

METU "Güventürk", AeroVironment RQ-11 Raven, AeroVironment FQM-151 Pointer, Boeing ScanEagle UAV, BAI's Javelin and AAI's Aerosonde are some examples of belly landing UAV platforms.

A photo of "Güventürk" during belly landing is given in Figure 2.

1.7. Objective of the Study

The scope of this study is to help the designer in making design decisions for a mini UAV that is tolerable to low velocity impact loads. To achieve this aim, “Güventürk” mini UAV that is designed and built by Middle East Technical University Aerospace Department is analyzed.

Low velocity impact phenomenon is examined in second chapter in detail. The theory of an approach introduced by Greszczuk [17] is examined in details. Greszczuk assumes that low velocity impact is “quasi-static” and proposes that the impulsive force on a target caused by an impactor can be replaced with a static force. The application area of the force can also be found. The impact problem can then be solved analytically. At the end of the second chapter, it is shown that for special class of orthotropic laminates, for which elastic properties are orientation independent, the approach of Greszczuk can be followed.

In the third chapter, the details of implicit and explicit methods are given. They are compared in terms of their applicability on finite element analysis problems. MSC.Software Programs are also introduced in Chapter 3. Then, the method introduced by Greszczuk is applied on fixed steel plates. The force on the steel plate caused by an impactor is found and applied on the steel plate as static load. Maximum deformations for different test cases are found. Then, test cases are remodeled in MSC.Patran and explicit dynamic finite element solution method is applied to find the deformations calculated previously. The results are compared and applicability of Hertzian Contact Law is discussed. At the end of the third chapter, the same comparison is made again for a composite plate.

Chapter 4 is dedicated to “Güventürk” Mini UAV. System description and specifications and brief information about the production of its composite parts is given. Belly landing condition of “Güventürk” is discussed in detail.

In Chapter 5, a complete analysis of “Güventürk” is given. Fuselage finite element model is introduced. Following a buildup approach, sequential analyses including fuselage shell, fuselage with internal structure and fuselage with wing are completed. Extra effort is given to the analyses concerning the different stacking sequences of fuselage composite laminates. Several test runs are executed for fuselage with internal structure case. The effect of changing stacking sequence on maximum stress is compared with simple plate analysis. Then, an alternative target

surface is examined. Soil is modeled as an elastic material and all analyses are repeated as the landing surface changes from rigid to soil.

Chapter 6 is the conclusion part; therefore, all the results are summarized and comments are given. A list of suggested future works is also developed.

CHAPTER 2

LOW VELOCITY IMPACT LOAD AND STRESS ANALYSIS

2.1. Low Velocity Impact

Impact phenomena can be categorized based on the impactor's relative velocity with respect to the target. Typically, an impact case with an approach velocity below 10m/s is considered as "Low Velocity Impact". In this section low velocity impact phenomena is introduced briefly and a simplified method of analysis of low velocity impact behavior of isotropic and composite plate like structures is demonstrated. It should be noted that the belly landing of a mini unmanned air vehicle on ground falls under the low velocity impact phenomena because the vertical descent speeds of such air vehicles are in general less than 10 m/s.

For low velocity impact cases with impact velocity below 10^{-2} m/s static equilibrium ($\sum F= 0$) can be assumed. If the impact velocity is between 10^{-2} m/s and 10m/s, then the force equilibrium is assumed to be quasi-static. ($\sum F \approx 0$)

Low velocity impact assumption can be made for a span of problems including general engineering problems, aircraft belly landing events or even slow car accidents.

2.2. Determining the Impact Load by Considering the Low Velocity Impact as "Quasi-Static"

When an impactor approaches and impacts a target, the impact causes a time dependent pressure field. As a result of the pressure, stress is observed in the target which may eventually cause failure. To find out the amount of stress, the pressure should be calculated first. For low velocity impact problems Greszczuk [17] proposed an analytical approach to design for impact response. Such an analytical treatment was proposed to address the issue of having a criterion for determining how the various properties of the target and the impact parameters influence target

damage. Especially for composite targets the availability of different composite material types and variety of design parameters, which can be adjusted to come up with different laminates, necessitates the use of simple analytical approach to design such composite structures subjected to impact loading. It should be noted that analytical approach does not have to provide close to exact impact response for all impact speeds. If the analytical approach allows one to make a qualitative comparison of impact responses of the various design alternatives, then it can be used in preliminary design stage to decide on the laminate configuration.

The approach in studying the response of isotropic and composite materials to low velocity impact consists of three major steps [17]. These steps are:

- Determination of impactor induced surface pressure and its distribution
- Determination of internal stresses in the target caused by surface pressure
- Determination of failure modes in the target caused by the internal stresses

In the simple analytical solution of the low velocity impact response of plate like structures, the magnitude and distribution of pressure distribution in the target can be obtained by combining the dynamic solution to the problem of impact of solids with the static solution for the pressure between two bodies in contact. Thus, in this method by applying the Hertz Contact Law [17] this dynamic problem can be converted into a static problem. Hertz Law states that the magnitude and the application area of the force caused by the impact can be estimated by an analytical approach. In order for the Hertz Law to be applicable, following assumptions have to be made:

- The impactor is linear elastic
- Contact duration of the target and impactor is relatively long compared to their natural periods; in other words, vibrations can be neglected.
- The impact is normal to the surface.

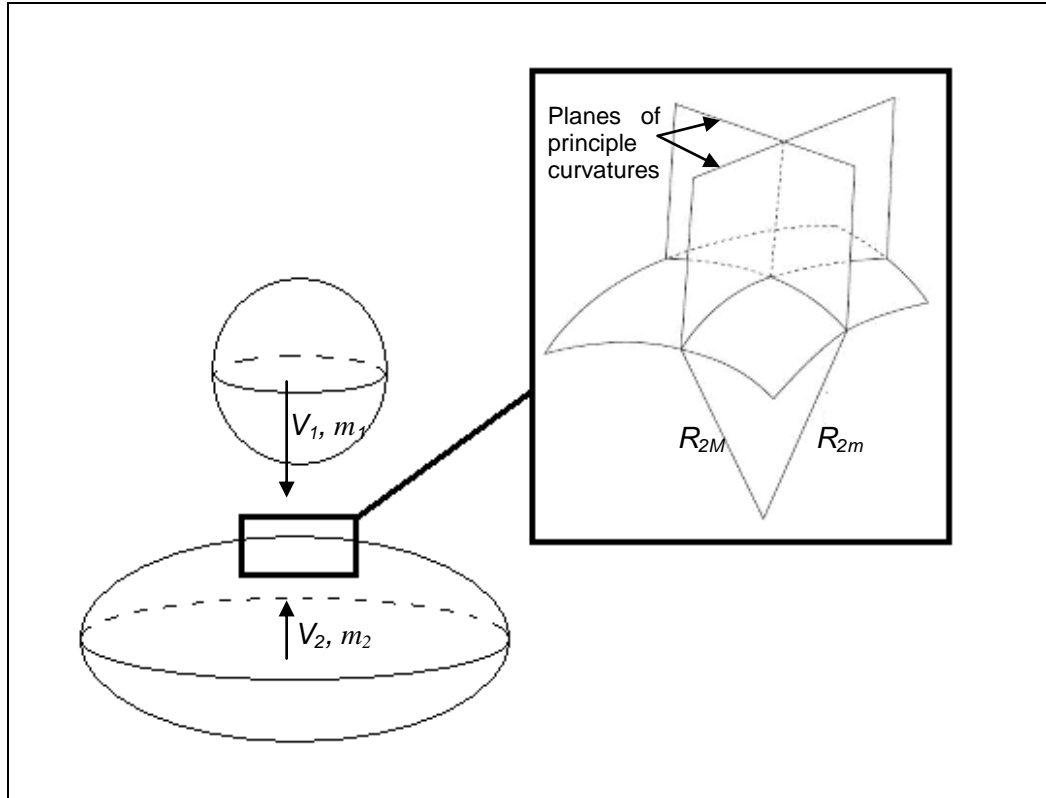


Figure 5: General Impact Case

In the simple approach, for a general impact event shown in Figure 5, it is assumed that Hertz Law that was established for static conditions applies also during impact. Therefore, it is possible to calculate the magnitude and distribution of the impact force. At the time of impact, the rates of changes in velocity of target and impactor are given by [17]:

$$m_1 \frac{dV_1}{dt} = -P, \quad m_2 \frac{dV_2}{dt} = P \quad (1)$$

where m_1 and V_1 are the mass and the velocity of the impactor, and m_2 and V_2 are the mass and the velocity of the target.

Approach velocity is the derivative of the distance, α , that the impactor and target approach one another:

$$\dot{\alpha} = V_1 + V_2 \quad (2)$$

Assume that the principle radii of curvature of impactor at the point of contact are R_{1m} and R_{1M} . And also assume that the principle radii of curvature of target at the same point are R_{2m} and R_{2M} . According to Hertz Law, the contact area is an ellipse with major and minor axes being [18]

$$a = m \left[\frac{3\pi}{2} P \left(k_1' + k_2' \right) C_R \right]^{1/3} \quad (3)$$

$$b = r \left[\frac{3\pi}{2} P \left(k_1' + k_2' \right) C_R \right]^{1/3} \quad (4)$$

where C_R is a term that takes into account the curvature effect and it is given by [17]:

$$\frac{1}{C_R} = \frac{1}{R_{1m}} + \frac{1}{R_{1M}} + \frac{1}{R_{2m}} + \frac{1}{R_{2M}} \quad (5)$$

For isotropic impactor and targets k_1' , k_2' are given by:

$$k_1' = \frac{1 - \nu_1^2}{\pi E_1}, \quad k_2' = \frac{1 - \nu_2^2}{\pi E_2} \quad (6)$$

For the general case of impact between two nonisotropic bodies of revolution k_1' and k_2' are yet to be defined. These are the parameters that take into account the elastic properties of the impactor and the target.

In addition, m and r are constants and they are related to a parameter θ defined in by Equation (8). m , r values are given in Table 2 after calculating θ from Equation (8) and C_R from Equation (7).

$$\frac{1}{C_R} = \frac{1}{R_{1m}} + \frac{1}{R_{1M}} + \frac{1}{R_{2m}} + \frac{1}{R_{2M}} \quad (7)$$

$$\theta = \arccos \left\{ C_R \left[\left(\frac{1}{R_{1m}} - \frac{1}{R_{1M}} \right)^2 + \left(\frac{1}{R_{2m}} - \frac{1}{R_{2M}} \right)^2 + 2 \left(\frac{1}{R_{1m}} - \frac{1}{R_{1M}} \right) \left(\frac{1}{R_{2m}} - \frac{1}{R_{2M}} \right) \cos 2\phi \right]^{\frac{1}{2}} \right\} \quad (8)$$

In Equation (8) ϕ is the angle between normal planes containing the curvatures R_{1m} and R_{2m} .

Table 2 Values of Parameters m , r , and s

θ	0°	10°	20°	30°	40°	50°	60°	70°	80°	90°
m	∞	6.612	3.778	2.731	2.136	1.754	1.486	1.284	1.128	1.00
r	0	0.319	0.408	0.493	0.567	0.641	0.717	0.802	0.893	1.00
s	-	0.851	1.220	1.453	1.637	1.772	1.875	1.994	1.985	2.00

The total deformation of both impactor and the target is given by [17]:

$$\alpha = s \left[\frac{9\pi^2 P^2 \left(\frac{1}{k_1} + \frac{1}{k_2} \right)}{256 C_R} \right]^{1/3} \quad (9)$$

If the above equation is solved for contact force one gets:

$$P = n' \alpha^{3/2} \quad (10)$$

where,

$$n' = \left(\frac{16}{3\pi \left(\frac{1}{k_1} + \frac{1}{k_2} \right)} \right) \sqrt{\frac{C_R}{s^3}} \quad (11)$$

In Equation (9) and Equation (11) parameter s is given in Table (2).

If Equation (2) is differentiated with respect to time, combined with Equation (1) and the result is substituted into Equation (10) following equation is found:

$$\ddot{\alpha} = n' M \alpha^{3/2} \quad (12)$$

where,

$$M = \frac{1}{m_1} + \frac{1}{m_2} \quad (13)$$

If both sides of Equation (12) is multiplied by $\dot{\alpha}$ and integrated, following result is obtained:

$$\dot{\alpha}^2 - V^2 = -\frac{4}{5} M n' \alpha^{5/2} \quad (14)$$

V is the initial relative velocity of the impactor at time zero. At the time of maximum deflection, α_{\max} , the rate of deflection, $\dot{\alpha}$, becomes zero; hence maximum deflection can be determined as:

$$\alpha_{\max} = \left(\frac{5V^2}{4Mn'} \right)^{2/5} \quad (15)$$

Substituting Equation (11) into Equation (15) and combining it with Equation (10) the impact force can be written as:

$$P = n' \left(\frac{5V^2}{4Mn'} \right)^{3/5} \quad (16)$$

Having found the impact force, the pressure distribution can now be determined. In case of contact problem involving solids of revolution, the force distribution has been shown to be of the form [17]:

$$q_{x,y} = q_0 \left[1 - \frac{x^2}{a^2} - \frac{y^2}{b^2} \right] \quad (17)$$

where q_0 , a and b can be found from the following relations:

$$q_0 = \frac{3P}{2\pi ab} \quad (18)$$

$$\frac{a}{m} = \frac{b}{r} = \left[\frac{3\pi}{2} \left(k_1' + k_2' \right) \left(\frac{5V^2}{4M} \right)^{3/5} \right]^{1/3} \quad (19)$$

k_1' and k_2' is given in Equation (6) and can be used if the impactor and the target are isotropic solids.

It should be noted once again that k_1' and k_2' given by Equation (6) can be used if the impactor and the target are isotropic solids. In addition, if the impactor is assumed to be rigid compared to the target k_1' can be neglected. For composite targets if the designed laminate is quasi-isotropic then an equivalent modulus of elasticity can be determined for the target material and k_2' given by Equation (6) can still be used. It has been reported by [17] that no closed form solution exists for k_2' for generally orthotropic solids. It is also reported that an approximate numerical solution for k_2' for generally orthotropic solids shows that k_2' is relatively insensitive to the fiber orientation. The parameter k_2' for a generally orthotropic material can also be determined experimentally. For instance for a spherical indenter ($R_{1m} = R_{1M} = R$) and flat target $R_{2m} = R_{2M} = \infty$, one can obtain a relation for k_2' in terms of contact load P , and total deformation α by performing a static indentation test. Thus, from the knowledge of contact load P and the deformation of the target, k_2' can be determined.

2.3. Quasi-static Low Velocity Impact Analysis of Composite Laminates

Low velocity impact damage on composite plates can be analyzed experimentally or by means of finite element programs. There are numerous computer codes which can solve this type of impact programs such as MARC, ANSYS or NASTRAN. In the literature, there are a number of studies covering impact analysis of composites considering different cases.

In this study, applicability of Hertz Method to analyze the behavior of composite plates will be investigated. Details of the method are given in the previous section of this chapter.

In this section simplified analytical method of analysis is performed by utilizing the Hertz Contact Law to determine the loading due low velocity impact. The method is applied to composite quasi-isotropic laminates so that Equation (6) can be used in the calculation of constants k_1' and k_2' . In chapter 3 results of the simplified method are also compared with the results of explicit finite element solution of the low velocity impact problem. This way one can form an opinion about the applicability of the simplified analytical approach and decide if such the outcome of such an approach can be used as a criterion for determining how the various properties of the target and the impact parameters influence the impact response.

There is a special class of orthotropic laminates for which the elastic properties are independent of orientation. In such laminates in-plane stiffnesses and compliances and all engineering constants are identical in all direction [19]. The main property of quasi-isotropic laminates is such that all shear coupling coefficients are zero. Thus, the laminate can be assumed to be quasi-isotropic if $A_{11}=A_{22}$ and $A_{16}=A_{26}=0$. In

general any laminate of $\left[0/\frac{\pi}{n}/\frac{2\pi}{n}/\dots/\frac{n-1}{n}\pi\right]_S$ or $\left[\frac{\pi}{n}/\frac{2\pi}{n}/\dots/\pi\right]_S$ lay-up is quasi-

isotropic for any integer value greater than or equal to 2.

The in-plane stress mid-plane strain relations are defined by the classical lamination theory.

$$\begin{Bmatrix} \sigma_1 \\ \sigma_2 \\ \tau_{12} \end{Bmatrix}_k = \begin{bmatrix} Q_{11} & Q_{12} & 0 \\ Q_{12} & Q_{22} & 0 \\ 0 & 0 & Q_{66} \end{bmatrix}_k \begin{Bmatrix} \varepsilon_1 \\ \varepsilon_2 \\ \gamma_{12} \end{Bmatrix} \quad (20)$$

Transformation to laminate axes yields:

$$\begin{Bmatrix} \sigma_x \\ \sigma_y \\ \tau_{xy} \end{Bmatrix}_k = \begin{bmatrix} \bar{Q}_{11} & \bar{Q}_{12} & \bar{Q}_{16} \\ \bar{Q}_{12} & \bar{Q}_{22} & \bar{Q}_{26} \\ \bar{Q}_{16} & \bar{Q}_{26} & \bar{Q}_{66} \end{bmatrix}_k \begin{Bmatrix} \varepsilon_x \\ \varepsilon_y \\ \gamma_{xy} \end{Bmatrix} \quad (21)$$

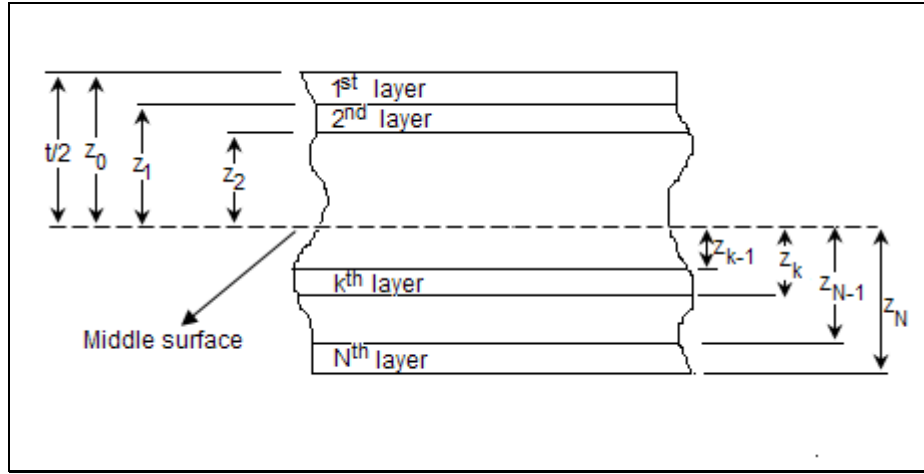


Figure 6: Cross section of an N-layered laminate

For the N-layered laminate given in Figure (6), the extensional stiffness is given by:

$$A_{ij} = \sum_{k=1}^N \bar{Q}_{ij} (z_k - z_{k-1}) \quad (22)$$

For quasi-isotropic laminates in-plane force resultant mid-plane strain relations are then:

$$\begin{Bmatrix} N_x \\ N_y \\ N_s \end{Bmatrix} = \begin{bmatrix} A_{xx} & A_{xy} & 0 \\ A_{xy} & A_{yy} & 0 \\ 0 & 0 & A_{ss} \end{bmatrix} \begin{Bmatrix} \varepsilon_x \\ \varepsilon_y \\ \gamma_{xy} \end{Bmatrix} \quad (23)$$

By making use of Eq. (23), in-plane moduli of the composite plate can be found by:

$$E_x = E_y = \frac{A_{xx} \cdot A_{yy} - A_{xy}^2}{t \cdot A_{xx}} \quad (24)$$

where, t is the thickness of the laminate. The effective Poisson's Ratio can also be determined as:

$$\nu = \frac{A_{xy}}{A_{xx}} = \frac{A_{xy}}{A_{yy}} \quad (25)$$

Thus, for quasi-isotropic laminates effective elastic Modulus and Poisson's Ratio can be used for the calculation of the constant k_2' in Equation (6) and the rest of the

steps described in the previous section can be followed in order to obtain the magnitude and the application area of the impact force due to low velocity impact.

CHAPTER 3

LOW VELOCITY IMPACT ANALYSIS WITH FINITE ELEMENT METHOD

3.1. Implicit Method

The majority of finite element programs use implicit methods to carry out a transient solution of structures subjected to time varying loads including impact loads. Normally, these programs use Newmark schemes to integrate in time [20]. If the current time step is step n , a good estimate of the acceleration at the end of step $n + 1$ will satisfy the following equation of motion:

$$Ma'_{n+1} + CV'_{n+1} + Kd'_{n+1} = F_{n+1}^{ext} \quad (26)$$

where

M = mass matrix of the structure

C = damping matrix of the structure

K = stiffness matrix of the structure

F_{n+1}^{ext} = vector of externally applied loads at step $n+1$

a'_{n+1} = estimated acceleration at step $n+1$

V'_{n+1} = estimated velocity at step $n+1$

d'_{n+1} = estimated displacement at step $n+1$

Implicit methods are solved in time by applying Newmark method. [20]

Considering the equation of motion:

$$u = \dot{u}t + \frac{1}{2}\ddot{u}t^2 \quad (27)$$

Newmark states that, the first time derivative in the equation of motion can be solved as:

$$\dot{u}_{n+1} = \dot{u}_n + \Delta t \ddot{u}_\gamma \quad (28)$$

where,

$$\ddot{u}_\gamma = (1-\gamma)\ddot{u}_n + \gamma\ddot{u}_{n+1} \quad 0 \leq \gamma \leq 1 \quad (29)$$

Thus, equation (28) can be rewritten as:

$$\dot{u}_{n+1} = \dot{u}_n + (1-\gamma)\ddot{u}_n \Delta t + \gamma\ddot{u}_{n+1} \Delta t \quad (30)$$

Newmark also applied mean value theorem to the displacement equation:

$$u_{n+1} = u_n + \dot{u}_n \Delta t + \frac{1}{2} \ddot{u}_\beta \Delta t^2 \quad (31)$$

where,

$$\ddot{u}_\beta = (1-2\beta)\ddot{u}_n + 2\beta\ddot{u}_{n+1} \quad 0 \leq \beta \leq 1 \quad (32)$$

Therefore, equation (31) becomes:

$$u_{n+1} = u_n + \dot{u}_n \Delta t + \frac{1-2\beta}{2} \ddot{u}_n \Delta t^2 + \beta \ddot{u}_{n+1} \Delta t^2 \quad (33)$$

Equation (33) and (30) can be rewritten as the estimates of displacement and velocity:

$$d'_{n+1} = d_n + V_n \Delta t + ((1-2\beta)a_n \Delta t^2) / 2 + \beta a'_{n+1} \Delta t^2 \quad (34)$$

$$V'_{n+1} = V_n + (1-\gamma)a_n \Delta t + \gamma a'_{n+1} \Delta t \quad (35)$$

(33) and (34) can be rewritten as:

$$d'_{n+1} = d_n^* + \beta a'_{n+1} \Delta t^2 \quad (36)$$

$$V'_{n+1} = V_n^* + \gamma a'_{n+1} \Delta t \quad (37)$$

where, d_n^* and V_n^* are known or predictive values, β and γ are constants, Δt is time step.

Substituting (36) and (37) into (26)

$$M a'_{n+1} + C \left(V_n^* + \gamma a'_{n+1} \Delta t \right) + K \left(d_n^* + \beta a'_{n+1} \Delta t^2 \right) = F_{n+1}^{ext} \quad (38)$$

$$\left(M + C\gamma\Delta t + K\beta\Delta t^2 \right) a'_{n+1} = F_{n+1}^{ext} - CV_n^* - Kd_n^* \quad (39)$$

$$M^* a_{n+1} = F_{n+1}^{residual} \quad (40)$$

By inverting the matrix M^* accelerations can be found.

Implicit solutions are unconditionally stable; therefore, time step size is chosen according to the required accuracy.

3.2. Explicit Method

Matrix solutions are not required for explicit methods. The equation of motion is used to obtain acceleration.

$$Ma_n + CV_n + Kd_n = F_n^{ext} \quad (41)$$

$$Ma_n = F_n^{ext} - CV_n - Kd_n \quad (42)$$

If internal forces are defined as:

$$F_n^{int} = CV_n + Kd_n \quad (43)$$

Equation (41) becomes:

$$Ma_n = F_n^{ext} - F_n^{int} \quad (44)$$

$$a_n = M^{-1} (F_n^{ext} - F_n^{int}) \quad (45)$$

M matrix is diagonal and inversion of M is trivial. Therefore, Equation (45) is set of independent equations. Assuming acceleration is constant through the time step, velocities and displacements are found by central difference method.

$$V_{n+1/2} = V_{n-1/2} + \frac{a_n}{2} (\Delta t_{n+1/2} + \Delta t_{n-1/2}) \quad (46)$$

$$d_{n+1} = d_n + V_{n+1/2} \Delta t_{n+1/2} \quad (47)$$

The loop given in Figure 7 is carried out for each time step.

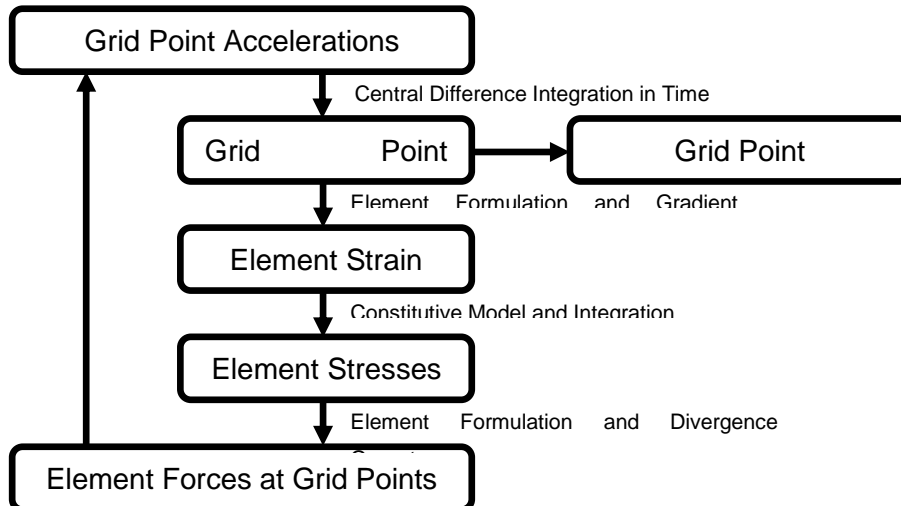


Figure 7: Explicit Method Scheme [20]

Explicit methods can be made unconditionally stable if the time step is chosen to be less than the time taken for a stress wave to cross the smallest element in the mesh. Typically, explicit time steps are 100 to 1000 times smaller than those used with implicit codes.

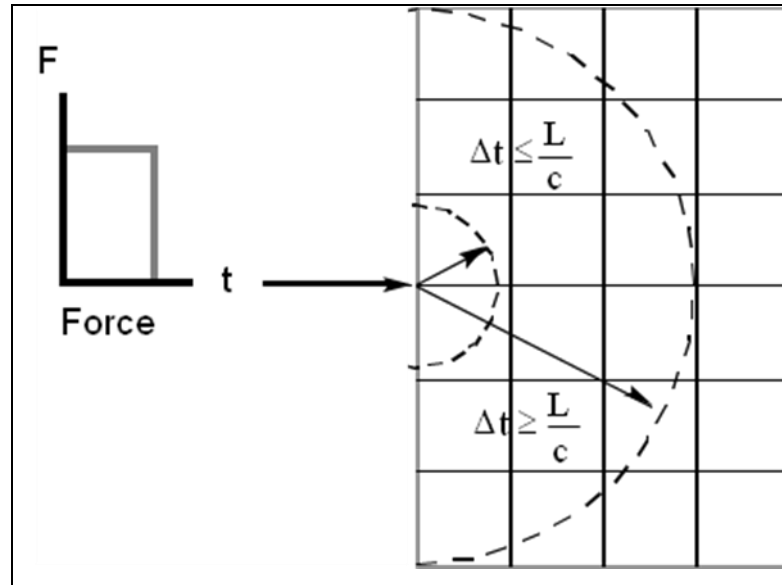


Figure 8: Time Step and Stress Waves Relationship

Figure 8 shows the propagation of stress waves in a media.

where,

L = Minimum element length

c = Speed of sound

Δt = time step

The stability limit of explicit method is the duration that the stress wave crosses the smallest element. It can be found by the following relation:

$$\Delta t_{critical} = \frac{2}{w_{max}} \left(\sqrt{1 + \xi^2} - \xi \right) \quad (48)$$

where,

w_{max} = The highest eigenvalue in the system

ξ = Fraction of critical damping in the highest mode

3.3. Comparison of Implicit and Explicit Methods

Differences between implicit and explicit methods are tabulated in Table (3).

Table 3: Comparison of Implicit and Explicit Methods

Implicit Methods	Explicit Methods
Bigger time step	Small time step
Big matrices and matrix inversion required	No big matrices and matrix inversion by having a diagonal matrix
Solution procedure complicated with increasing degree of nonlinearities	Robust solution procedure even for high degree of nonlinearities

The computational time is relatively long for explicit methods due to the small time step. On the contrary, matrix operations are simpler and reduce the calculation steps. If the problem includes nonlinearities such as large displacements, plasticity of material, large strain values or pressure spikes, the explicit method is still reliable. Computational cost of a problem linearly increases with the problem size for the explicit method; whereas, it increases exponentially for the implicit method. Duration of the problem is important as well. As the duration increases, implicit method becomes more applicable. Cost of implicit and explicit methods for various cases is given in Figure 9.

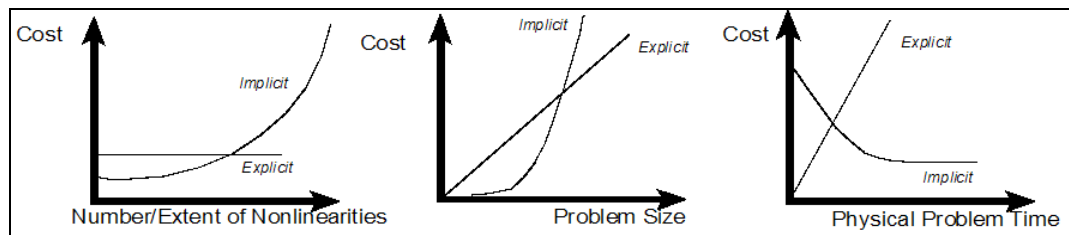


Figure 9: Cost of Methods for Various Cases [8]

For impact problems with an impact velocity greater than 1 m/s, it is essential that explicit method is applied.

The impact velocity of a belly landing UAV is most generally between 10^{-1} m/s and 10^0 m/s. This velocity regime can be called as “low velocity impact”. For low velocity impacts, strain rate is small; therefore, quasi-static approach can be followed.

3.4. MSC.Patran/Nastran

MSC.Patran is a software system, used primarily in mechanical engineering analysis [21]. It is comprised of engineering modeling functionalities, geometry access from external programs, analysis modules like thermal and fatigue, result visualization and reporting.

MSC.Nastran is a general purpose finite element analysis solution for small to complex assemblies [22]. Nastran provides a wide range of modeling and analysis capabilities, including linear statics, displacement, strain, stress, vibration and heat transfer.

In this study skin model of “Güventürk” Mini UAV has been completed in Dassault System’s CATIA v5.r13 [23] and imported into MSC.Patran. Patran is used for meshing outer skin and modeling the internal structure. Later, the whole model is laminated by Laminate Modeler Tool of MSC.

The process of importing a model into MSC.Patran is given in Appendix A.

The details of the Laminate Modeler Tool are explained in Appendix B.

3.5. MSC.Dytran

Dytran is an explicit finite element analysis (FEA) software for analyzing complex nonlinear behavior involving permanent deformation of material properties or the interaction of fluids and structures [24].

Generally, problem in space is solved by FEM and problem in time is solved by explicit time integration with small time increments. MSC.Dytran applies Lagrange Finite Element Technology and/or Euler Finite Volume Technology. Problem in time is solved by central difference integration.

Grid points are fixed to the body locations when Lagrange solver is applied. As the body moves or deforms grid points relocates with the body; in other words, in Lagrangian meshes elements are of constant mass. In another word, in Lagrangian meshes since the material points remain coincident with mesh points, elements deform with the material. Therefore, elements in a Lagrangian mesh can be severely distorted. A typical Lagrangian mesh is illustrated in Figure 10 which shows the undeformed and deformed configurations.

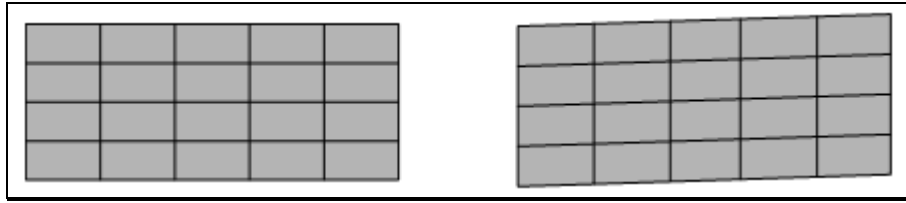


Figure 10: Lagrange Finite Element Technology – Elements of Constant Mass

On the other hand in Eulerian meshes, grid points are fixed to space.. Eulerian mesh acts as a fixed frame of reference; moreover, energy, mass and momentum transfers through elements. Figure 11 shows a typical Eulerian mesh at two different times. It is seen that the mesh does not change as the material passes through it.

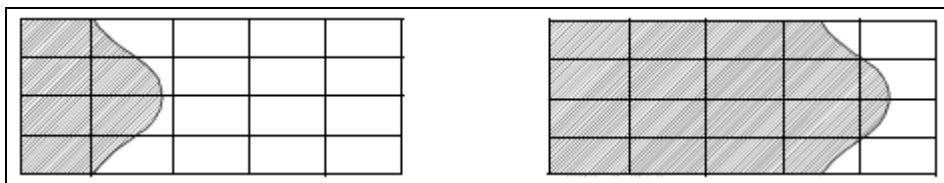


Figure 11: Euler Finite Volume Technology – Elements of Constant Volume

As it is mentioned in Section 3.2, in order to have a stable solution the time step size must be less than the duration of a stress wave to travel through the smallest element. For a problem with many elements, it is a long process to accomplish the eigenvalue analysis shown in Equation (48). An approximate method called Courant Criterion is applied in MSC.Dytran solver. Courant Criterion states that, [9]

$$\Delta t_{critical} = \frac{L}{c} \quad (49)$$

where,

L is the smallest element dimension, and the speed of sound can be approximated as:

$$c = \sqrt{\frac{E}{\rho}} \quad \text{for 1-D elements} \quad (50)$$

$$c = \sqrt{\frac{E}{\rho(1-\nu^2)}} \quad \text{for 2-D elements} \quad (51)$$

where,

E = Young's Modulus

ν = Poisson's Ratio

ρ = Density

Critical time step size is calculated for the whole model; that is for all of the elements, by using Courant Criteria. After calculating the critical time step values for all elements, the smallest one is multiplied by a safety factor, S .

$$\Delta t = S \cdot \Delta t_{critical} \quad (52)$$

The default safety factor is 0.666 for MSC.Dytran. However it can be reset to 0.9 for the models with Lagrangian elements only [9].

3.6. Examples of Low/High Velocity Impact Problem Solutions

In this section low velocity impact demonstrations are performed. The solutions are performed by modeling the impact phenomenon as a quasi-static event as described before and by performing explicit finite element solution using MSC Dytran. The impactor is assumed to be rigid to concentrate on what is happening in the target material. As for the target material for the initial solutions an isotropic material steel is used. Later on a quasi-isotropic laminate is modeled and low velocity impact solutions are performed.

In the initial analyses a rigid ball impactor of 0.1 m radius (r_{ball}) is projected to a steel square plate target of 1 m edge length (a_{plate}), as shown in Figure 12.

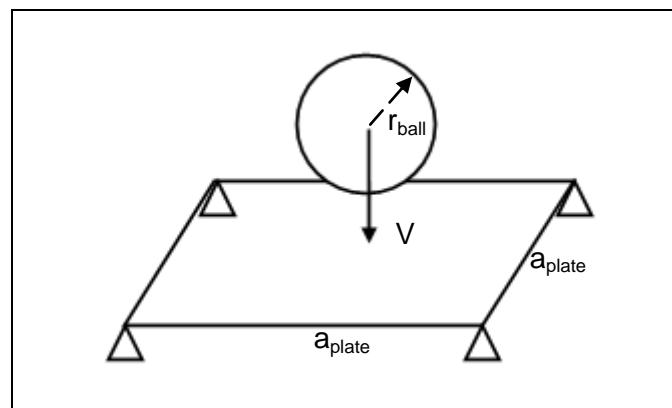


Figure 12: Impactor and Target

Properties of ball which is the impactor:

$$r_{ball} = 0.1m$$

$$E_{ball} = \infty \quad (\text{Rigid ball assumption})$$

$$V_{impact} = \text{Varying}$$

$$m_{ball} = \text{Varying}$$

Properties of steel plate which is the target:

$$a_{plate} = 1m$$

$$\nu = 0.3$$

$$\rho = 7850 \text{ kg/m}^3$$

$$t = 0.005m$$

$$E_{steel} = 2 \times 10^{11} Pa$$

Two different methods are used to solve this problem. In the first method, the impact case is assumed to be quasi-static. Hertz Law, as explained in detail in the chapter 2, is applied and the impact force is calculated. Then, the impact force is then applied as a static load to the plate and the problem is solved by MSC.Nastran utilizing linear static solver. In this method since the low velocity impact is modeled as a quasi-static event, it is expected that a static finite element solution might provide reasonable results especially for low impact velocities.

Secondly, the same impact problem is modeled in MSC.Patran and the explicit finite element analysis is performed by MSC.Dytran.

Finally, for different impact velocities of the ball, the solutions are compared and applicability of Hertz Law is investigated.

3.6.1. Solutions with MSC.Nastran by assuming low velocity impacts; “quasi-static” case

For a flexible, plate-like target, the surface pressure, area of contact and impact duration will be functions of the parameters entering in Equation (15), and Equation (18-19) as well as the bending stiffness of the plate and boundary conditions. For a given impact velocity the impact load P will decrease as the flexibility of the target increases [17]. Increase in target flexibility will also increase contact duration and decrease the contact area. An approximate solution for the impact response of a flexible target can be obtained by considering the deformations shown in Figure 12.

The case shown in Figure 13 indicates the local and overall deformation of flexible target at the moment of maximum deflection.

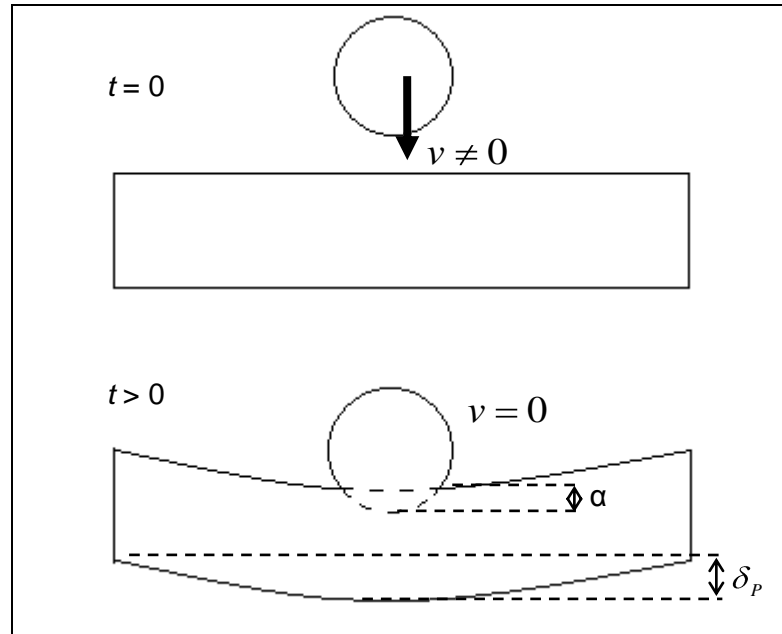


Figure 13: Local and Overall Deformation of the Target

In Figure 13 δ_p represent the maximum deflection of the plate and α indicates the Hertzian contact deformation.

According to Hertz Law, resulting impact force due to low velocity impact was given in Chapter 2 as:

$$P = n' \cdot \alpha^{3/2} \quad (10)$$

where,

α = the distance that impactor and target get closer to each other due to compression

For rigid impactor ball and plate case $R_{1m} = R_{1M} = r_{ball}$ and $R_{2m} = R_{2M} = \infty$.

Therefore, Equation (7) becomes:

$$\frac{1}{C_R} = \frac{2}{r_{ball}} \quad (53)$$

On the other hand, Equation (8) yields

$$\theta = \arccos(0) = \pi/2$$

For the θ value of $\pi/2$ Table 2 gives

$$m = 1$$

$$r = 1$$

$$s = 2$$

Therefore, Equation (11) becomes:

$$n' = n = \frac{4\sqrt{R_1}}{3\pi \left(\frac{1}{E_1} + \frac{1}{E_2} \right)} \quad (54)$$

where;

$$k_1 = \frac{1 - \nu_1^2}{\pi E_1} = 0 \quad (\text{Rigid ball assumption})$$

$$k_2 = \frac{1 - \nu_2^2}{\pi E_2}$$

If energy balance equation is written for the impact event shown in Figure 12 one gets:

$$\frac{1}{2} m_{ball} V_{ball}^2 = \int_0^{\delta_{max}} P_{plate} d\delta_{plate} + \int_0^{\alpha} P_{contact} d\alpha \quad (55)$$

where,

$$P_{contact} = P$$

$$P_{plate} = K_p \cdot \delta$$

and K_p is the spring constant for the plate.

Substituting Equation (10) and $P_{plate} = K_p \cdot \delta_p$ into Eq.(55) and noting that

$P_{contact} = P_{plate}$ Equation (55) can be rewritten as:

$$\frac{1}{2} m_{ball} V_{ball}^2 = \frac{1}{2} \left(\frac{P^2}{K_p} \right) + \frac{2}{5} \left(\frac{P^{5/3}}{n^{2/3}} \right) \quad (56)$$

In the ball impact problem over a plate Equation (3) and (4) becomes identical which means that impact area becomes circular:

$$a = b = \left[\frac{3\pi}{4} P \left(\frac{1}{E_1} + \frac{1}{E_2} \right) \right]^{1/3} \quad (57)$$

In Equation (56) if the spring constant of the plate K_p is known then the impact load P can be solved iteratively. The plate spring constant K_p can be determined easily by performing a linear static analysis by MSC.Nastran. In the current example the plate model is analyzed under 100 N concentrated load at the center of the plate,

and the maximum deflection is found as $2.53 \cdot 10^{-4} m$. Figure 14 shows the displacement plot of this solution.

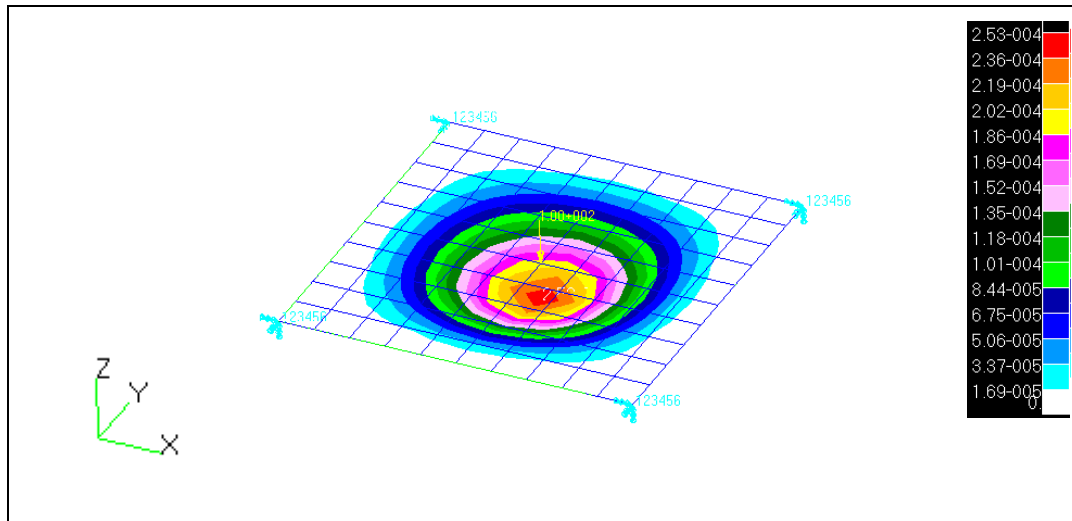


Figure 14: Calculation of Maximum Deflection of the Plate under 100N Load

Therefore; bending stiffness constant K_p for this particular plate is:

$$K_p = \frac{P}{\delta} = \frac{100}{2.53E-04} N/m \quad (58)$$

After all the unknown variables, except the impact load P , in Equation (56) have been calculated, P can be found by iteration. Force application area can also be calculated from Equation (57).

Tables 4-6 give the impact loads which are determined from the solution of Equation (56) for three different impactor masses and for five different impact velocities.

Table 4: Iteration of P for m=0.2kg

m_{ball} (kg)	0.2				
V_{ball} (m/s)	0.1	0.5	1	5	10
P (N)	28.045	140.372	280.83	1404.836	2810.071
Area (m^2)	2,12E-4	3,63E-4	4,58E-4	7,82E-4	9,86E-4

Table 5: Iteration of P for m=2kg

m_{ball} (kg)	2				
V_{ball} (m/s)	0.1	0.5	1	5	10
P (N)	88.757	444.105	888,395	4443.456	8887.772
Area (m^2)	3,12E-4	5,33E-4	6,72E-4	1,149E-4	1,448E-4

Table 6: Iteration of P for m=20kg

m_{ball} (kg)	20				
V_{ball} (m/s)	0.1	0.5	1	5	10
P (N)	280,83	1404,835	2810,071	14053,543	28108,941
Area (m ²)	4,58E-4	7,83E-4	9,86E-4	16,86E-4	21,25E-4

The impact loads given in Table (4) and (6) are applied as concentrated forces in the geometric center of the steel plate, and each case is analyzed in MSC.Nastran and corresponding deflections are found. It should be noted that the right hand side of Equation (56) is proportional to almost square of the impact load. Therefore, if the impactor mass is increased by a factor then the impact load should increase by square root of that factor. The results given in Tables (4-6) confirm this behavior. For instance when the impactor mass is increased 100 times, from 0.2 kg to 20 kg, the impact load increases by approximately 10 times. In a similar fashion in Equation (56) impact velocity and impact load are approximately directly proportional to each other. This relation is also reflected in Tables (4-6). When the impact velocity is increased by a factor, the impact load also increases by the same factor. One last comment about the results given in Tables (4-6) is that the 20 kg impactor mass case combined with the impact velocities might put the problem out of the limits of linear analysis.

The impact loads given in Table (5) are first applied as concentrated forces and later on they are uniformly distributed on the steel plate over the circular impact area determined by Equation (57). This analysis is accomplished for three different velocity cases (0.1 m/s, 1 m/s, 10 m/s). Sample screenshots of MSC.Patran, for these analyses, are given in Figures 15 and 16. Figure 15 gives the displacement plot for the concentrated load case and Figure 16 gives the displacement plot for the distributed load case.

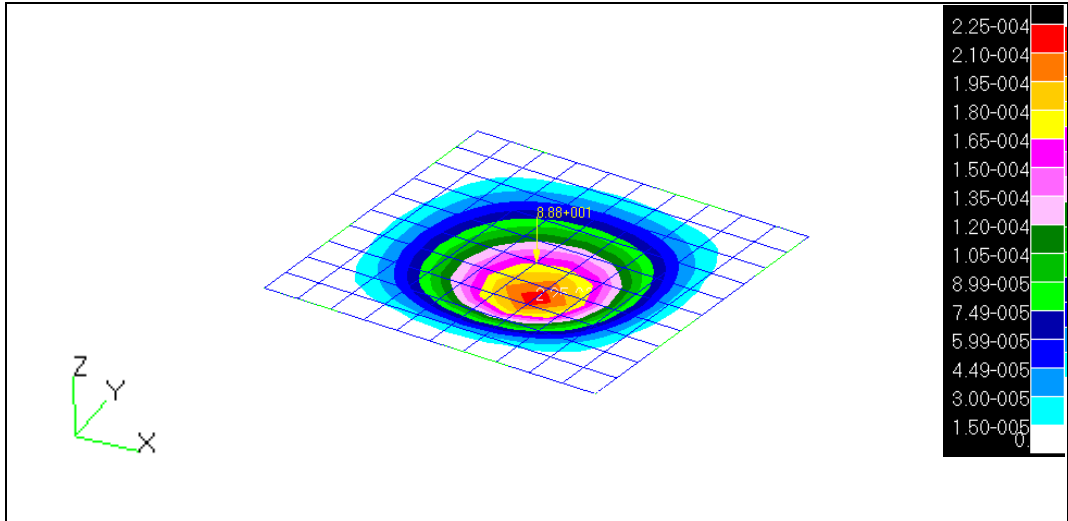


Figure 15: Maximum Deflection for Concentrated Load, $P=88.8\text{N}$, $m=2\text{kg}$, $V=0.1\text{m/s}$

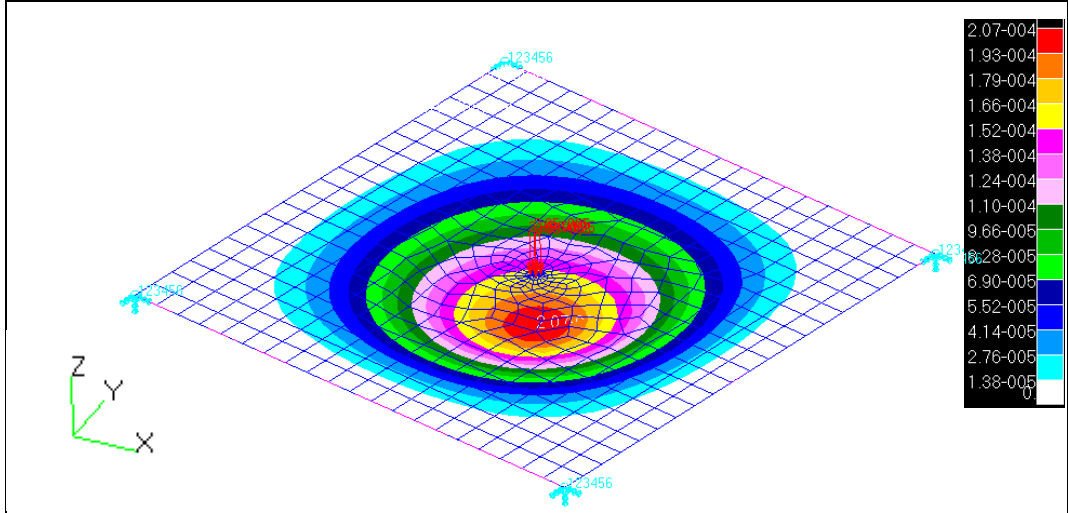


Figure 16: Maximum Deflection for Distributed Load, $P=88.8\text{N}$, $m=2\text{kg}$, $V=0.1\text{m/s}$

Meshing details of the distributed load case is given in Figure 17-18.

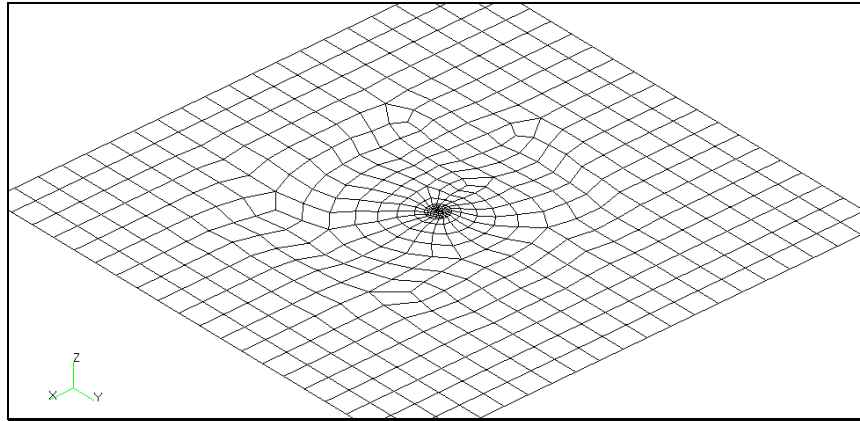


Figure 17: Meshing of Distributed Load Case

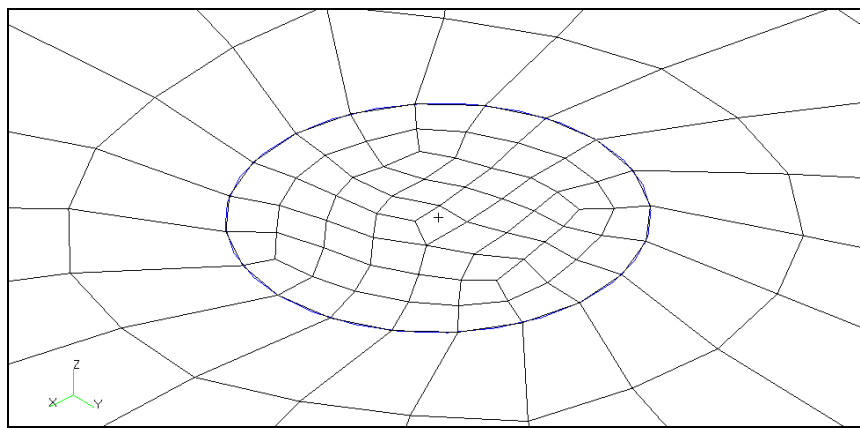


Figure 18: Meshing of Distributed Load Case (detail)

As it is explained in Chapter 2.3 the same low velocity impact problem is solved by using a classical orthotropic laminate as the target material instead of a steel plate. A composite laminate having four layer with a stacking sequence of $[0^\circ, 90^\circ, 90^\circ, 0^\circ]$ is taken and as the layer material carbon/epoxy is chosen. After modeling the carbon/epoxy laminate in MSC.Patran, the stiffness coefficient matrices A, B, D matrices are determined as:

$$\bar{\mathbf{A}} = \begin{bmatrix} 2.937823\text{E}+007 & 9.059633\text{E}+005 & 4.756234\text{E}-003 \\ 9.059633\text{E}+005 & 2.937823\text{E}+007 & -1.14748\text{E}+000 \\ 4.756234\text{E}-003 & -1.14748\text{E}+000 & 1.056000\text{E}+006 \end{bmatrix} Pa \quad (59)$$

$$\bar{\mathbf{B}} = \begin{bmatrix} 0.000000\text{E}+000 & -3.81469\text{E}-006 & 0.000000\text{E}+000 \\ -3.81469\text{E}-006 & -1.52587\text{E}-005 & 0.000000\text{E}+000 \\ 0.000000\text{E}+000 & 0.000000\text{E}+000 & 0.000000\text{E}+000 \end{bmatrix} Pa \quad (60)$$

$$\bar{\mathbf{D}} = \begin{bmatrix} 9.405161\text{E}-001 & 1.739449\text{E}-002 & 0.000000\text{E}+000 \\ 1.739449\text{E}-002 & 1.876079\text{E}-001 & 0.000000\text{E}+000 \\ 0.000000\text{E}+000 & 0.000000\text{E}+000 & 2.027520\text{E}-002 \end{bmatrix} Pa \quad (61)$$

As it was requested in Chapter 2.3, the in-plane extensional stiffness coefficients are equal to each other and the in-plane coupling stiffness coefficients are negligibly small. As a matter of fact from a theoretical point of view, the coupling coefficients should turn out to be exactly zero for the particular laminate.

$$A_{11} = A_{22}$$

$$A_{16} \approx A_{26} \approx 0$$

Therefore; the laminate can be regarded as quasi-isotropic and after determining the effective modulus and Poisson's ratio for the quasi-isotropic laminate, Hertz Law can be applied.

From Equation (24) and (25), the effective modulus and Poisson's ratio of the laminate are determined as

$$E_1 = E_2 = 6.12\text{E}+10 \text{ Pa}$$

$$\nu = 3.08\text{E}-02$$

Thickness of Carbon/Epoxy laminate used in the analysis is given by Turgut [25]:

$$t = 0.00053 \text{ m}$$

K_p is found again by modeling the plate in MSC.Patran and applying a concentrated force, similar to the isotropic target case.

$$K_p = \frac{10N}{0.139m} = 71.94N/m$$

Following the same procedure a set of results is obtained for the impact load for different impactor mass and impact velocities. For instance Figure 19 shows the displacement plot of the composite plate for an impact load of 0.38 N which is calculated for an impactor mass of 0.2 kg and impact velocity of 0.1 m/s.

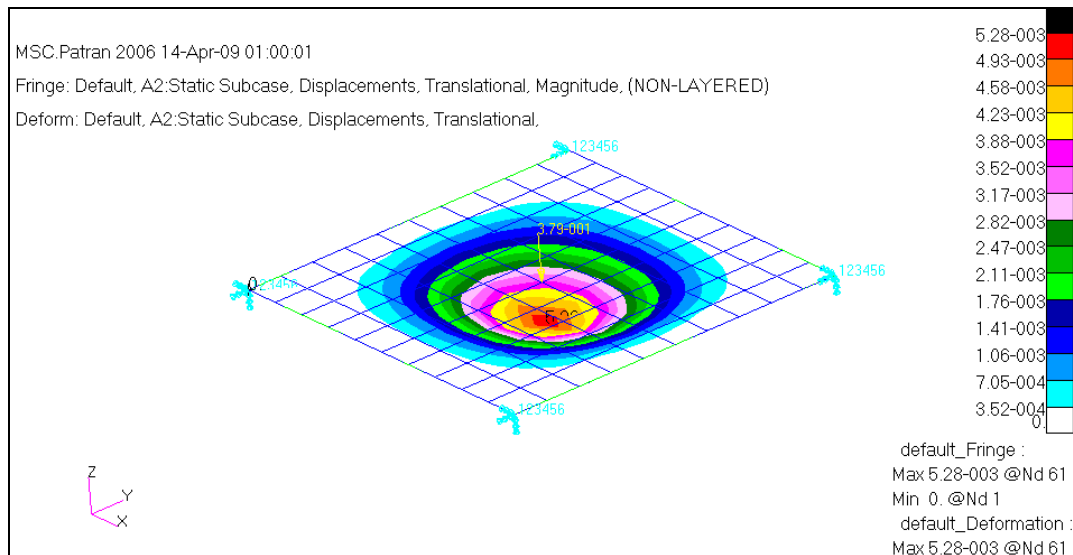


Figure 19: Maximum Deflection for Concentrated Load, $P=0.38\text{N}$, $m=0.2\text{kg}$, $V=0.1\text{m/s}$

3.6.2. Explicit finite element solutions of low velocity impact problems with MSC.Dytran

Low velocity impact problems, which were analyzed by a quasi-static approach in the previous sections, are solved by MSC.Dytran utilizing explicit finite element solution. In order to solve the same problems by MSC.Dytran, the model is built again in MSC.Patran. Boundary conditions of the plate, initial velocity of the ball and material properties of both of them are given as input. In the analyses performed by MSC.Dytran, there is no need to enter the contact area or duration of the impact because MSC.Dytran calculates the necessary parameters automatically.

After the completion of modeling, each case solved in Part 3.6.1 is resolved with MSC.Dytran.

A sample screenshot from MSC.Dytran analysis is given in Figure 20.

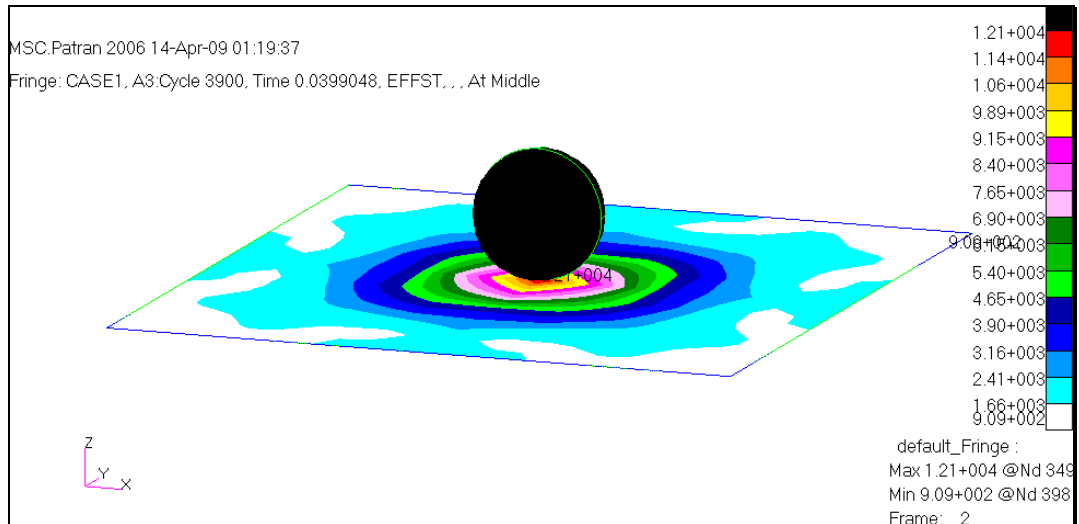


Figure 20: Sample screenshot from MSC.Dytran analysis

3.6.3. Comparison of quasi-static and explicit finite element solutions

The maximum plate deflections determined by the quasi-static analyses and explicit finite element solutions are compared in Table 7 for the steel plate.

Table 7: Maximum Deflection of Steel Plate for $m_{ball} = 2\text{kg}$

m_{ball} (kg)	2		
V_{ball} (m/s)	0.1	1	10
Dytran Solution (m)	-0.00011	-0.00109	-0.00777
Nastran Solution (m)	-0.00023	-0.00225	-0.0225
Nastran Solution (m) (force is uniformly distributed over the area given in Table 5)	-0.00021	-0.00216	-0.0216

Table 7 shows that application of the impact load in a concentrated fashion or as a uniformly distributed load over the area of contact gives very close deflection results, as expected. Tables 8 and 9 compare the maximum plate deflection for five different impact speeds for impactor masses of 0.2 kg and 20 kg, respectively. It is observed that explicit finite element solution consistently produces lower deflections compared to the quasi-static solutions obtained by MSC.Nastran.

Table 8: Maximum Deflection of Steel Plate for $m_{ball} = 0.2\text{kg}$

m_{ball} (kg)	0.2				
V_{ball} (m/s)	0.1	0.5	1	5	10
Dytran Solution (m)	-0.00002	-0.00009	-0.00019	-0.00094	-0.00186
Nastran Solution (m)	-0.00007	-0.00036	-0.00071	-0.00356	-0.00711

Table 9: Maximum Deflection of Steel Plate for $m_{ball} = 20\text{kg}$

m_{ball} (kg)	20				
V_{ball} (m/s)	0.1	0.5	1	5	10
Dytran Solution (m)	-0.00051	-0.00248	-0.00467	-0.01483	-0.02442
Nastran Solution (m)	-0.00071	-0.00356	-0.00711	-0.0356	-0.0711

Figures (21-23) below are sketched by using the data given in Tables 7-9. As it can be seen, the discrepancy between the result of quasi-static solution based on the Hertz method and the explicit finite element solution increases as the impact velocity increases. A graph drawn with more data points is given in Appendix E.

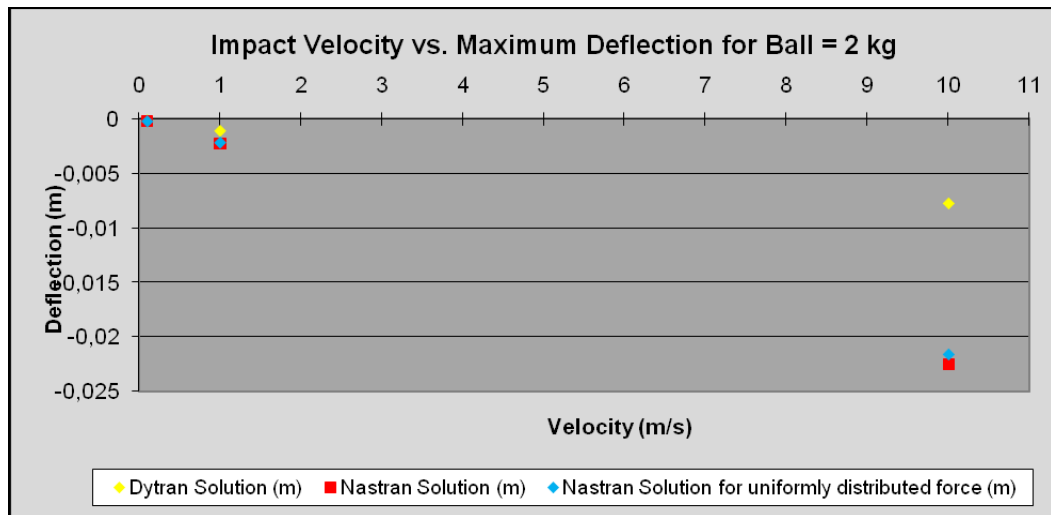


Figure 21: Comparison of Different Solution Methods for $m_{ball} = 2\text{kg}$

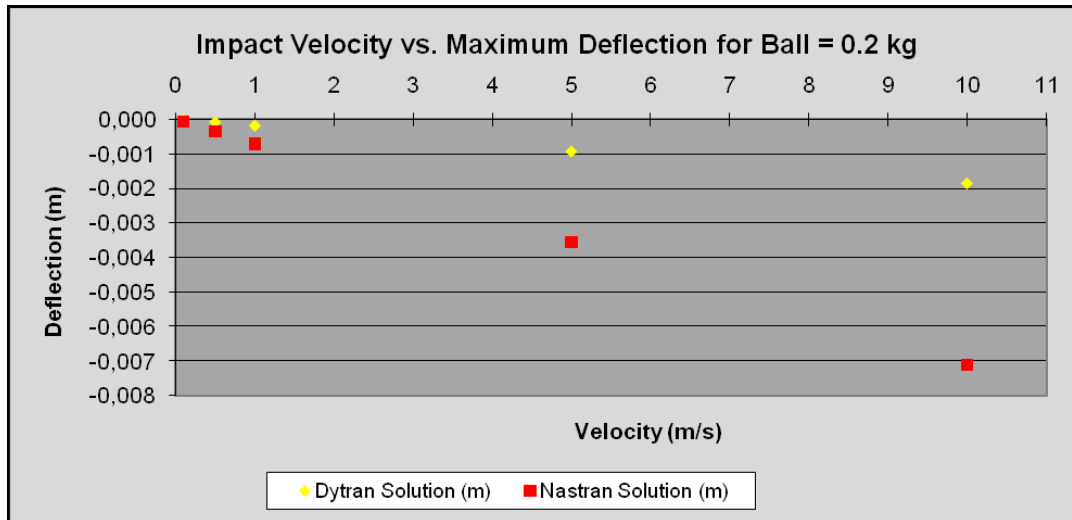


Figure 22: Comparison of Different Solution Methods for $m_{ball} = 0.2\text{kg}$

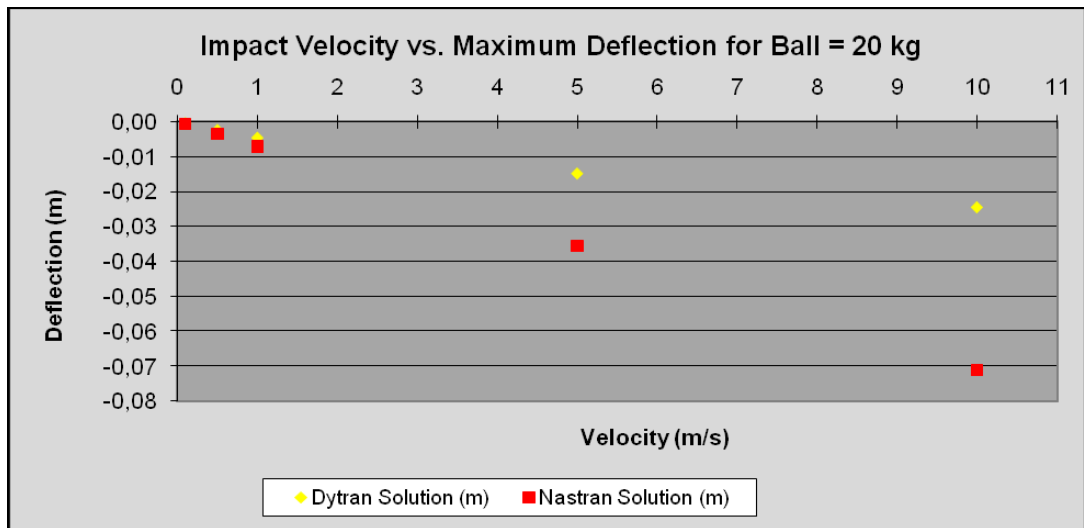


Figure 23: Comparison of Different Solution Methods for $m_{ball} = 20\text{kg}$

From the displacement results one conclusion that may be drawn is that the quasi-static approach overestimates the resulting deformation of the target material. The main reason for this could be due to the fact that in the quasi-static approach the peak impact load is assumed to act at full magnitude. However, in real case there is duration and the impact load increases from a zero value to peak value in a finite time. The total impact duration could also be calculated from Equation (14). Greszczuk [17] has calculated the total impact duration in his work from Equation (14), and it is seen that the total impact duration is inversely proportional with the impactor mass, as expected. Therefore, the impact duration is shorter if the mass of the impactor is higher. In addition, in the work of Greszczuk [17] the variation of the

impact load with time is seen to a half sine wave which is in accordance with the variation of impact deformation with time. It can be observed from Tables 7-9 that when the mass of the impactor is increased the percent difference between the quasi-static solution and explicit finite element solution decreases. This behavior is attributed to the fact that when the mass of the impactor is increased the impact duration decreases and the peak impact load is reached in a shorter time. Thus, the deformation induced by the peak impact load approaches to the quasi-static case in which the peak impact load is acting continuously. The discrepancy between the quasi-static solution and explicit finite element solution might also be due to the overestimation of the impact load in the quasi-static approach.

It should be noted that one could determine the variation of the impact load with time as described by Greszczuk [17] and carry out a transient finite element analysis by imposing a time varying force on the target material. It is expected that the result of such an analysis could provide more close results to the results determined by MSC.Dytran. However, in this study this work is not performed because the main aim was to investigate the applicability of quasi-static approach in low velocity impact problems. Such a transient finite element analysis based on a time varying load is more time consuming compared to an MSC.Dytran analysis.

Based on the analysis performed on steel plate it can be concluded that quasi-static approach may provide reasonable results for very low velocity impact problems. However, in the 10 m/s range the discrepancy between the results of the quasi-static approach and MSC.Dytran solution can be very large especially at impact speeds close to 10 m/s. Therefore, the quasi-static approach should not be relied on.

For some of the cases MSC.Dytran is requested to output time history graphs. Middle node is observed and z position vs. time graph is sketched. Figures 24 and 25 give the variation of the displacement of the center node of the plate with respect to time for the 2 kg impactor corresponding to impact velocities of 0.1 m/s and 10 m/s, respectively. Displacement plots show that the plate bounces back following the impact. The maximum displacement values given in Tables 7-9 are read from these time history plots at the center node of the plate.

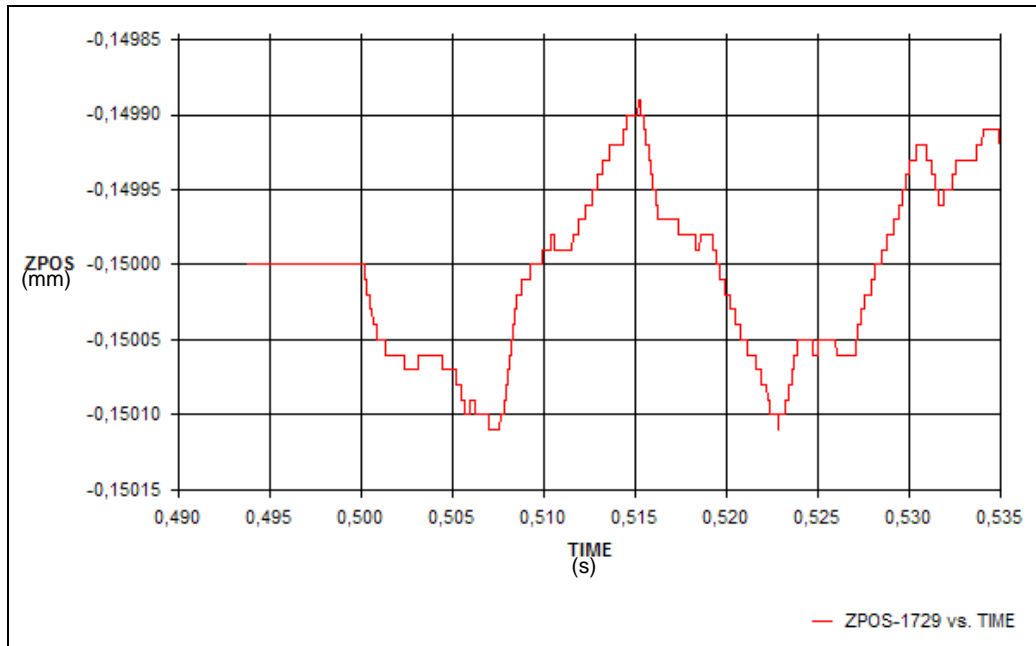


Figure 24: Z-Position vs. Time Graph for Steel Plate ($m=2\text{kg}$, $V=0.1\text{m/s}$)

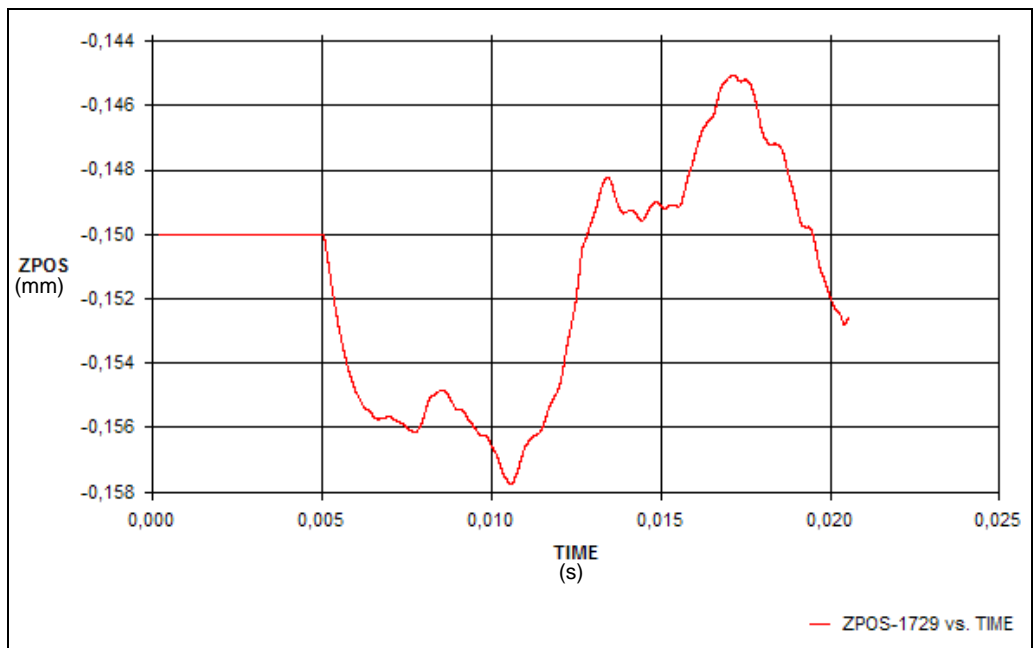


Figure 25: Z-Position vs. Time Graph for Steel Plate ($m=2\text{kg}$, $V=10\text{m/s}$)

It should be noted that the vertical position (Z-Position) is given in mm. Initial position of the steel plate is -0.15mm . Node 1729 is at the geometric center of the steel plate.

For the composite plate case the analysis results are similar to the previous one. Table 10 gives the results for the quasi-isotropic composite plate for an impactor mass of 0.2 kg. It can be seen that for the composite plate there is a significant difference between the peak deformation determined by the quasi-static approach and MSC Dytran solution.

Table 10: Maximum Deflection of Composite Plate for $m_{ball} = 0.2\text{kg}$

V_{ball} (m/s)	0.1	0.5	1	5	10
Dytran Solution (m)	-0.00186	-0.00467	-0.00696	-0.01595	-0.02288
Nastran Solution (m)	-0.00528	-0.0265	-0.0529	-0.264	-0.529

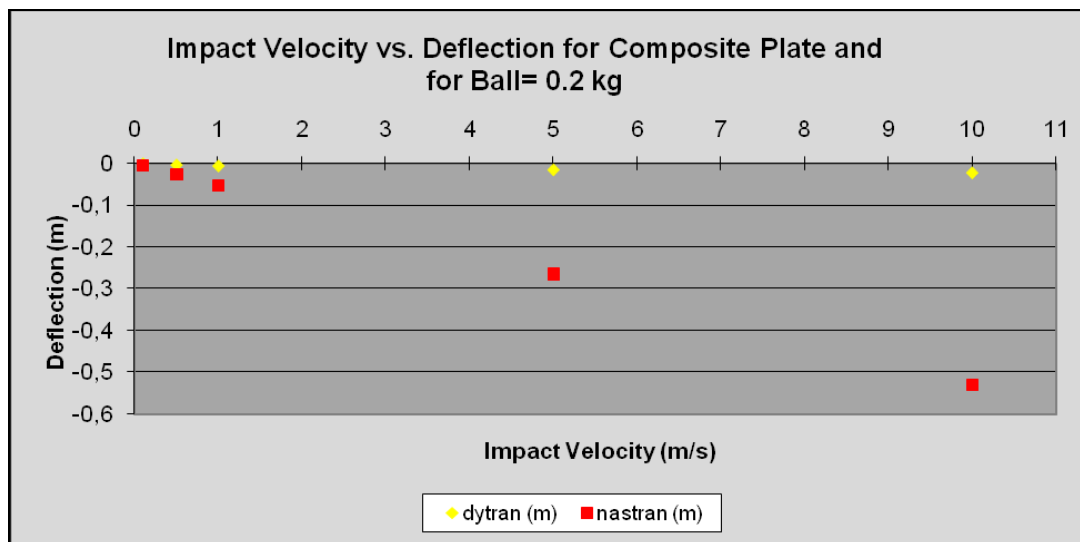


Figure 26: Comparison of Different Solution Methods for $m_{ball} = 0.2\text{kg}$

3.7. Impact Analysis of Composite Plates With Different Materials and Stacking Sequences

In this section the response of composite plates subject to impulsive loads is investigated. The main aim is to provide insight to the effect of stacking sequence on the stress and deformation response of the composite plate. As an initial analysis a simple composite plate of 30cm edge length is modeled. Carbon-Epoxy Woven is

used as composite material. According to the test results by Turgut [25] Carbon-Epoxy Woven has following material properties:

Table 11: Material Properties of Carbon-Epoxy Woven

$E_{11} = 46.26 \text{ GPa}$	$G_{12} = 3.8 \text{ GPa}$
$E_{22} = 46.26 \text{ GPa}$	$G_{23} = 2.7 \text{ GPa}$
$\nu_{12} = 0.03$	$G_{13} = 2.7 \text{ GPa}$
$\rho = 1.19 \times 10^{-6} \text{ kg/mm}^3$	$t = 0.133 \text{ mm}$

Figure 27 shows the finite element model of the composite plate used in the analyses.

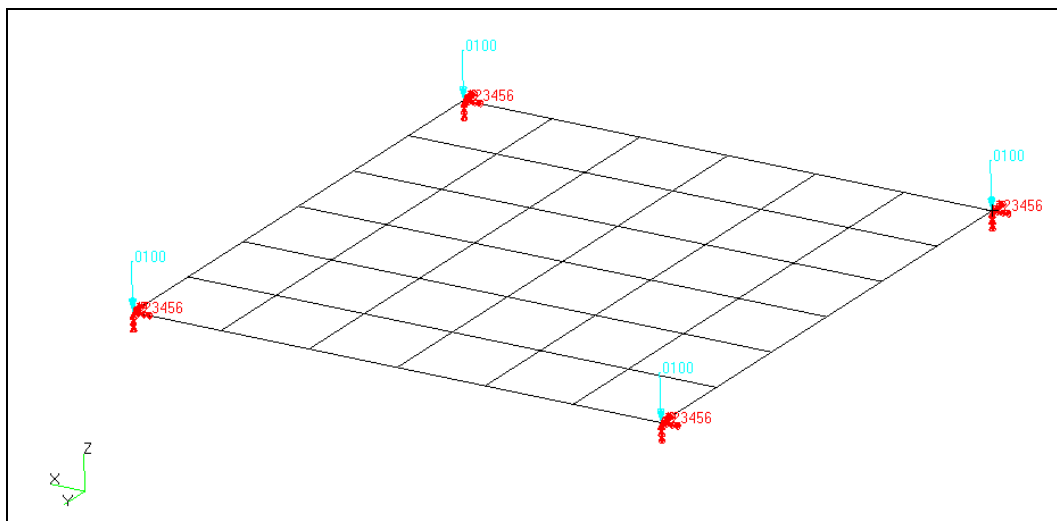


Figure 27: Carbon-Epoxy Plate Model

As shown in Figure 27 plate is clamped from all sides and an impulsive force of 100kPa is applied for 0.5 s and solution is performed in MSC Dytran. The analysis is repeated for different stacking sequences for 8 plies. Maximum stress and deflection results are tabulated in Table 12.

Table 12: Maximum Stress and Deflection Results of Test Case

Stacking Sequence	Max. Stress (MPa)	Max. Deflection (mm)
[0/0/0/0] ₂	83.468	0.29666
[0/45/0/45] ₂	72.333	0.42215
[45/0/0/45] _s	55.701	0.56534
[0/45/0/45] _s	90.188	0.35234
[45/45/0/0] _s	57.753	0.7908
[0/0/45/45] ₂	71.577	0.44096
[45/45/45/45] ₂	60.731	1.0889
[45/0/45/0] ₂	90.013	0.45616
[0/45/45/0] ₂	90.702	0.39593
[45/0/45/0] _s	56.185	0.67569
[0/0/45/45] _s	89.688	0.32402
[45/45/0/0] ₂	88.833	0.50402

From results given in Table 12 it is clear the stacking sequence significantly affects the peak stress and deflection values of the composite plate. Such a simple study shows that in designing composite structures one should make a stacking sequence study to decide on the best lay-up configuration to use in the particular design at hand.

The analysis above can be repeated if the impulsive force is replaced with an impactor ball which is projected on a similar plate as shown in Figure 28.

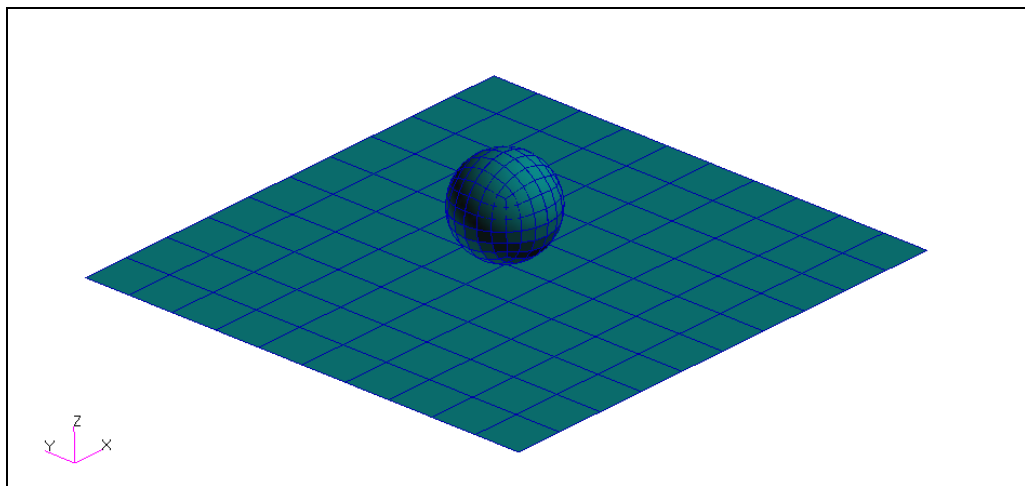


Figure 28: Low velocity impact model of a ball impactor on a target plate

If a ball impactor with 10 mm radius is projected at a speed of 2 mm/s on a target plate with 10 cm edge length the stress and maximum deflection varies as the stacking sequence changes. Results for 6 different cases are tabulated in Table 13.

Table 13: Maximum Stress and Deflection Results of Test Case - 2

Stacking Sequence	Max. Stress (MPa)	Max. Deflection (mm)
[0/0/0/0] ₂	13.988	0.248
[45/45/45/45] ₂	14.061	0.251
[45/0/45/0] ₂	13.749	0.25
[0/0/45/45] ₂	13.894	0.251
[0/0/45/45] _s	13.985	0.249
[45/0/0/45] _s	14.217	0.249

The results for both impulsive force and low velocity impact show that stacking sequence directly affects the stress and strain behavior of the whole laminate. This phenomenon for “Güventürk” Mini UAV is analyzed in the following chapters.

CHAPTER 4

DESIGN AND STRUCTURAL LAYOUT OF “GÜVENTÜRK” MINI UAV

4.1. Description and Specifications

As the demand on Unmanned Aerial Vehicles increased, Middle East Technical University Aerospace Department took part in a project financed by State Planning Organization. Following the requirements of the project, METU Aerospace Engineering UAV Research Group designed and built a Mini UAV that is capable of performing observation, reconnaissance and surveillance missions autonomously inside a mission range of 10 km.

“Güventürk” Mini UAV is a hand launched airplane with belly landing capability by the virtue of folding propeller. The airplane is designed to carry an analog or IR Camera. It was designed to be a lightweight platform so that it could be hand launched. Maximum take-off weight of the airplane was limited to 4.5 kg with a maximum payload weight of 0.5 kg. Long wing span of 2.20 m gives the opportunity to have a small stall speed. 9 m/s stall speed makes belly landing easier. The airplane is also equipped with the commercial autopilot MicroPilot [26] which can fly the airplane autonomously.

A photo showing “Güventürk” after hand launch is given in Figure 29.



Figure 29 “Güventürk” in operation
The specifications of “Güventürk” are summarized in Table 14.

Table 14: Specifications of “Güventürk” Mini UAV

MTOW	4.5 kg	Empty Weight	3 kg
Wing Span	2.20 m	Length	1.35 m
Endurance	90 min	Range	10 km
Maximum Speed	23.5 m/s (45kt)	Stall Speed	9 m/s (17kt)
Cruise Speed	13.5 m/s	Cruise Altitude	300 m

The solid model of “Güventürk” that was built in CATIA is the one of the basic milestones of the whole design period. It is not only a visual representation of the UAV, but also starting point of the CFD and structural analyses. In this study, the skin of the aircraft is transferred from CATIA to MSC.Patran and belly landing analysis is accomplished. CATIA model of the UAV is given in Figure 30.

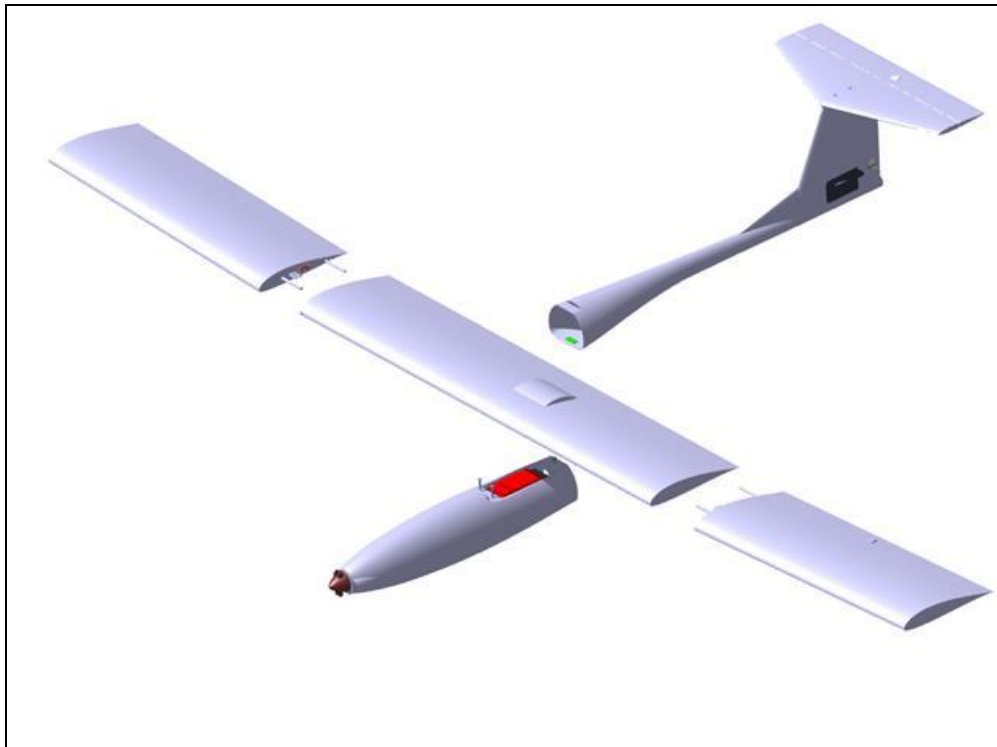


Figure 30: Solid Model of “Güventürk”

CATIA model is used to form molds as well. After modeling the whole vehicle in CATIA, a foam male mold is produced by the hot wire foam cutting CNC machine. Female molds are made of polyester. During the production, carbon fabric is widely used on this platform with epoxy matrix. Underneath of the fuselage is reinforced by means of Kevlar which gives additional elasticity against the impact loading. Internal structure is stiffened by balsa wood covered by carbon fabric. The spar inside the wing is made of Styrofoam covered again by carbon fabric. The spar is cut from a block of Styrofoam in the requested shape and thickness; then, by vacuum bagging method it is covered by carbon fabric. Curing is completed at room temperature. Schematic of spar and internal structure is given in Figure 31.

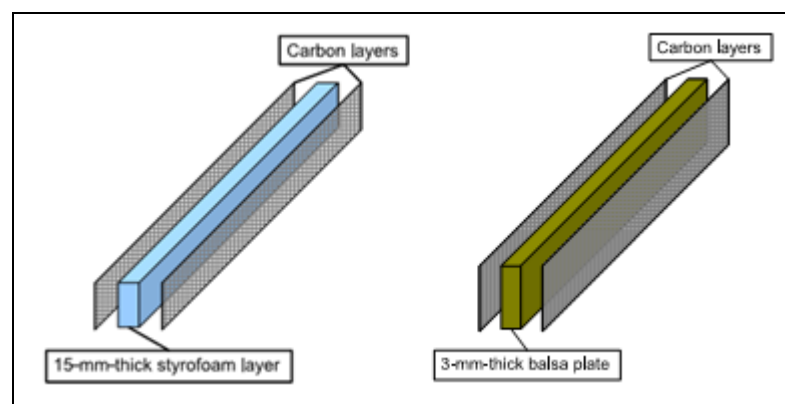


Figure 31: Schematic of spar and internal structure [25]

After the production of “Güventürk” mini UAV is completed it is divided into 5 parts: Fuselage, horizontal tail, mid wing and two outer wings. In this way, maintainability is improved and transportation is made easier.

A carry bag is also built to ease the flight test operations. The packed aircraft can be made ready to fly in approximately 5 minutes. First, the middle wing and horizontal tail is fixed to the fuselage by plastic screws; then, outer wings are attached to the middle wing by sliding in through the spar holes; and finally, putting the battery on board by a strip of Velcro.

4.2. Belly Landing

At the end of a successful mission, when “Güventürk” descends to the ground, the only thing that is expected is a safe landing. During the final leg of approach electric motor is cut off and the propeller folds. Then, the aircraft flies at minimum airspeed

possible which is very close to stall speed. As a result of the high aspect ratio of wing, approach velocity is very low.

The aircraft approaches to the ground at 5° - 10° ; whereas, the approach angle becomes smaller when altitude above ground level becomes 3-6 ft or 1-2 m. Considering an ideal landing case, at the time of touch down, the approach angle should be less than 3° .

The weight issue also becomes extremely important in belly landing for such mini unmanned airplanes. Low weight implies low stall speed and for an airplane landing on its belly if the stall speed is low, then the speed of the airplane can be reduced further before touchdown. Therefore, low weight design of such mini unmanned airplanes is a necessity also from landing point of view. Ideal landing would be a landing without a glide which implies that the forward velocity of the airplane should be almost zero. Such an ideal landing cannot be achieved in practice, however by clever design the stall speed of the airplane can be reduced as much as possible. In the current design high lift devices such as flaps were not integrated to the airplane. Therefore, the landing speed of the airplane could not be decreased further. In addition, depending on the mission requirements there were demands for installing additional systems on the airplane which further increased the weight of the airplane resulting in an increase in the stall speed. Under such circumstances the forward velocity of the airplane during landing cannot be decreased. High forward speed is not as critical as high vertical speed during landing. However, under certain circumstances during the skidding period on the ground, an obstacle on the way may induce high load on the airplane if the forward speed is high during landing. Therefore, low forward speed is a desired requirement. In addition to low forward speed, the vertical descent speed of the airplane is also a crucial factor in the structural integrity of the airplane. During landing there can be unpredictable factors that may prevent the air vehicle from a safe landing. Gust, for instance, might cause the aircraft to suddenly hit the ground suddenly when the aircraft is in close proximity to the ground. Based on the experience obtained during the flight tests of "Güventürk" it is concluded that during windy weathers belly landing-associated failures of the sub-structures of the airplane increased. Actually, when the wind speed is high this can be used to advantage during landing by landing against the wind so that the forward speed of the airplane can be decreased to such a level that landing can be performed smoothly. However, in the windy weathers very frequently

there are changes in the wind speed and its direction which causes the pilot to lose control and execute hard landing in order to prevent a full crash. Therefore, gust is considered to be the major factor affecting the smooth or hard landing phenomenon of the unmanned air plane. Another reason for a hard landing may be the external pilot. Especially, an inexperienced pilot might land the airplane with a higher vertical speed which may induce higher landing loads on the airframe. The advantage of autonomous landing capability can be appreciated more during belly landing. With autonomous landing the pilot related events causing hard landing may be minimized. However, the main drawback in autonomous landing is the time consuming experimentation that has to be carried out before successful landing can be achieved.

In any case, it should be expected that during belly landing the airframe might be exposed to impact loads due to various reasons which may not be always controlled. Figure 32 shows “Güventürk” during a belly landing. This picture shows an ideal landing on a grass-soil mixed ground.

Based on the explanations made in this section, it can be concluded that the impact velocities encountered under most belly landing cases can be considered as low velocity. Therefore, the main goal of this thesis, as it was mentioned in the introduction section, is to perform the structural analysis of the airframe of the mini unmanned air vehicle under low velocity impact loads that may be induced during belly landing. The next section summarizes the low velocity impact analysis results of the mini unmanned air vehicle and draws conclusions.



Figure 32: Belly Landing of “Güventürk”

CHAPTER 5

LOW VELOCITY BELLY LANDING ANALYSIS OF “GÜVENTÜRK”

5.1. Fuselage Finite Element Model

In this chapter, the belly landing analysis of “Güventürk” Mini UAV is accomplished in light of the information obtained by the analysis made in third chapter. As it is stated in Chapter 3.7, variation of stacking sequence significantly affects the peak stress. In order to optimize the design of composite parts of “Güventürk”, the whole fuselage model is analyzed by applying different layup configurations. The main aim of this chapter is to accomplish a stacking sequence study for the fuselage and guide the designer of “Güventürk” in fuselage manufacturing part. As a preliminary study, analysis is executed for the fuselage skin only. Then, the fuselage is combined with the internal structure, and that configuration is analyzed in detail. Finally, the combination of wing and fuselage is analyzed to have some ideas about the effects of belly landing on the whole structure. Because of the limitations in computer resource and very long solution times of the explicit finite element solution the vertical and horizontal tail plane is left out of the analysis. It should be noted that based on the flight test experience of the air vehicle horizontal and vertical tail structure is not affected adversely by the hard belly landing. Therefore, leaving the tail system out of the analysis can be justified. However, as a future work the tail system could also be included in the analysis to see the effect of belly landing on the behavior of the tail system.

During the design of “Güventürk” Mini UAV, Dassault’s Computer Aided Three-Dimensional Interactive Application “CATIA” v5 r13 was employed. Fuselage, wing, tail and internal structure were modeled in detail. To transfer the UAV model from CATIA to MSC.Patran, CATIA model is first exported into IGES format. IGES is nomenclature of “The Initial Graphics Exchange Format” and defines a data format that allows the digital exchange of information among computer aided design (CAD) programs [31]. IGES file is then imported into MSC.Patran. The imported model of

the fuselage is given in Figure 32. The details of importing a model into MSC.Patran are given in Appendix A.

The aircraft is imported into MSC.Patran such that the principle axes of it coincide with the coordinate system of MSC.Patran (Figure 33). In this manner, x axis becomes the longitudinal axis, y axis becomes lateral axis and z axis becomes vertical axis.

After importing the model, wing and tail is cut out and the fuselage is scaled up so that the length of fuselage becomes 1350 units. Since the real length of fuselage is 1.35 m, each unit in MSC.Patran becomes 1 mm. The other units used are given in Table 15.

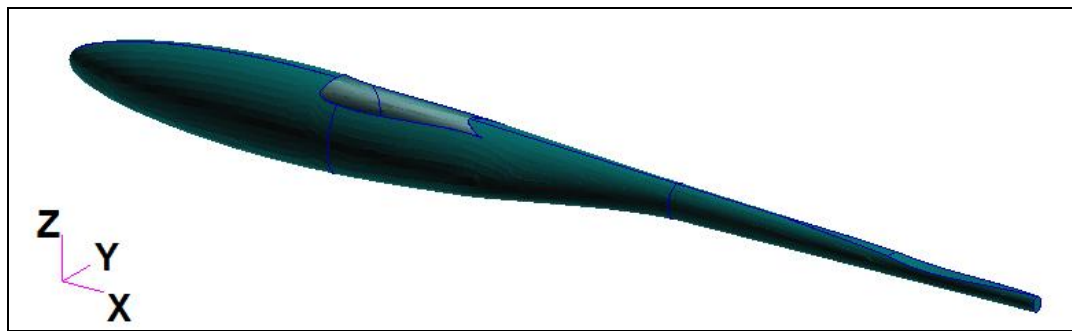


Figure 33 Imported fuselage geometry and the principle axes

Following table shows the units used in MSC.Patran modeling.

Table 15 Units used in MSC.Patran Model

Length	mm
Velocity	mm/s
Pressure	MPa
Density	kg/mm ³

Initially, the preliminary analysis is completed with fuselage skin only. QUAD Mesh is applied to fuselage skin with a target global edge length of 10 mm. Due to the curvatures some parts of the fuselage don't allow to apply isomesh; therefore, pavermesh is used at certain portions. The absence of the tail boom resulted in an open area at the end of the tail boom and that area is closed to gain structural rigidity. Meshed fuselage model is given in Figure 34 and 35. The effect of mesh size on the analysis is given in Appendix D.

After meshing is completed uniformly distributed 3800 nodes are selected. 1 gram of inertial load is applied to each of them; therefore, the whole structure is loaded with 3.8kg of uniformly distributed inertial mass. Since the maximum takeoff weight of the UAV is 4.5 kg and empty weight is 3 kg, the inertial load is reasonable.

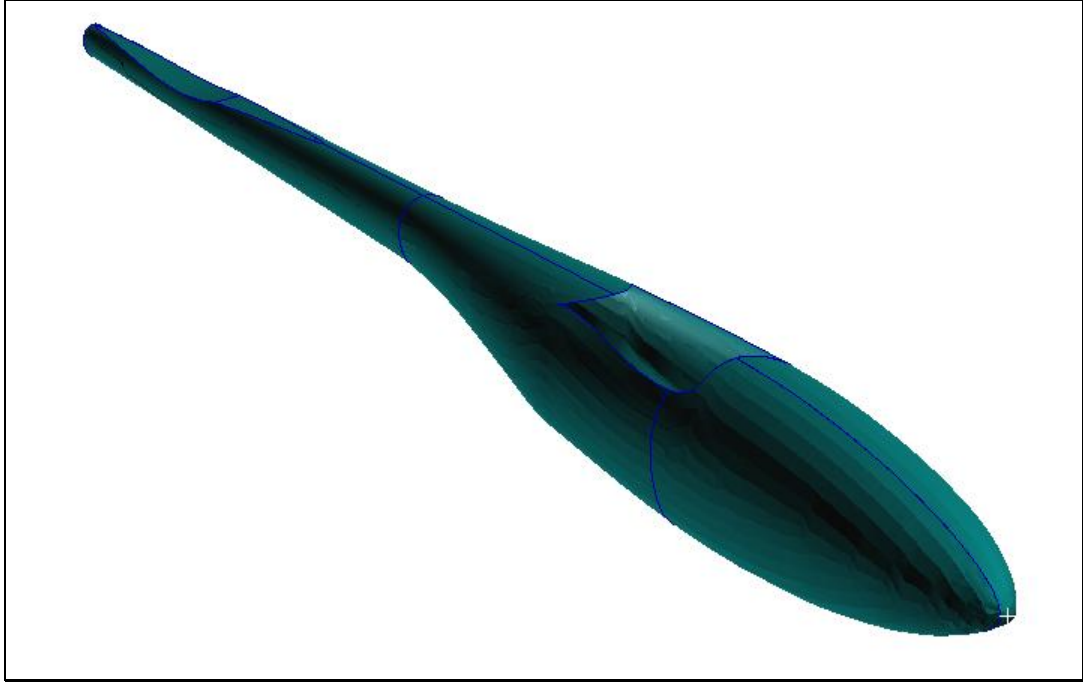


Figure 34: Meshed fuselage solid model

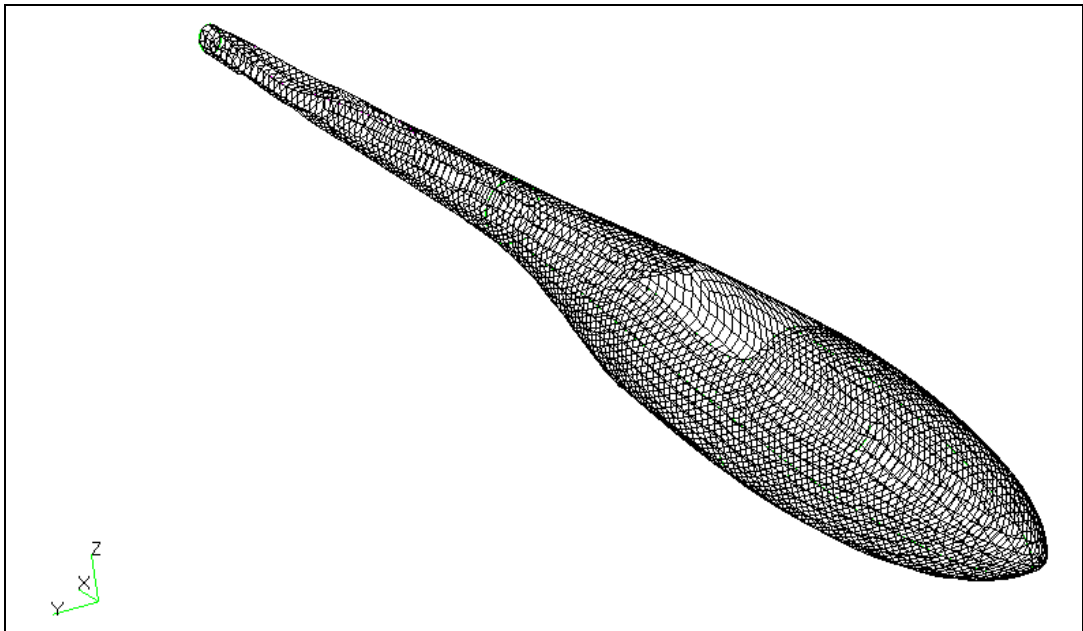


Figure 35: Meshed fuselage hollow model

5.2. Impact Modeling

During a typical landing an aircraft approaches at a velocity which is calculated by adding a safety margin to the stall speed of the particular aircraft. Safety margin is usually 20%-25% in excess of stall speed for commercial airplanes. [29] This can be even less for unmanned air vehicles with auto landing capability when the autopilot has a high precision control on the attitude angles and airspeed. Approach angle is typically 2.5-3.5 degrees followed by the flare maneuver just before the touchdown [30]. Flare maneuver is an important part of the landing by which the airspeed and vertical speed (e.g. vario) of the aircraft is decreased.

For the belly landing analysis part of this thesis, optimum conditions are not considered; on the other hand, operational conditions are simulated. Belly landing is assumed to be completed by an external pilot; therefore, tough landing conditions with steep approach angle and higher airspeed without flare maneuver are modeled. Stall speed of "Güventürk" is given as:

$$V_s = 9m/s \quad (65)$$

With a safety factor of 4/3

$$V_{approach} = 9m/s \cdot \frac{4}{3} \quad (66)$$

$$V_{approach} = 12m/s$$

Assuming an approach angle of 3.5 degrees vertical velocity becomes:

$$V_{vertical} = 12m/s \cdot \sin(3.5) \quad (67)$$

$$V_{vertical} = 0.733m/s \approx 0.7m/s$$

Vertical and approach velocities are given as initial velocity:

$$V_x = -12000mm/s$$

$$V_y = 0 \quad (68)$$

$$V_z = -700mm/s$$

No initial angular velocity is given. Therefore,

$$w_x = w_y = w_z = 0 \quad (69)$$

The initial velocities calculated above are kept constant for all of the analysis cases. Analyses are repeated for different composite laminate materials and layups. Impact surface is also changed from rigid to soil and differences in results are observed.

According to the given initial parameters, the impact case is formed as shown in Figure 36.

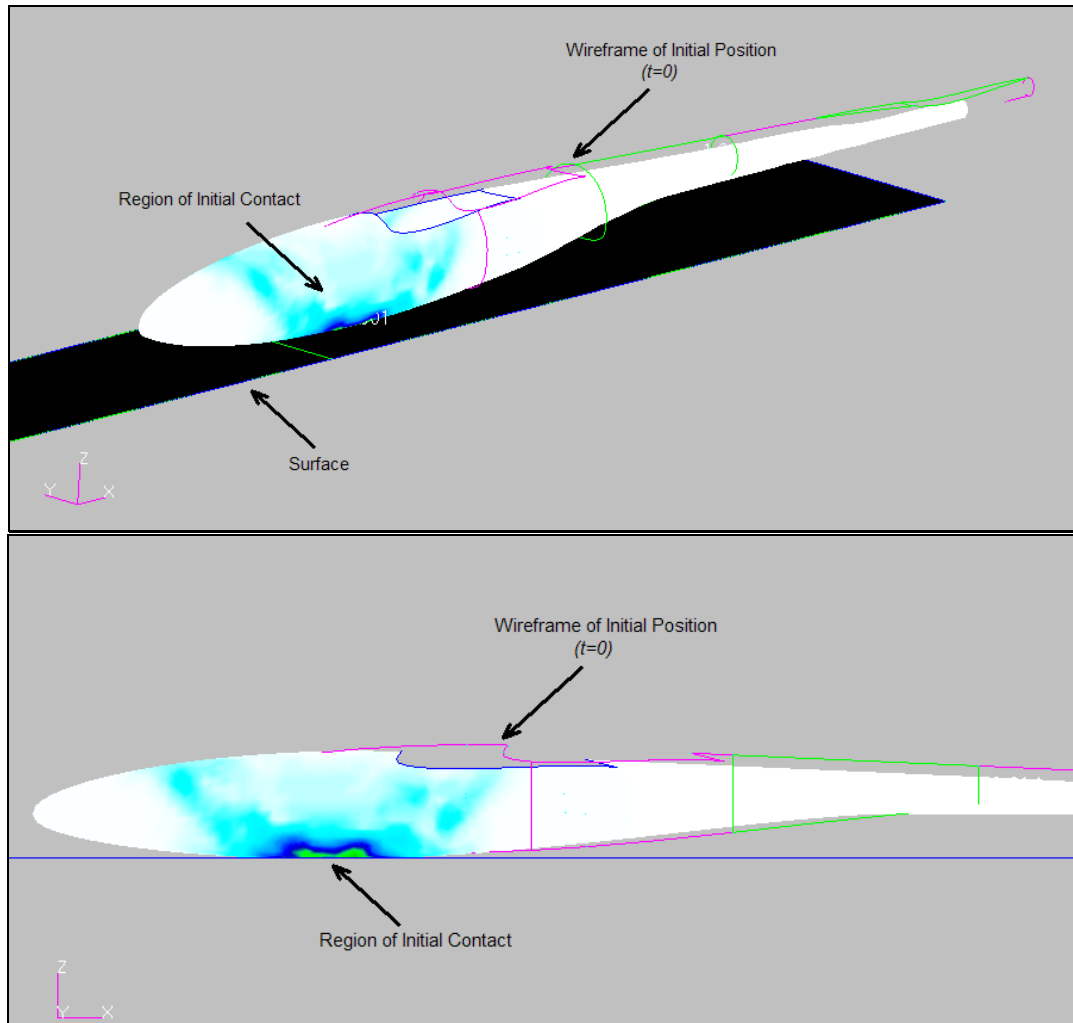


Figure 36: The contact instant of impact case ($t=0.009$ s)

The technical specifications of the computer on which the analyses are conducted are given in Table 16. The clock rate of Central Processing Unit (CPU) and the capacity of the random access memory (RAM) are directly related to analysis time. Access speed of hard disk drive (HDD) and overall compatibility of hardware are also factors that affect the performance slightly. For pre and post processing the performance of graphics card is an important parameter.

Table 16 Specifications of the analysis computer

CPU	Intel Core 2 Duo T5600 (1.83GHz, 667 MHz FSB, 2MB Cache)
RAM	1 GB DDR2 (dual channel)
HDD	120 GB IDE
Graphics Card	256 MB NVIDIA GeForce Go 7300

For the cases mentioned in this chapter, the analysis durations vary from a few minutes to tens of hours. A summary of approximate computational durations is given in Table 17.

Table 17 Typical durations of analysis for different cases

Case	Typical Duration of Analysis
Fuselage shell only (rigid surface)	10 minutes
Fuselage shell only (soil surface)	12 minutes
Fuselage shell with internal structure (rigid surface)	25 minutes
Fuselage shell with internal structure (soil surface)	30 minutes
Fuselage shell with internal structure and wing shell only (rigid surface)	3 hours
Fuselage shell with internal structure and wing shell only (soil surface)	4 hours
Fuselage shell with internal structure and wing shell with internal structure (rigid surface)	27 hours

5.3. Fuselage Shell Landing Analysis On Rigid Surface

The first belly landing analysis of “Güventürk” Mini UAV is completed with considering external skin only. The imported model shown in Figure 34 is covered

with carbon/epoxy laminate with 45 degrees orientation with respect to x axis. Building of laminate is made in Laminate Modeler Tool of MSC.Patran. Laminate Modeler Tool is a powerful modeling tool for composite laminates. In real life, when covering a part with composite laminate one should consider the convex shape of the body in order to prevent buckling of the composite fabric. The same situation also exists in Laminate Modeler. According to the shape of the body, laminate modeler calculates the maximum strain. The details of Laminate Modeler Tool are given in Appendix B. In this study, the left and right side of the fuselage is covered separately. Figure 37 shows the composite layup on the body. Red arrow is the application point where the laminate first touches to the body. Rest of laminate is laid according to the application point. Green arrow is the reference direction. The angle of composite lamina is given according to reference axis. If the reference angle is 0, that means composite fibers are in same direction with the reference axis.

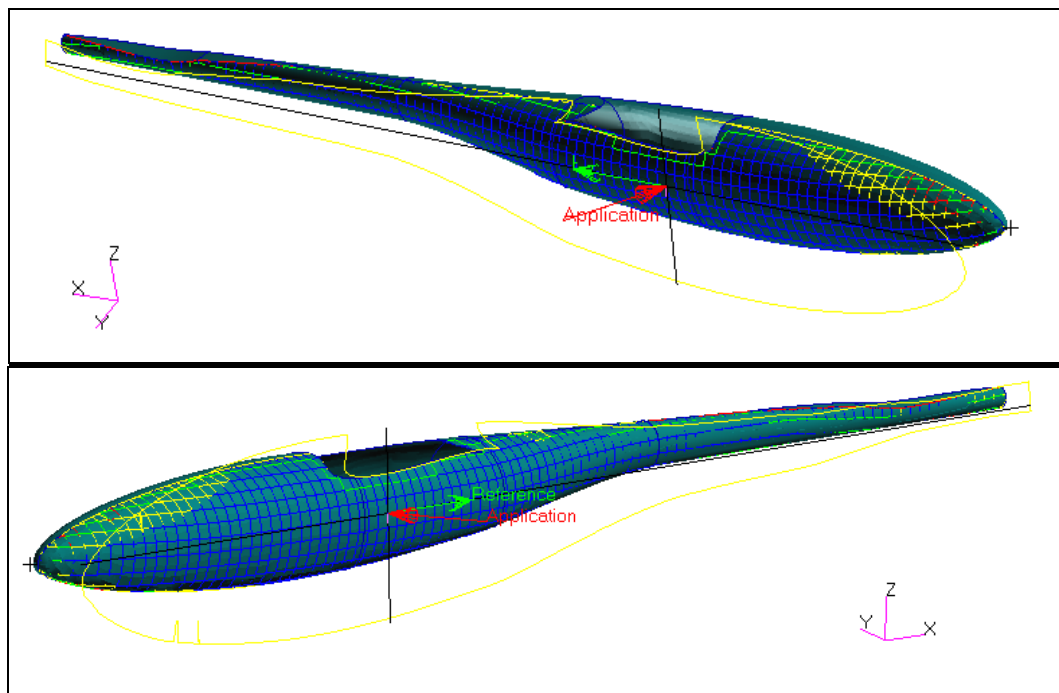


Figure 37: Composite laminate layup for the left and right hand side of the body

After building a layup of 12 plies the fuselage shell is impacted on the rigid surface. It should be noted that since the fuselage shell has no internal structure, the stiffness of the fuselage is very low due to the absence of bulkheads.

The analysis is run for 20000 time steps which is nearly equal to 0.09 s of duration in real time. Throughout 0.09 s, the maximum stress, which is just above 350 MPa, is observed at Element 6116. The location of Element 6116 is at the bottom of the fuselage and given in Figure 38.

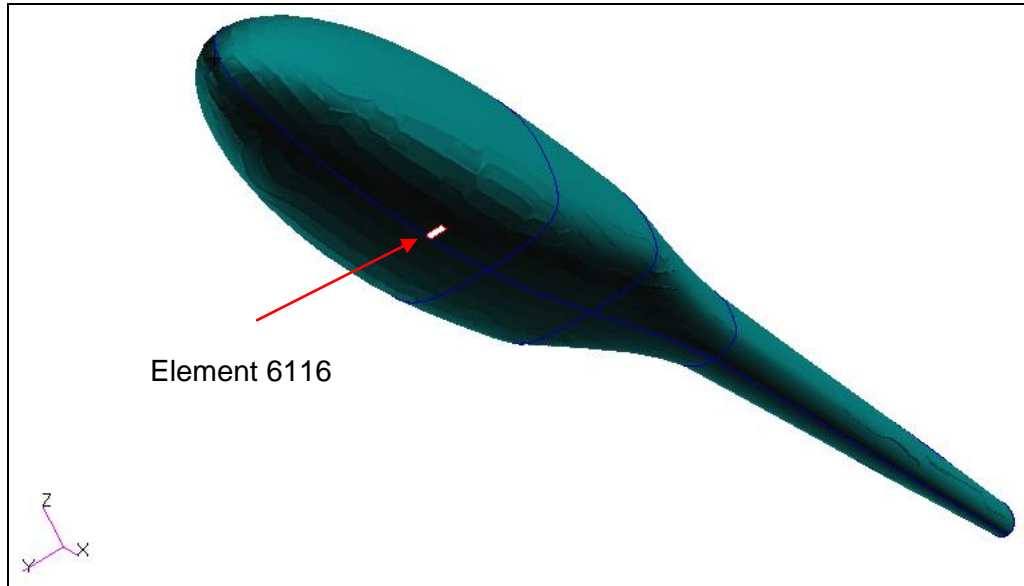


Figure 38: Location of Element 6116

At any time step, for each element there is a set of stress result. Since the fuselage is covered by composite laminates, it is possible to have different stress results at different layers. The stress result for each element is given for inner, middle and outer layers. Inner, middle and outer layers are defined according to the surface normal of the corresponding element. In this case the maximum stress for Element 6116 is occurred in the inner layer. Effective Stress vs. time graph for Element 6116 is given in Figure 39.

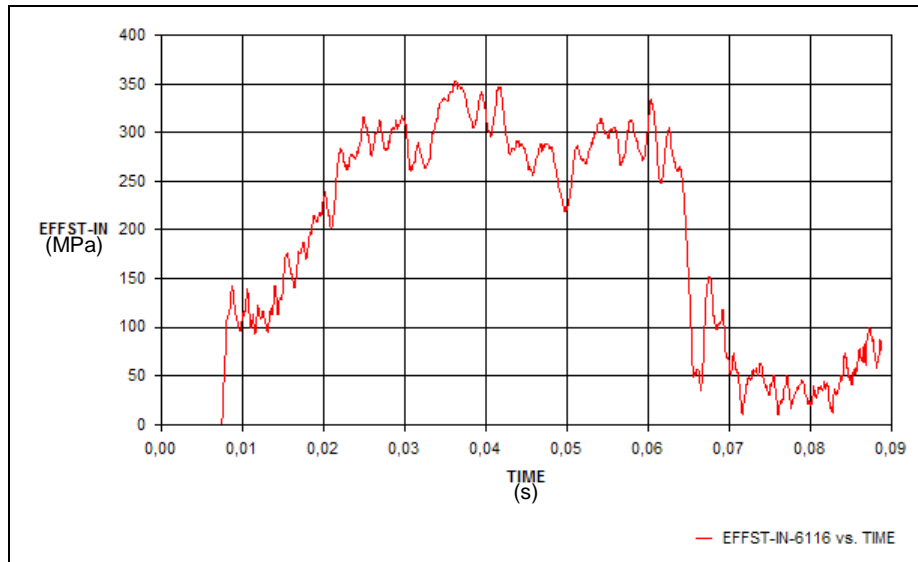


Figure 39: Stress (MPa) vs. Time (s) graph for Element 6116

According to Figure 41 it is possible to say that the body contacts with the ground before $t=0.01$ s. A sudden rise of stress in Element 6116 is followed by an almost linear increase up to 350 MPa. The noisy behavior of stress vs. time diagram shows nature of stress waves. After $t=0.06$ s stress relaxation starts and decrease in stress is observed. The deformation observed on the shell can be clearly seen in Figure 40.

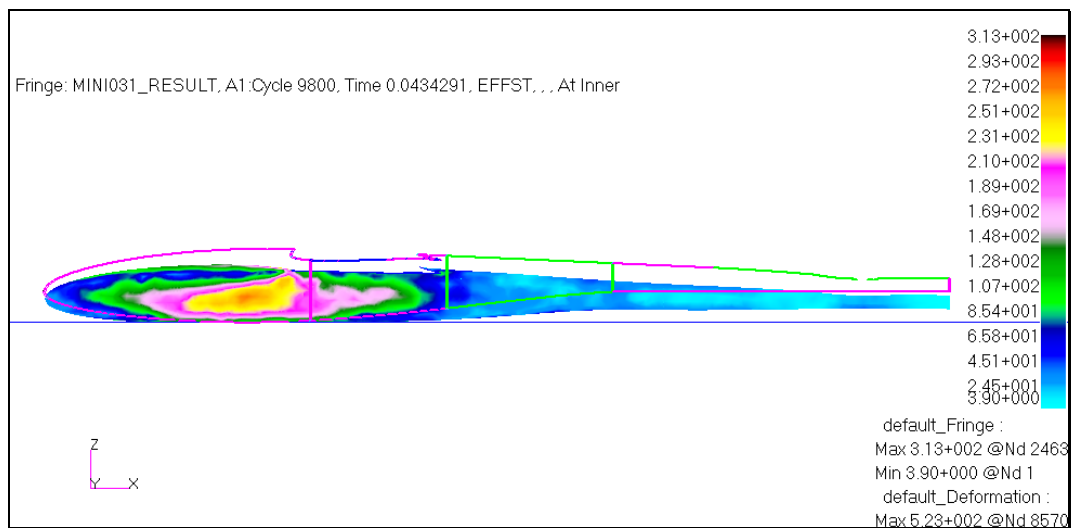


Figure 40: Analyzed fuselage model at $t=0.04$ s and overlapped original form in wireframe

Stress contour vs. time visual for the whole fuselage shell is another result output. As it is mentioned before, the analysis is run for 20000 steps and in every 2000 steps a screenshot is taken. Inner stress contour vs. time graphs are given in Figure 41-43. Figure 41 shows the initial contact and stress propagation up to 0.018 s. Figure 42 shows further stress development on the side of the fuselage between $t=0.027$ to 0.053 s. In Figure 43, stress waves move through the tail boom and stress relaxation of the side can be examined.

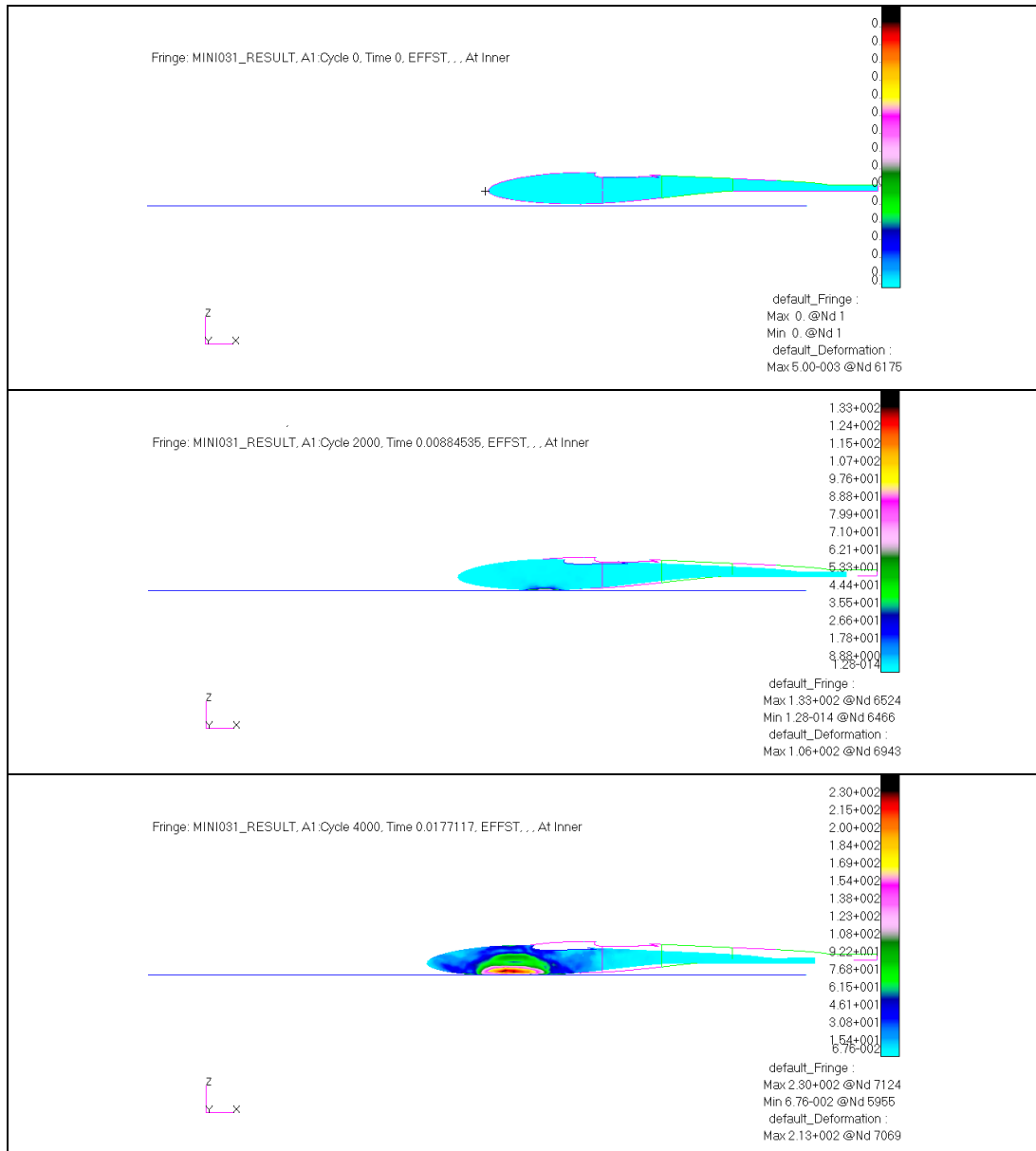


Figure 41: Stress contours at $t=0$, $t=0.009$, $t=0.018$ (s)

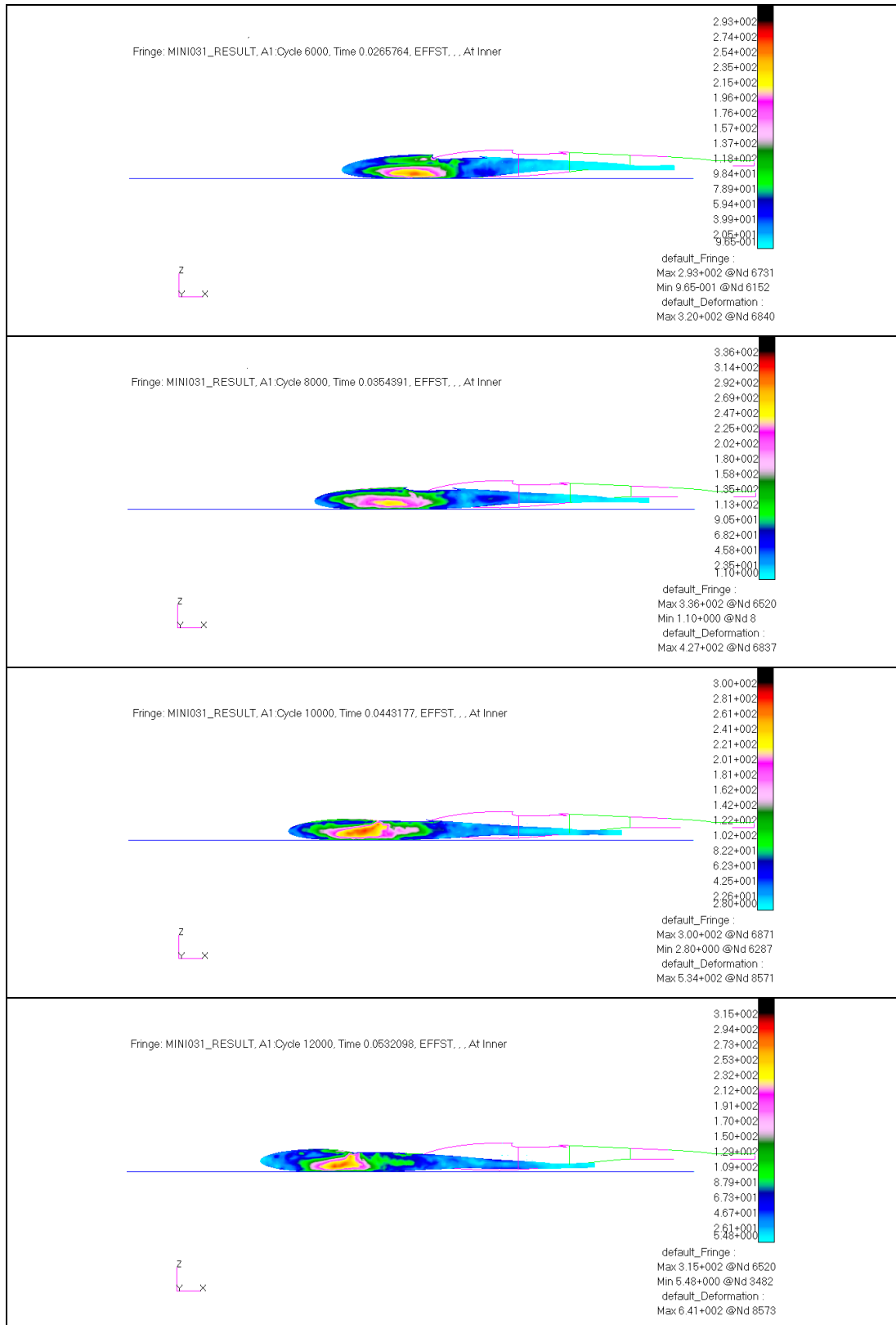


Figure 42: Stress contours at t=0.027, t=0.035, t=0.044, t=0.053 (s)

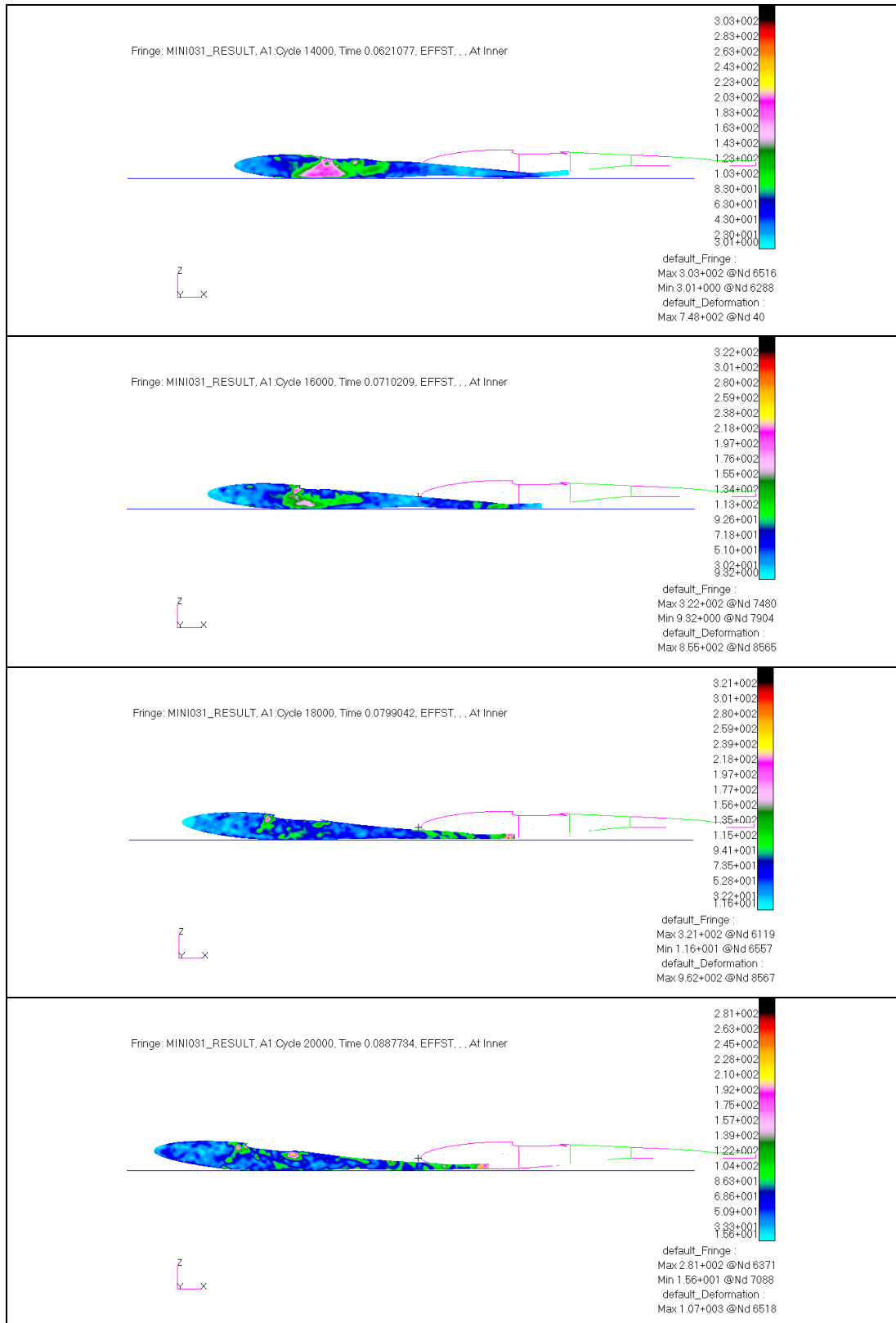


Figure 43: Stress contours at t=0.062 t=0.071, t=0.080, t=0.089 (s)

In order to observe the deformation precisely, a node from top of the shell and another node from bottom of the shell are selected and corresponding z-position vs. time graphs are drawn. Thus, it is now possible to observe the vertical deformation of the fuselage shell without any bulkheads. Location and coordination of top and bottom nodes is given in Figure 44 and z-position vs. time graph is given in Figure 45

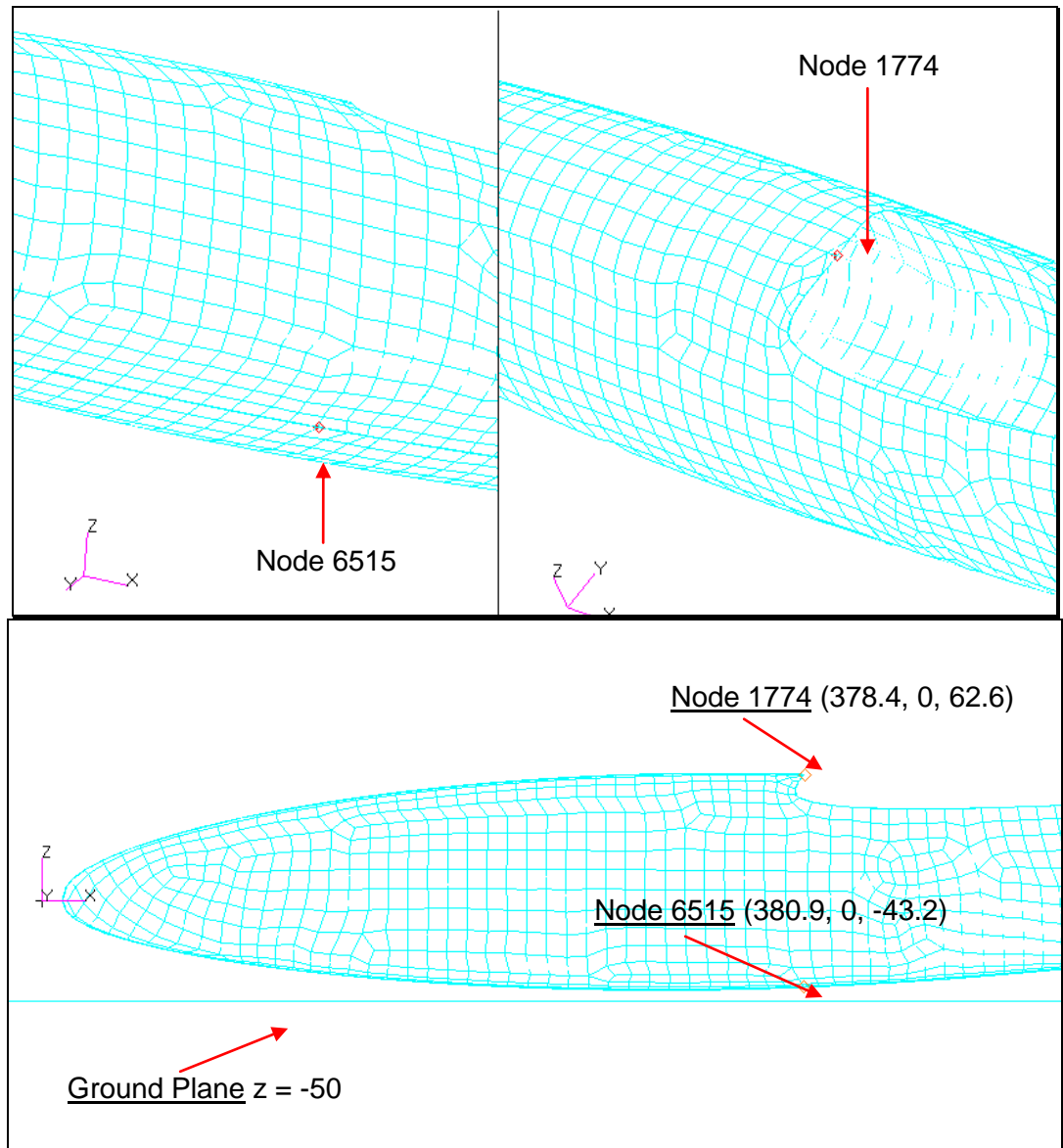


Figure 44: Location and coordination of bottom (node 6515) and top (node 1774) nodes (coordinates in mm)

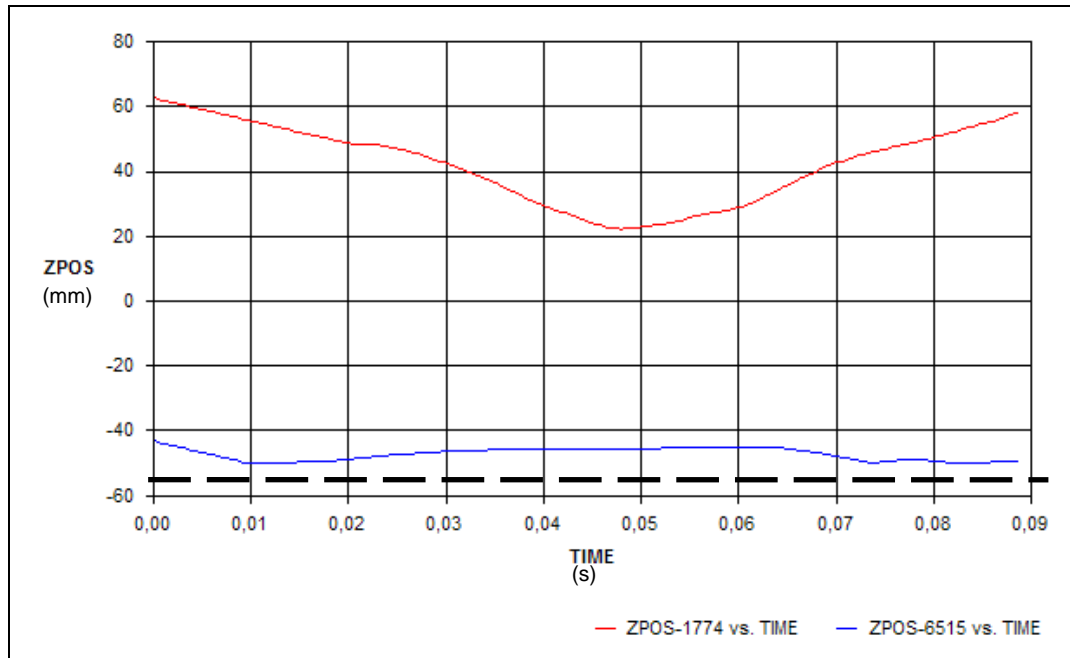


Figure 45: Z-Position (mm) vs. Time (s) graph for top (red), bottom (blue) nodes and ground (dashed line)

A combined observation of Figures 41 and 45 indicates that after the bottom of fuselage touches the rigid surface it bounces back. However, top side of the body is still approaching to the ground since the stress waves are not arrived to there yet. After $t=0.05$ s the fuselage shell starts to expand again until the initial form is nearly gained at $t=0.088$ s. When observing these graphs, one should always keep in mind that no failure criterion is applied. The body is assumed to be completely elastic, and the main emphasis is placed on the deformation and stress behavior of the airframe during belly landing. Such information is enough to aid the designer in making design decisions.

5.4. Fuselage Shell Landing Analysis On Soil

Fuselage shell landing analysis is repeated after replacing the mechanical properties of rigid surface with the ones similar to soil. The main purpose of this study is to have an idea about the changes in result when the same impact scene is reconstructed by considering a flexible target that can be assumed to be soil. More dedicated analyses are conducted by Ramalingam, V. K. and Lankarani, H. M [31] by using LS-DYNA.

There are numerous textbooks and studies concerning mechanical properties of soil [32, 33]. Bowles [32], gives the density and the ranges for elastic modulus and Poisson's ratio for gravel & sand as:

$$\rho = 4.1913 \text{ E} - 9 \text{ kg} / \text{mm}^3$$

$$E = 100 \text{ MPa} - 200 \text{ MPa}$$

$$\nu = 0.30 - 0.40$$

In the study, the average of the values above is selected:

$$E_{soil} = 150 \text{ MPa}$$

$$\nu_{soil} = 0.35$$

Shear modulus and bulk modulus is interrelated to elastic modulus and poisson's ratio:

$$\nu = \frac{E}{2G} - 1 \quad (70)$$

$$\nu = \frac{1}{2} - \frac{E}{6K} \quad (71)$$

Solving Equation (70) for G:

$$G = \frac{E}{2(\nu + 1)} = \frac{150}{2(0.35 + 1)} = 55.56 \text{ MPa} \quad (72)$$

Solving Equation (71) for K:

$$K = \frac{E}{6(1/2 - \nu)} = \frac{150}{6(0.5 - 0.35)} = 166.67 \text{ MPa} \quad (73)$$

Defining the soil as elastic material and plugging in mechanical properties for the target material the analysis is repeated.

The results indicate that the shell itself has no impact resistance since z-position vs. time graph is almost the same as the previous case. Both top and bottom nodes moves a few millimeters down since the bottom nodes penetrate into the soil; however, total vertical deformation of the fuselage remains nearly the same.

z-position vs. time graph is given in Figure 46.

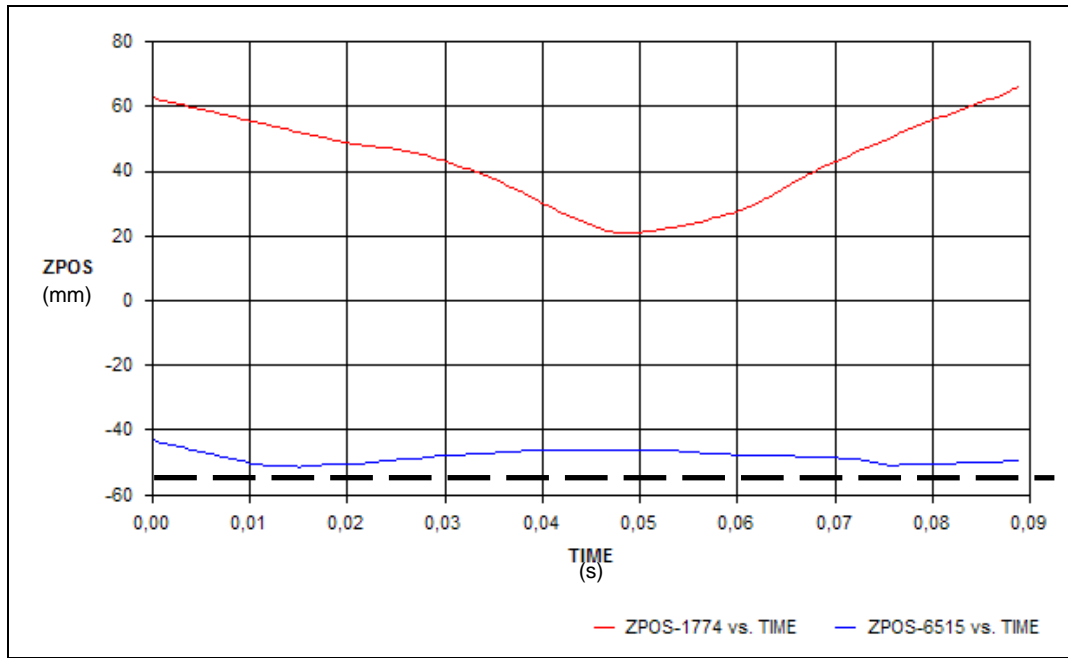


Figure 46: z-position vs. time graph for top (red), bottom (blue) nodes and the level of ground (dashed line)

For the soil impact case maximum stress also occurs in the same element. Stress vs. time graph for element 6116 for the soil impact case is given in Figure 47 together with the stress vs. time curve for the rigid target case. Figure 47 shows that there is no significant difference between landing on rigid surface and landing on soil surface cases as far as the stress on element 6116 is concerned. The peak at $t=0.04$ s for soil case is unexpected and can be explained by numerical error of the finite element solution.

It should be noted that at the first contact, the rise of stress for the soil surface case is lower than the rigid surface case, which indicates that the impact energy is dissipated by the elastic behavior of soil.

The stress contour graph is given in Figure 48. It shows the screenshot of effective stress result at $t=0.039$ s.

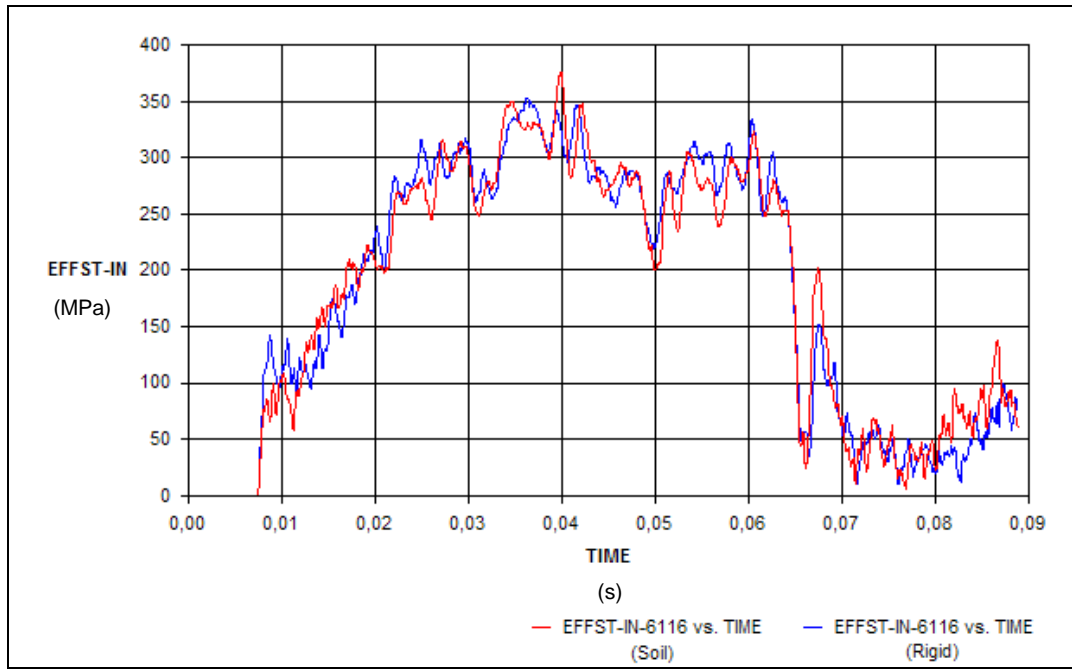


Figure 47: Stress (MPa) vs. Time (s) graph for fuselage shell impact case

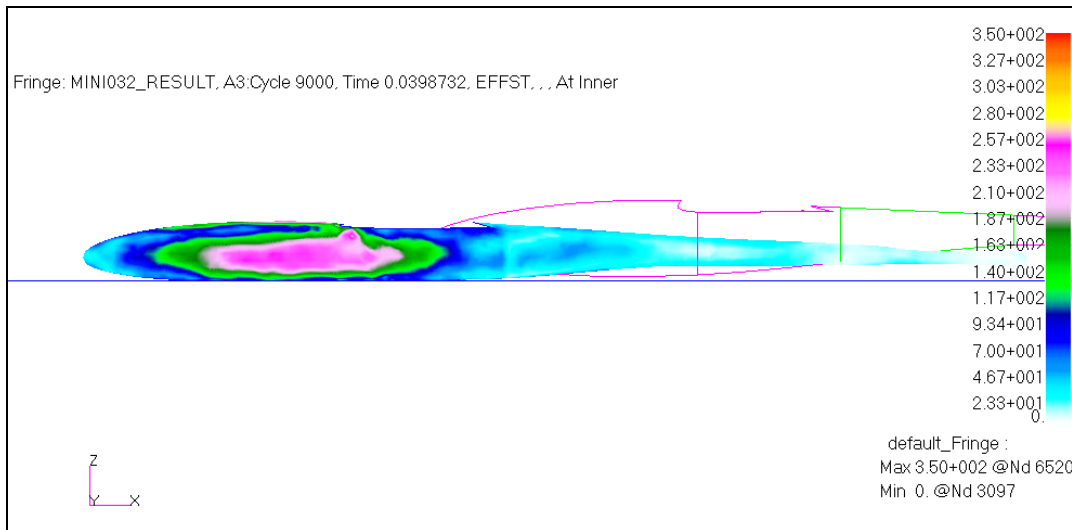


Figure 48: Stress contour of skin at t=0.039

5.5. Fuselage Shell with Internal Structure Landing Analysis On Rigid Surface

The analysis of fuselage shell indicated that it is possible to cover the convex surface of the “GÜVENTÜRK” Mini UAV by means of several layers of composite laminae. MSC.Dytran was capable of solving the impact problem after designating initial velocities, characterizing contact points of impact, modeling rigid or soil target surface.

In order to have more realistic results, internal structure must be added to the model. Bulkheads, vertical and horizontal stiffeners are modeled by measuring the dimensions of the internal structural elements of the real airplane. This way the effect of internal structure on the behavior of the airframe can be investigated.

Skin was already meshed; similar mesh with global edge length of 10 mm is applied to inner structure. Some portions did not allow applying QUAD Mesh; therefore, TRIA Mesh utilizing triangular elements is applied to those regions.

In order to make the whole fuselage unite, edges of internal structure and skin are associated. Association function of MSC.Patran allows different elements to move together; moreover, impact waves can jump through associated elements.

Material of inner structure is selected to be carbon/balsa composite. Carbon/balsa is composed of 5 mm of balsa wood in the middle layer and [0/90] carbon/epoxy plies in the top and bottom layers. Figure 49 shows the reinforcements added to the forward fuselage.

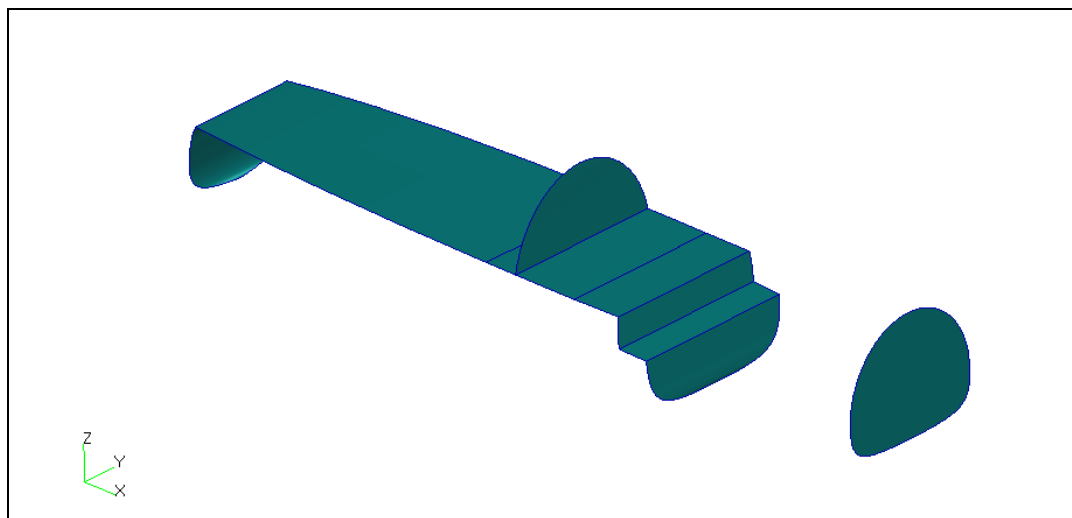


Figure 49: Internal reinforcement added to the fuselage

Figure (50) and (51) gives the forward fuselage with internal reinforcement showing the internal structure skin association.

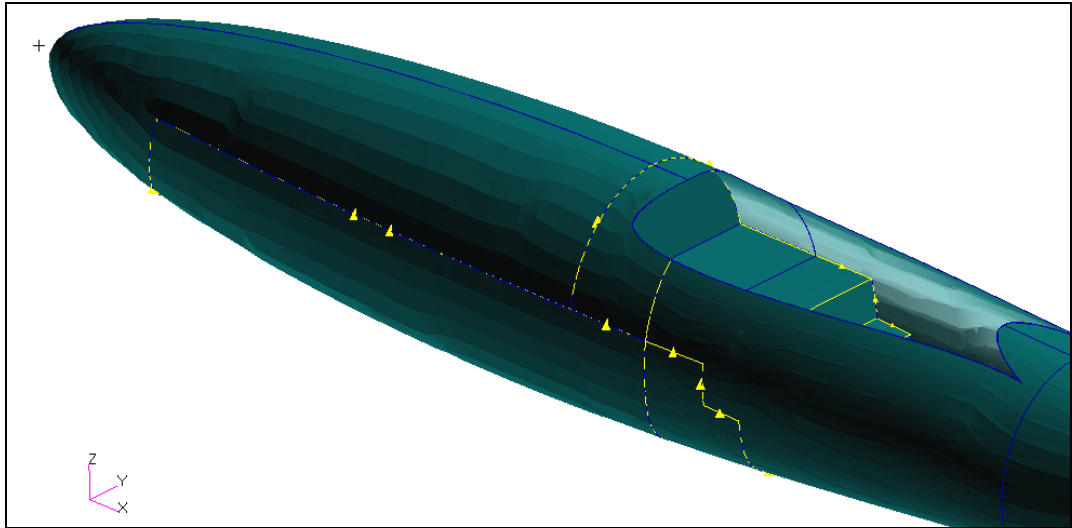


Figure 50: Internal Structure - Fuselage Skin Association

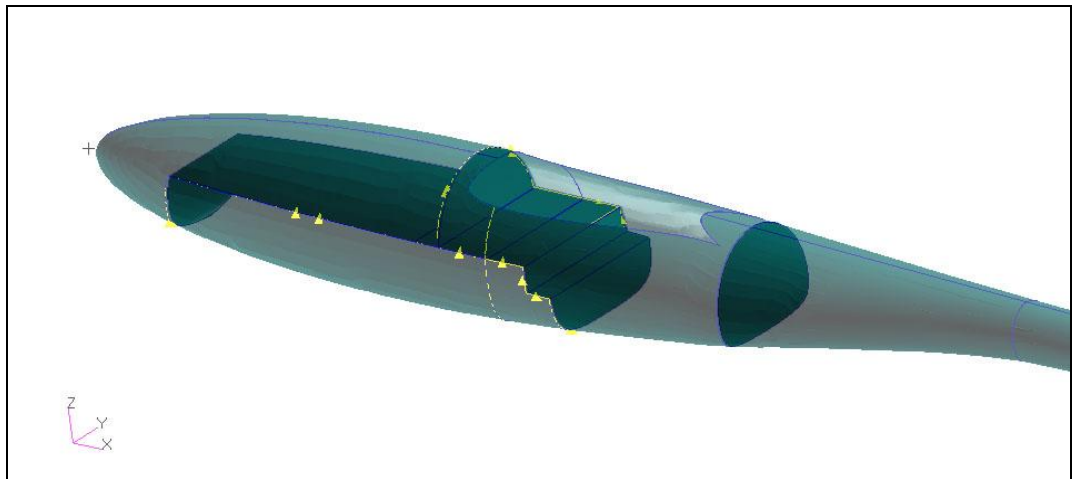


Figure 51: Internal structure in the low opacity fuselage skin

Table 18 gives a summary of the fuselage model with the internal structure added.

Table 18: Fuselage Model Properties (shell and internal structure)

Total Surface Area of Fuselage Model	313479 mm ²
Average Element Edge Length	10 mm
Total Number of Elements	3478

As the model and problem size becomes bigger, resultant file size of the explicit finite element solution increases. Since the earlier versions are incapable, to cope with the large output files Microsoft Office 2007 Excel is used to post-process the results. Microsoft Office 2007 Excel has no physical column limit; whereas, earlier

versions have a column limit of 256. All the fuselage elements are included in the result file; however, after verifying the results some of them are excluded. At some locations where the internal structure and skin meet, the impact force causes very high amount of stress at the perpendicular intersections. The reason of excessive stress at these perpendicular intersections is due to the fact that no fillets are modeled in the internal structure. In the actual airframe the perpendicular intersections of the skin-frame, skin-bulkhead are filleted. Figure 52 gives the sample preview of Excel file of effective stress distribution. The Excel file has 7085 columns and 402 rows. Maximum stress occurred in the analysis is found by the "MAK()" command of Excel which gives the maximum value of a selected area of cells. As it can be seen in Figure 52, maximum stress is exerted in inner layer of element 6891 at time $t=0.0261$ and at step 5900 for that particular case.

Note that "MAK()" command is valid for Excel 2007 Turkish Edition.

1	CYCLE	TIME	HKP	HKQ	HKR	HKS	HKT	HKU	HKV	HKW	HKX
112	5,50E+03	2,44E-02	3,10E+02	3,02E+02	3,17E+02	2,85E+02	2,23E+02	2,39E+02	2,40E+02	2,59E+02	2,40E+02
113	5,55E+03	2,46E-02	3,15E+02	3,06E+02	3,16E+02	2,92E+02	2,31E+02	2,43E+02	2,33E+02	2,60E+02	2,53E+02
114	5,60E+03	2,48E-02	3,07E+02	3,02E+02	3,16E+02	3,04E+02	2,35E+02	2,45E+02	2,37E+02	2,49E+02	2,58E+02
115	5,65E+03	2,50E-02	2,95E+02	2,95E+02	3,11E+02	3,13E+02	2,45E+02	2,45E+02	2,37E+02	2,45E+02	2,53E+02
116	5,70E+03	2,52E-02	2,88E+02	3,03E+02	3,15E+02	3,32E+02	2,55E+02	2,49E+02	2,46E+02	2,42E+02	2,60E+02
117	5,75E+03	2,55E-02	2,84E+02	3,10E+02	3,27E+02	3,54E+02	2,64E+02	2,61E+02	2,61E+02	2,35E+02	2,62E+02
118	5,80E+03	2,57E-02	2,89E+02	3,14E+02	3,33E+02	3,70E+02	2,68E+02	2,76E+02	2,67E+02	2,47E+02	2,54E+02
119	5,85E+03	2,59E-02	2,93E+02	3,27E+02	3,34E+02	3,73E+02	2,70E+02	2,79E+02	2,76E+02	2,66E+02	2,56E+02
120	5,90E+03	2,61E-02	2,95E+02	3,35E+02	3,39E+02	3,78E+02	2,70E+02	2,92E+02	2,78E+02	2,87E+02	2,58E+02
121	5,95E+03	2,64E-02	3,01E+02	3,39E+02	3,47E+02	3,64E+02	2,68E+02	2,98E+02	2,83E+02	3,08E+02	2,58E+02
122	6,00E+03	2,66E-02	3,06E+02	3,43E+02	3,45E+02	3,48E+02	2,70E+02	3,04E+02	2,88E+02	3,22E+02	2,74E+02
123	6,05E+03	2,68E-02	3,01E+02	3,39E+02	3,48E+02	3,40E+02	2,74E+02	3,10E+02	2,88E+02	3,15E+02	2,89E+02
124	6,10E+03	2,70E-02	3,06E+02	3,35E+02	3,45E+02	3,31E+02	2,71E+02	3,06E+02	2,89E+02	3,08E+02	3,00E+02
125	6,15E+03	2,72E-02	3,13E+02	3,25E+02	3,44E+02	3,37E+02	2,80E+02	3,07E+02	2,88E+02	2,96E+02	2,99E+02
126	6,20E+03	2,75E-02	3,19E+02	3,20E+02	3,46E+02	3,52E+02	2,82E+02	3,01E+02	2,75E+02	2,80E+02	2,91E+02

Figure 52: Sample Excel File of Effective Stress Distribution

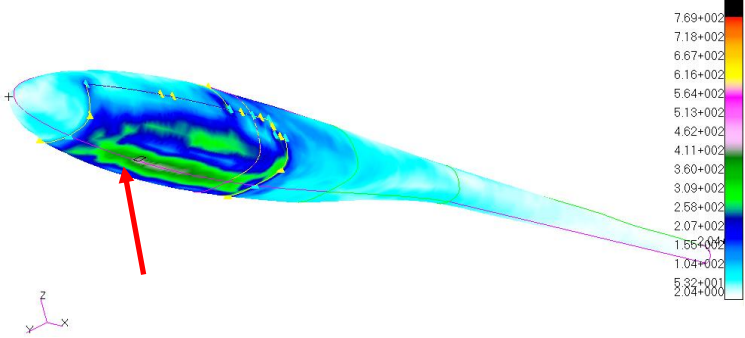
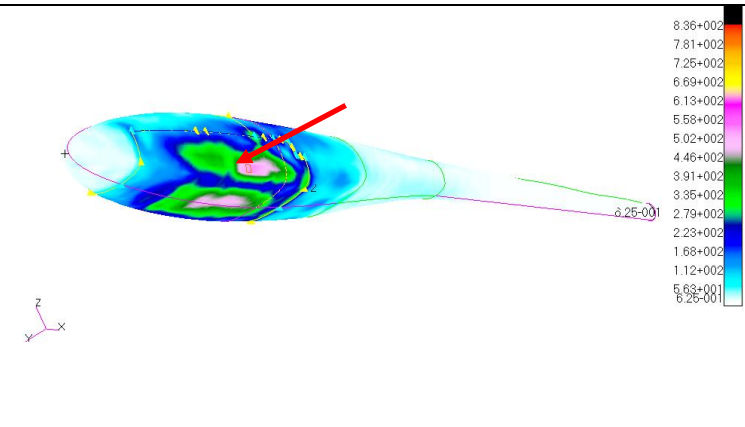
Impact analysis is completed for different stacking sequence of carbon/epoxy laminates. Maximum stress results corresponding to different stacking sequences are tabulated in Table (19):

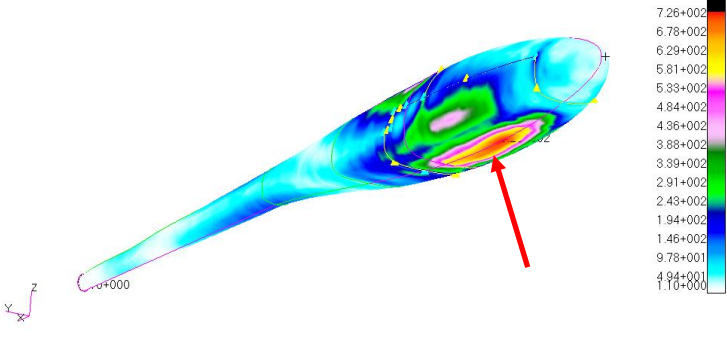
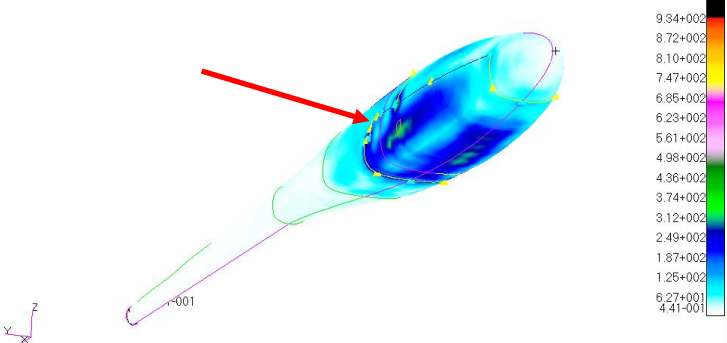
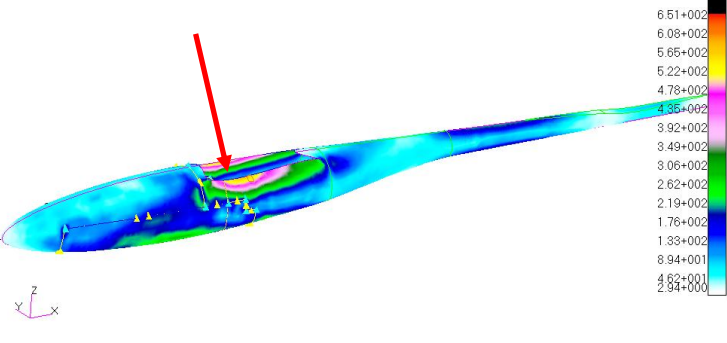
Table 19: Effective Maximum Stress for Various Stacking Sequence Sets

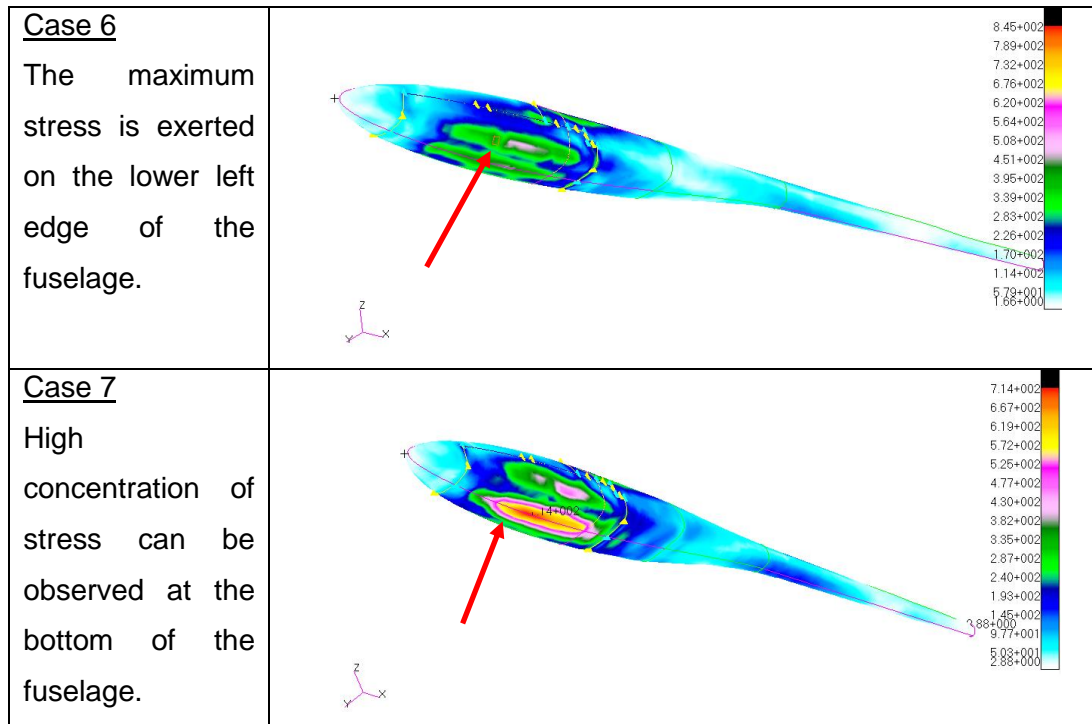
Case Number	Stacking Sequence (with respect to A/C's longitudinal axis)	Effective Maximum Stress (MPa)
1	[45/45/0/0/45/45] _s	451.05
2	[0] ₁₂	606.15
3	[0/45] ₆	764.75
4	[45] ₁₂	378.02
5	[45/45/45/45/0/0] _s	587.20
6	[45/45/0/0] ₃	582.96
7	[0/0/45/45] ₃	749.30

For the 7 cases tabulated above, the point at which the maximum stress occurs is different. Table 20 shows the corresponding maximum stress point and the stress contour at the time the maximum stress is observed.

Table 20: Location of the points of maximum stress for each case
(continuing on the next 2 pages)

<p><u>Case 1</u></p> <p>Maximum stress is exerted at the bottom of the fuselage.</p>	 <p>The image shows a stress contour plot of a fuselage. A red arrow points to the bottom of the fuselage, indicating the location of maximum stress. A color scale on the right ranges from 2.04e+000 (blue) to 7.69e+002 (red).</p>
<p><u>Case 2</u></p> <p>Maximum stress is seen on the left hand side of the fuselage. However, stress level at the bottom is also high.</p>	 <p>The image shows a stress contour plot of a fuselage. A red arrow points to the left side of the fuselage, indicating the location of maximum stress. A color scale on the right ranges from 6.26e-001 (blue) to 8.36e+002 (red).</p>

<p>Case 3</p> <p>Maximum stress is observed at the bottom. Compared with the first case one should notice that the stress concentration is very high</p>	 <p>The image shows a stress distribution plot for Case 3. The fuselage is oriented horizontally. A red arrow points to a region of high stress concentration (red/yellow) at the bottom of the fuselage. A color scale on the right ranges from 1.10+000 (blue) to 7.26+002 (red). A coordinate system (x, y, z) is shown at the bottom left.</p>
<p>Case 4</p> <p>Smooth stress distribution peaks slightly on the right hand side of the fuselage. Both minimum stress and best stress distribution is observed in this case.</p>	 <p>The image shows a stress distribution plot for Case 4. The fuselage is oriented horizontally. A red arrow points to a region of high stress concentration (red/yellow) on the right side of the fuselage. A color scale on the right ranges from 4.41+001 (blue) to 9.34+002 (red). A coordinate system (x, y, z) is shown at the bottom left.</p>
<p>Case 5</p> <p>Upper left hand side of the fuselage is stricken by the stress. The cavity on the top of the fuselage yields stress concentration at that region</p>	 <p>The image shows a stress distribution plot for Case 5. The fuselage is oriented horizontally. A red arrow points to a region of high stress concentration (red/yellow) at the upper left side of the fuselage. A color scale on the right ranges from 2.84+000 (blue) to 6.51+002 (red). A coordinate system (x, y, z) is shown at the bottom left.</p>



Different stacking sequences resulted in different maximum stresses. As it can be seen, the layup case with $[45]_{12}$ seems to be the most optimized solution among the 12 ply laminates. Examining Table 20 one can say that stress is very smoothly distributed in Case 4. For this case, the maximum stress 378.02 MPa is exerted on the inner layer of Element 6891. Effective stress vs. time diagram for the Element 6891 is given in Figure 53. A generic screenshot of the analysis of skin with internal structure is given in Figure 54.

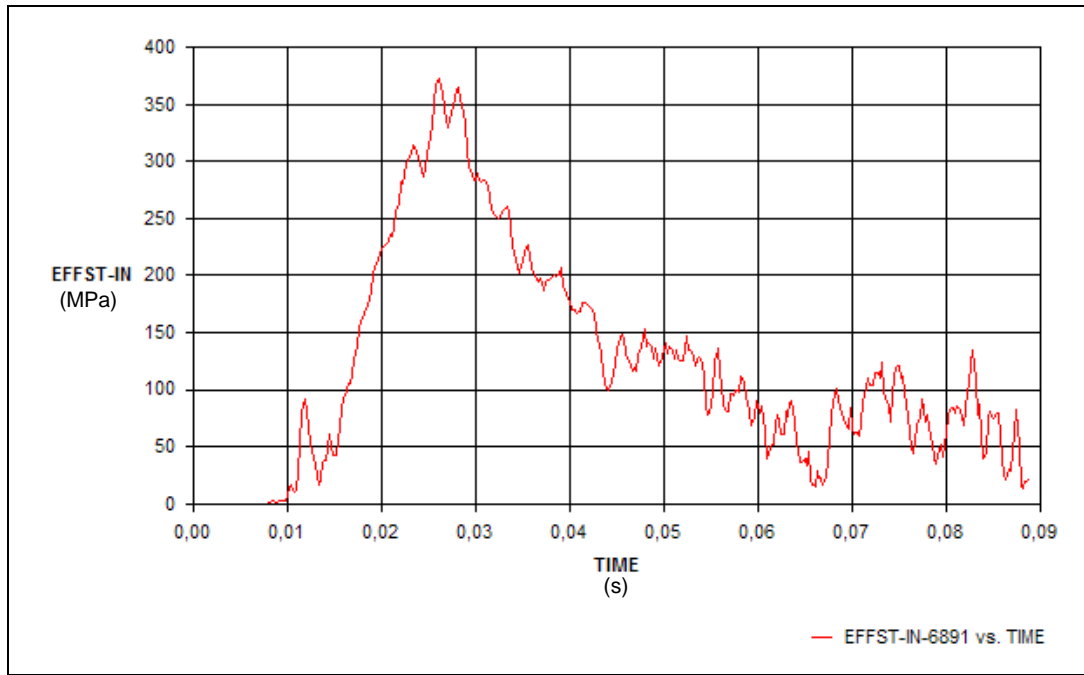


Figure 53: Stress (MPa) vs. time graph for best layup case ([45]₁₂)

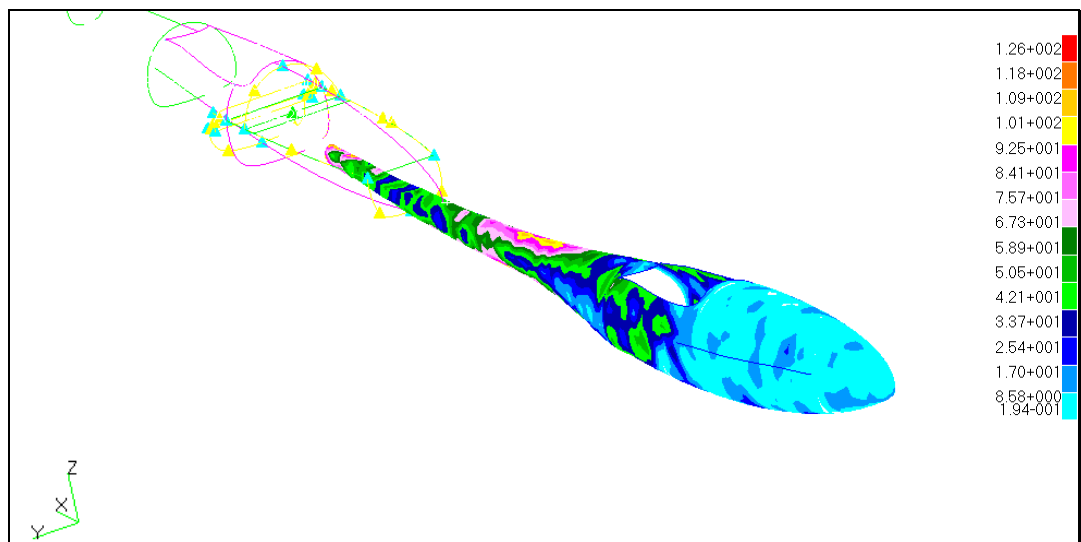
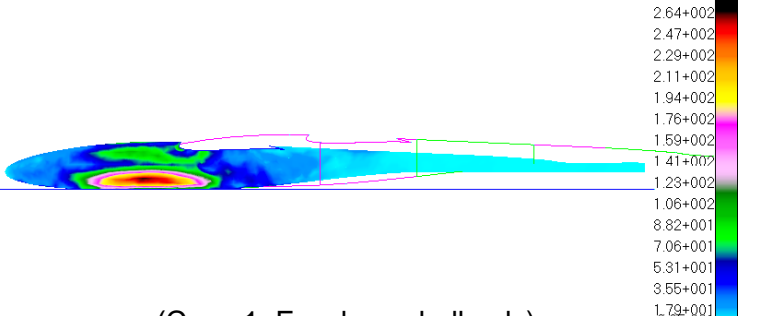
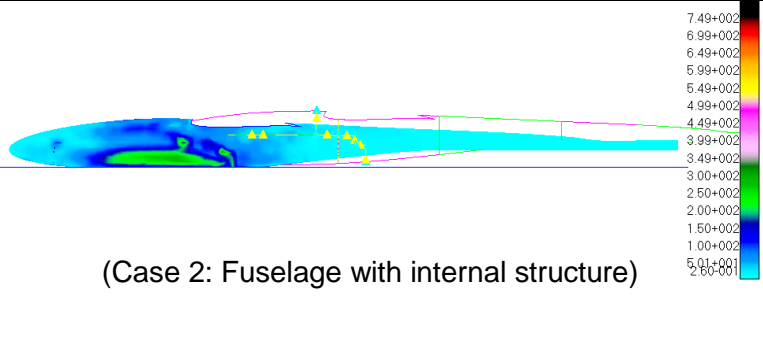
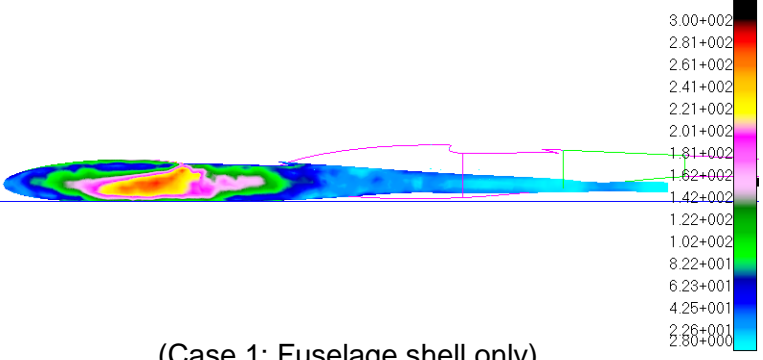
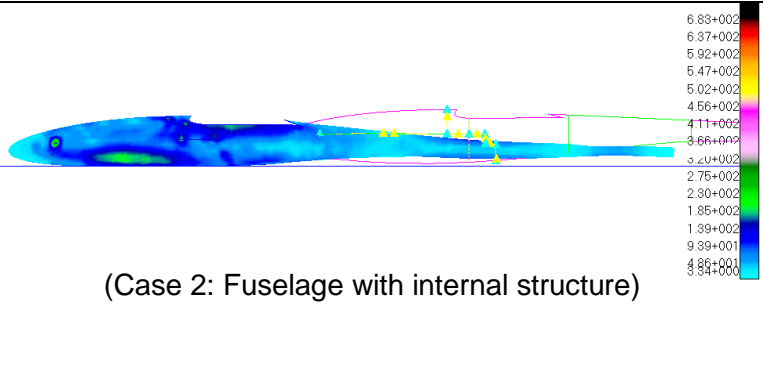
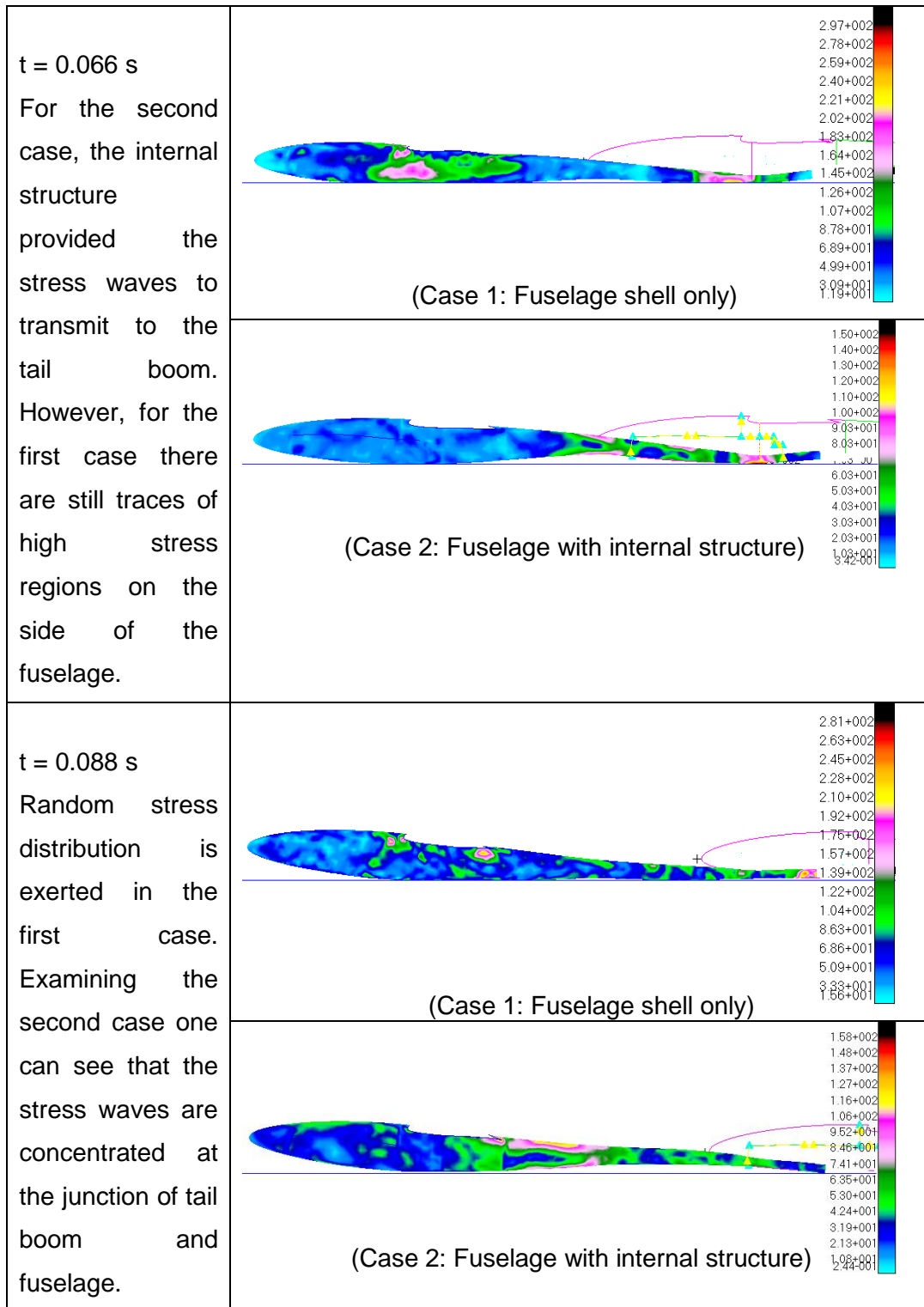


Figure 54: Analyzed Fuselage and Internal Structure Model

Table 21 gives the comparison of previous two cases: Fuselage shell and fuselage with internal structure analyses. Examining the table one can see the effect of bulkheads and the other structural elements. For each time segment, upper picture shows the case with fuselage shell only.

Table 21: Comparison of fuselage shell and fuselage with internal structure analysis (continuing on the next 2 pages)

<p>t = 0.22 s</p> <p>After the fuselage touches the ground stress is immediately exerted on the bottom section. Absence of internal structural elements leads to a stress concentration on the skin.</p>	 <p>(Case 1: Fuselage shell only)</p>
<p>t = 0.044 s</p> <p>In the first case, the stress at bottom of the fuselage moves towards the side of the fuselage and the deformation on fuselage shell can be easily seen; whereas, the second case keeps its integrity.</p>	 <p>(Case 2: Fuselage with internal structure)</p>
<p>t = 0.044 s</p> <p>In the first case, the stress at bottom of the fuselage moves towards the side of the fuselage and the deformation on fuselage shell can be easily seen; whereas, the second case keeps its integrity.</p>	 <p>(Case 1: Fuselage shell only)</p>
<p>t = 0.044 s</p> <p>In the first case, the stress at bottom of the fuselage moves towards the side of the fuselage and the deformation on fuselage shell can be easily seen; whereas, the second case keeps its integrity.</p>	 <p>(Case 2: Fuselage with internal structure)</p>



At this point it would be meaningful to compare the results of MSC.Dytran with the real life situation. In one of the test flights “Güventürk” has crash-landed and severe

damage occurred on the fuselage and on the tail boom. The picture of the crushed aircraft is given in Figure 55.



Figure 55: Crush damage on the tail of the UAV

Figure 56 shows the propagation of stress waves through the body between $t = 0.033$ s and $t = 0.055$ s in the middle layers of composite laminate. If the stress wave travelling on the tail boom is carefully observed it can be seen that since the cross section of the tail boom gets smaller, it grows up as it goes towards the end section.

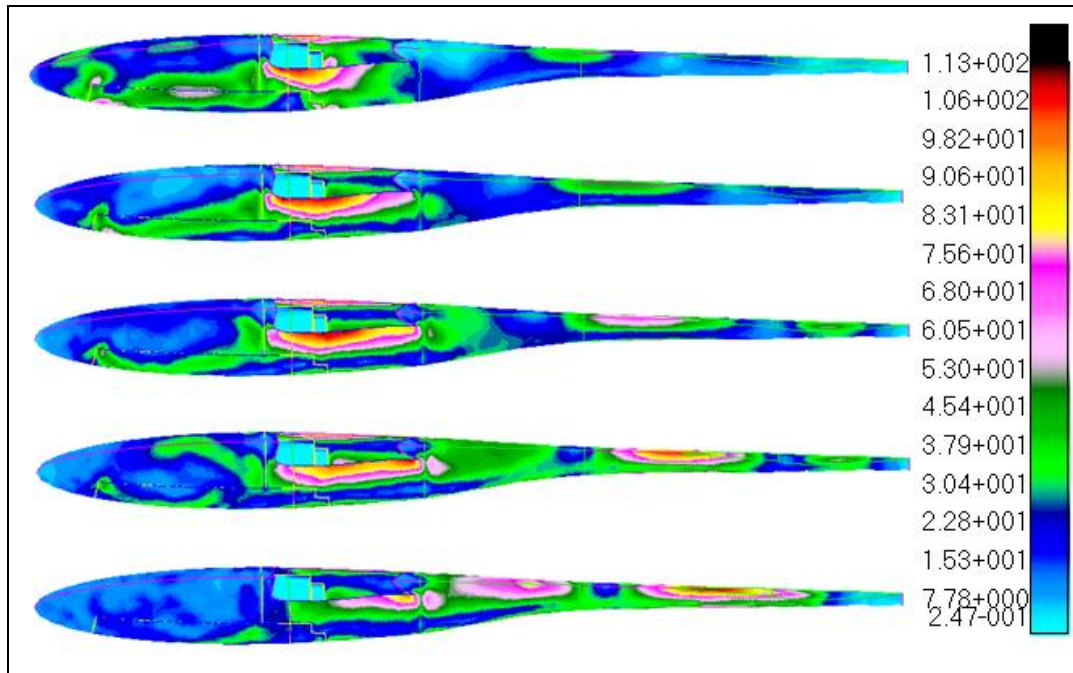


Figure 56: Stress (MPa) contour of the fuselage between $t = 0.033$ and $t = 0.055$

Comparing Figure 58 and 59 the designer may have a clue about the reason of the severe damage on the tail of the aircraft. There is a high possibility that the damage on the tail of “Güventürk” is occurred because of a stress wave similar to the one shown in Figure 56. A stress wave that increases in magnitude as it moves towards the end of the fuselage may caused an excessive stress concentration which is larger than the composite part of the body can tolerate. As a result, tail boom is broken at the point shown in Figure 55.

5.6. Fuselage Shell and Internal Structure Landing Analysis On Soil

Having analyzed different cases impacting to the rigid surface there are a number of results for the fuselage of “Güventürk” Mini UAV. In this part, in order to see the impact behavior on a more elastic surface soil model is used as the target. The fuselage with $[45]_{12}$ layup design is analyzed and stress vs. time graph is plotted in Figure 57.

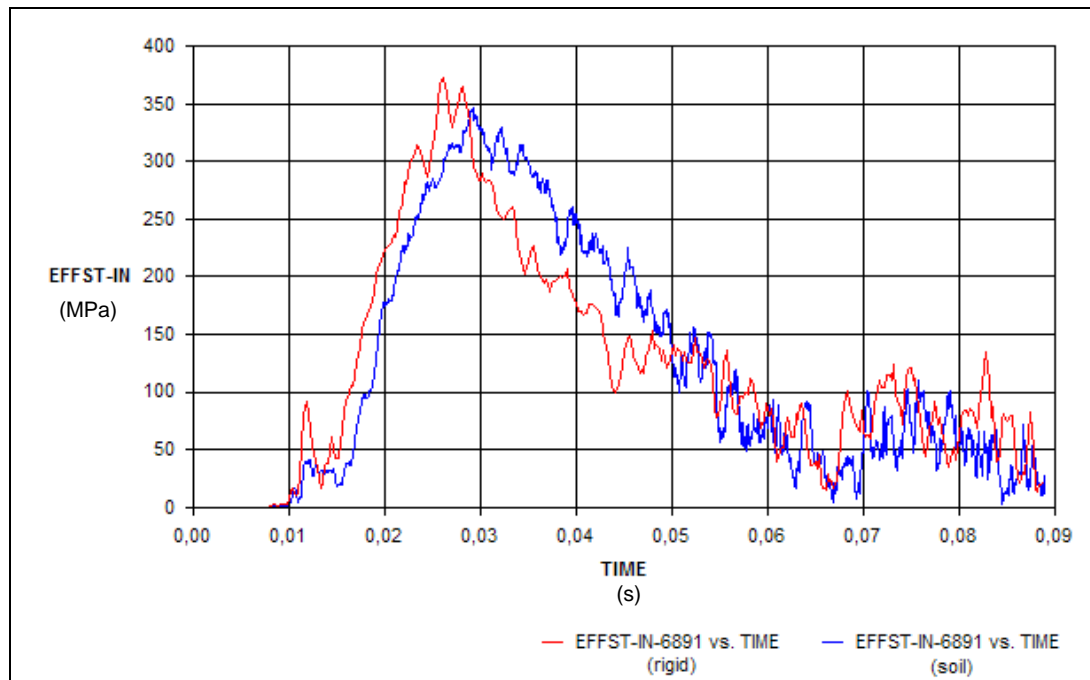


Figure 57: Stress (MPa) vs. time graph for $[45]_{12}$ (rigid surface and soil model)

The effect of soil model on the impact case is as expected. A softer and more elastic surface dissipates some energy.

For the rigid target case, the maximum stress that is exerted on the Element 6891 is 378 MPa; however, for the soil target case it is less than 350 MPa. However, it should be noted that there is no major difference between the results determined a rigid target and soil target case. By decreasing the modulus of elasticity of the target the effect of flexibility of the target material on the results can be investigated as a future work.

5.7. Fuselage Shell and Internal Structure with Shell Wing Landing Analysis On Rigid Surface

A complete study of fuselage with different stacking sequences is completed so far. In this part, additional study is completed by adding the effect of wing that is attached above the fuselage. The main aim of this section is to see the effect of belly landing on the behavior of the wing. In this part the wing is modeled as a shell without any internal structure such as spars, ribs etc.

At the beginning of this chapter, model of Mini UAV was imported to MSC.Patran. Then, the wing and tail was cut out and analyses were conducted. In this part, wing

is again imported and attached to the fuselage. After that, the wing is meshed with an average element edge length of 10 mm. $[0^\circ, 90^\circ]_6$ composite layup is used in the wing skin. In Part 5.5 $[45^\circ]_{12}$ layup was the one that gave the minimum stress result for the fuselage; therefore, in this section the same layup is used in the fuselage frame. A generic screenshot of fuselage with internal structure and wing during analysis is given in Figure 58.

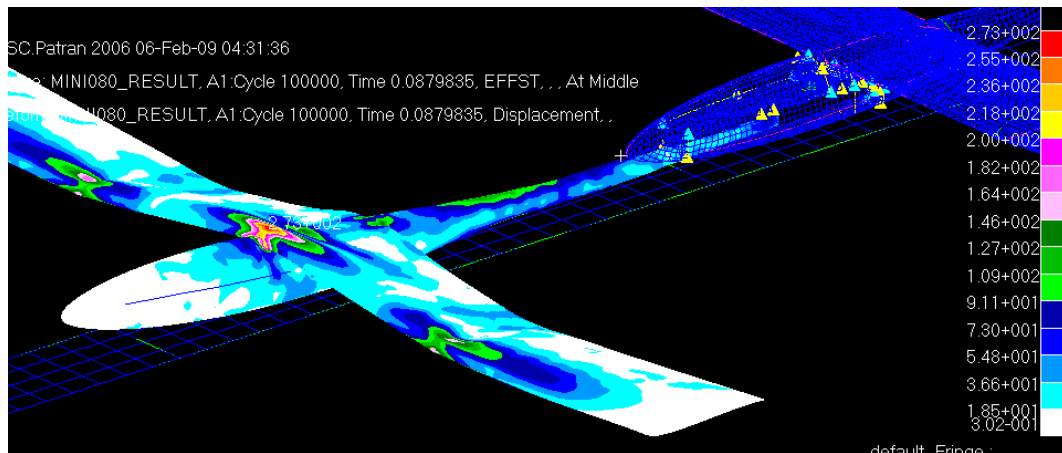


Figure 58: Analyzed Fuselage with Internal Structure and Shell Wing Model

It is possible to observe the vertical position of the wingtip from Figure 59. The nose of the fuselage is the origin of the global coordinate axis. The vertical position (z-coordinate) of the wing tip is 77 mm. The z-coordinate of the surface is -50 mm. this brings out the fact that the wing tip is 127 mm above the ground. Figure 59 shows the vertical travel of a node on the wingtip. Since there is no spar inside the wing model the deflection is about 65 mm after 0.08 s.

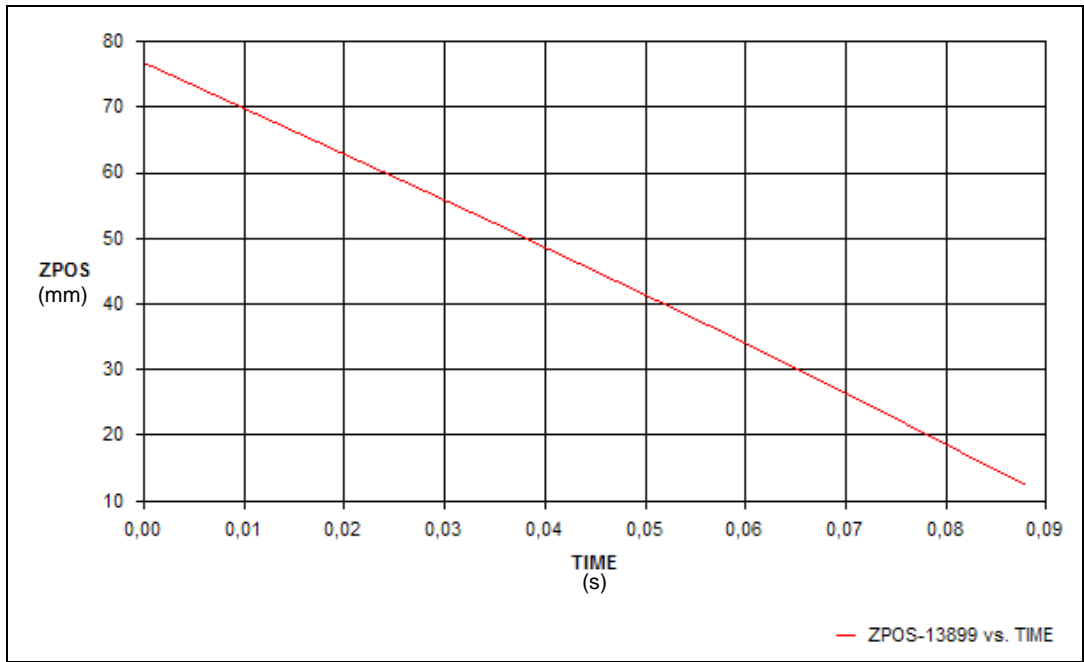


Figure 59: Wing tip deflection (mm) vs. time (s) (for no spar case)

After the impact, since it is attached to the fuselage, the wing gains a rotational inertia and starts rotating around its own center of gravity. The tangential velocity of wingtip is added to its initial velocity. As a result of this, velocity of wing tip increases. Vertical velocity of the wingtip is given in Figure 60.

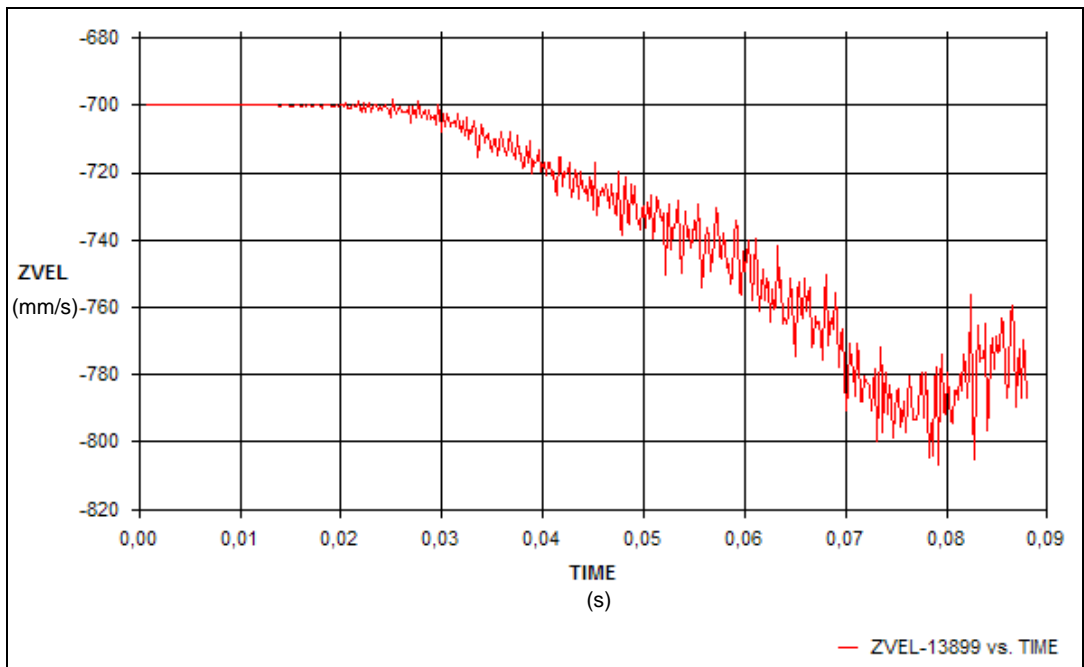


Figure 60 Vertical velocity of the wingtip

5.8. Fuselage Shell and Inner Structure with Shell Wing Landing Analysis (On Soil)

The previous case is re-analyzed by replacing the target surface with soil model. Stress vs. time graph is plotted. As it was expected, elasticity of soil dissipated the impact energy and the maximum stress exerted on the element 6226 is decreased by an amount of 20%. Figure 61 shows the stress vs. time graph for landing analysis on rigid and soil surfaces.

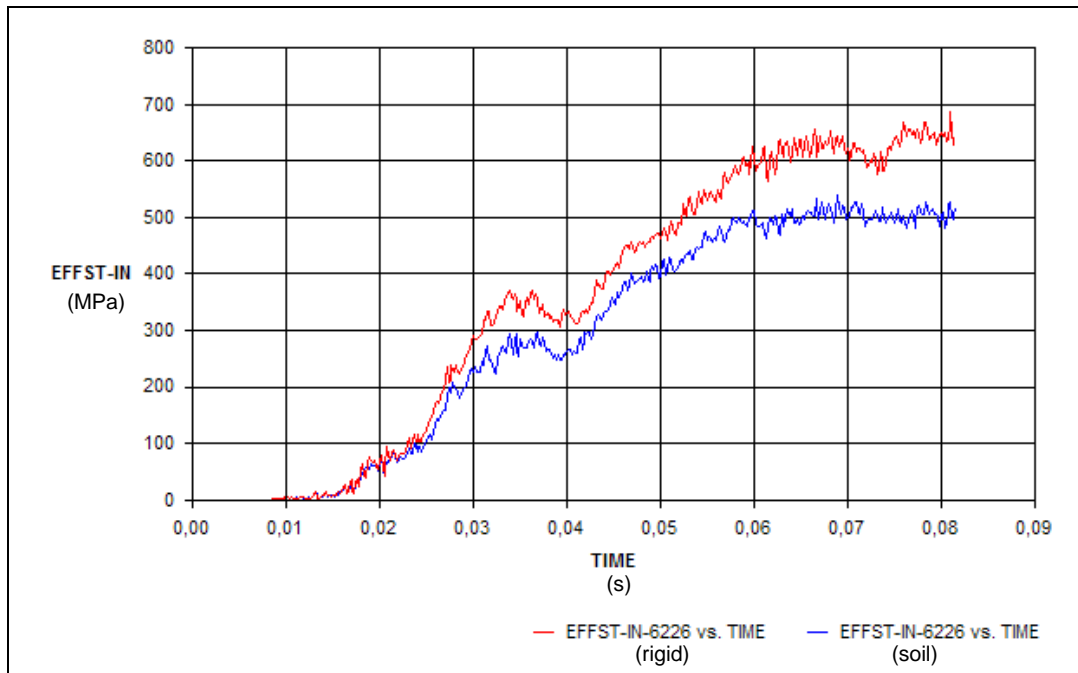


Figure 61: Stress (MPa) vs. time graph for $[45]_{12}$ (rigid surface and soil model)

The wingtip deflection vs. time graph is given in Figure 62. This graphic basically plots the z coordinate of the node at the wing tip with respect to time. Therefore, one can observe how much deflection is exerted on the wingtip with respect to time. As it can be seen, there is no significant difference between two belly landing cases. Wing tip deflection is slightly less when considering belly landing on soil surface.

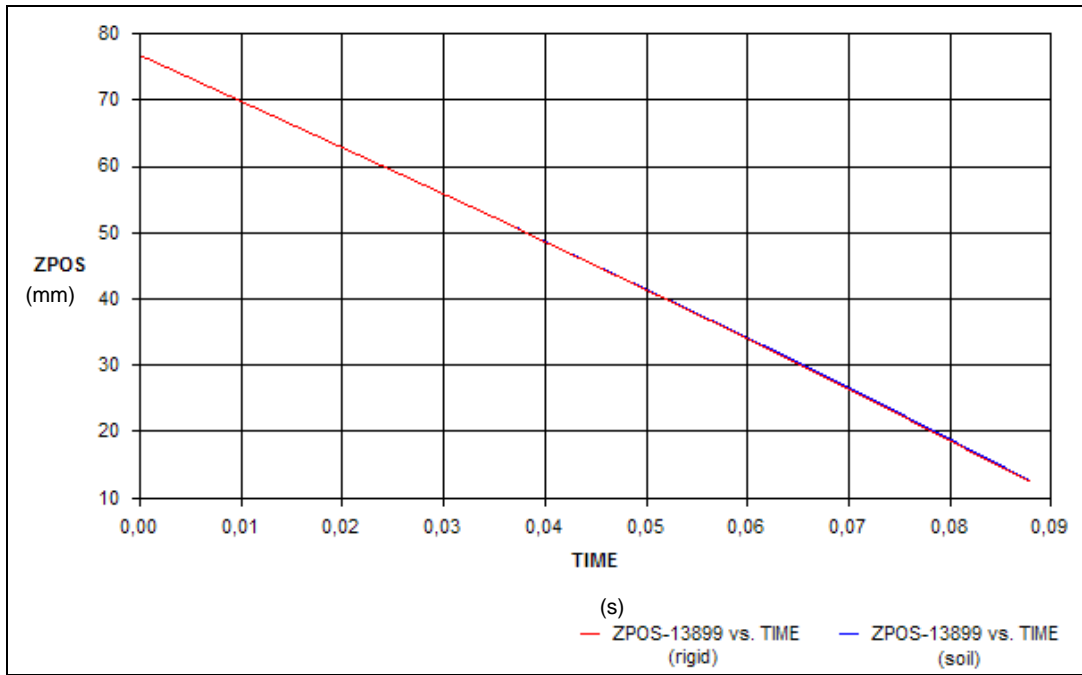


Figure 62: Wingtip deflection vs. time (rigid and soil surfaces)

One should note that the deflection of the wingtip plot is affected by the deformation of the fuselage. If the fuselage was completely rigid, the wingtip deflection curve would give the deflection of tip only. In this case however, the deformation of the fuselage causes wing root to move down as well. That brings out the fact that whole wing translates down, additionally it deforms. This can be observed in Figure 63-64.

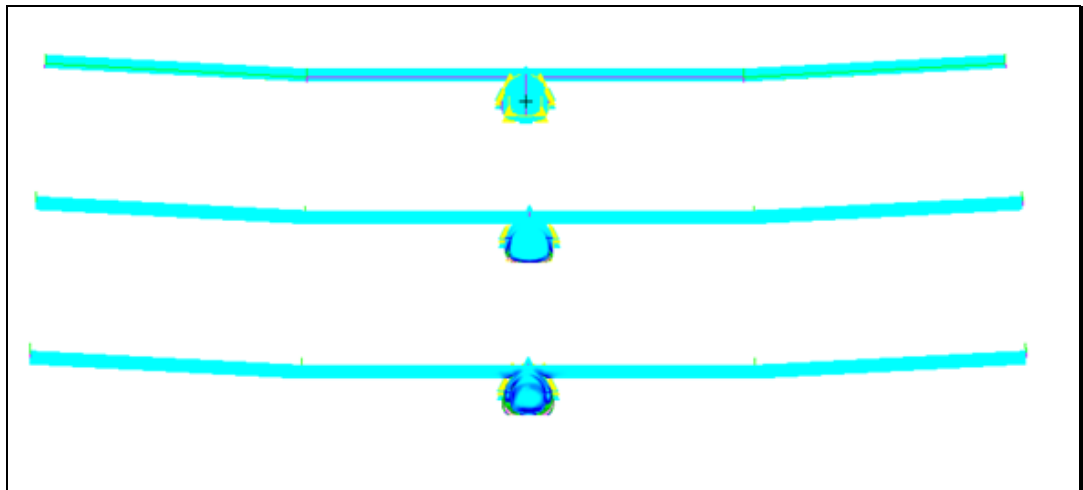


Figure 63: Stress contour graphs for $t=0$, $t=0.021$, $t=0.032$ (s)
(continuing on the next page)

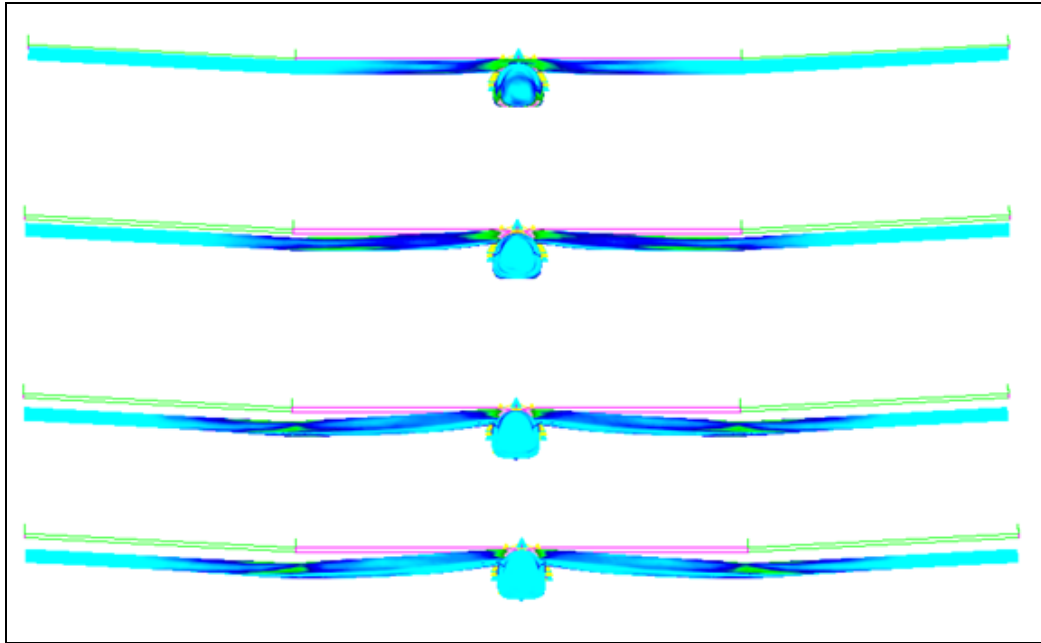


Figure 64: Stress contour graphs for $t=0.041$, $t=0.052$, $t=0.062$, $t=0.075$ (s)

Considering Figure 63 it is seen that the stress waves jump to middle wing at $t=0.032$ s. Figure 64 shows the deformation of the wing as the stress waves propagates towards the tips of the wing.

5.9. Fuselage Shell and Internal Structure with Shell Wing and Internal Structure Landing Analysis On Rigid Surface

Final analysis of this chapter includes the fuselage, wing, spar and ribs. The shell of wing is modified by a front spar which stiffens the whole wing from root to tip. Another spar located towards the trailing edge of the wing provides additional rigidity. Two ribs are also integrated at tip of the wing and at the point where dihedral of wing is applied. Front spar is built of 10 mm thick balsa, covered by two carbon layers. Rear spar is built fully of carbon to improve the structural rigidity. Internal structure of wing is shown in Figure 65.

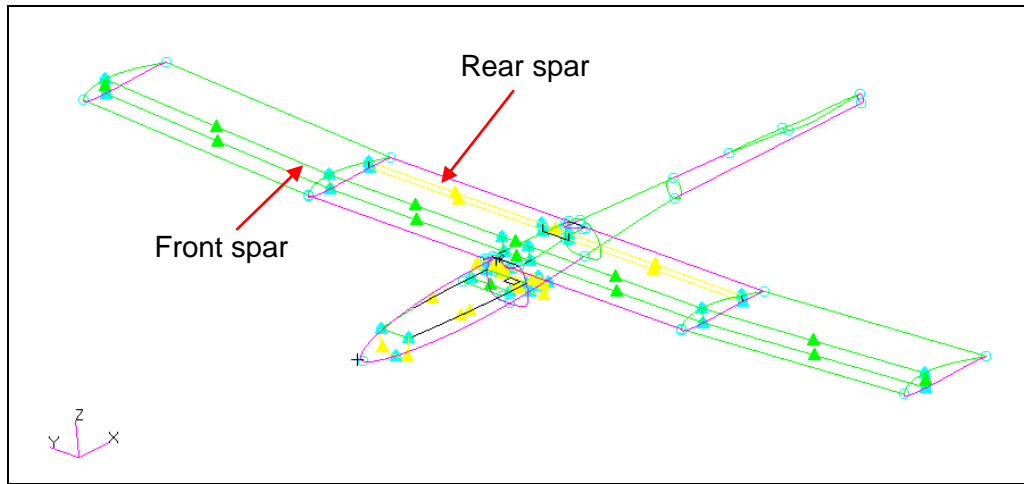


Figure 65: Internal structure of wing

This complete model of aircraft is subjected to belly landing analysis and wingtip deflection and maximum stress graphs are plotted.

Figure 66 shows the vertical position of two nodes with respect to time. Node 15078 (red) is located on the root of the wing whereas Node 15588 (blue) is located on the tip. It is possible to examine the deflection of the wing tip with respect to wing root. When the wing is stiffened by spar the deflection becomes nearly 20 mm in 0.07 s.

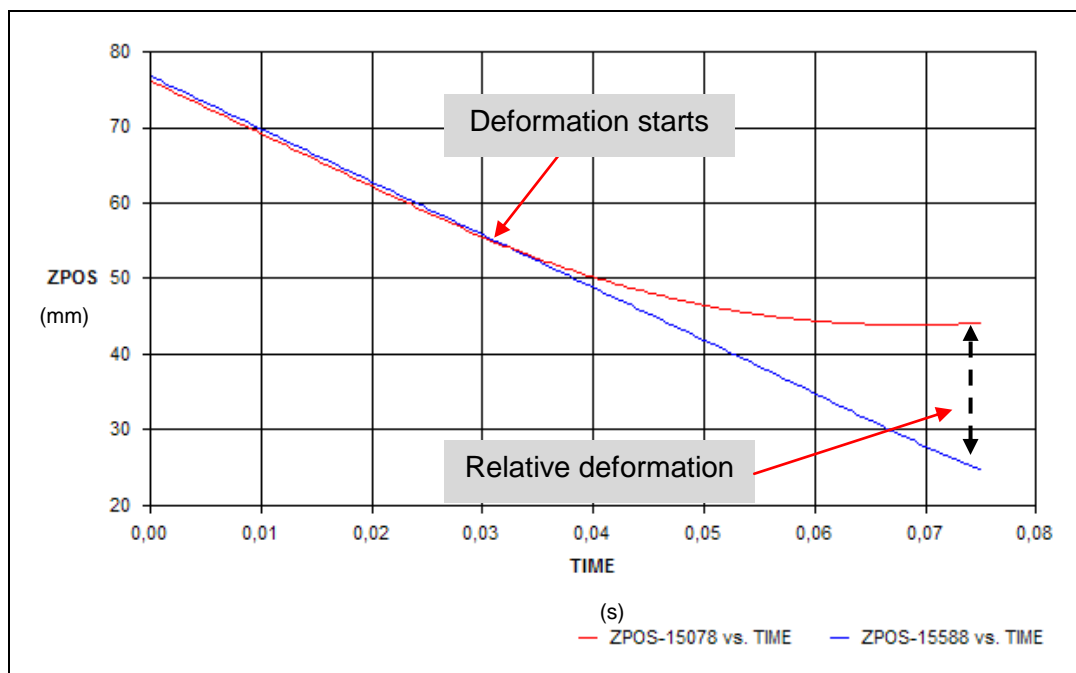


Figure 66: Wingtip deflection vs. time (rigid surface)

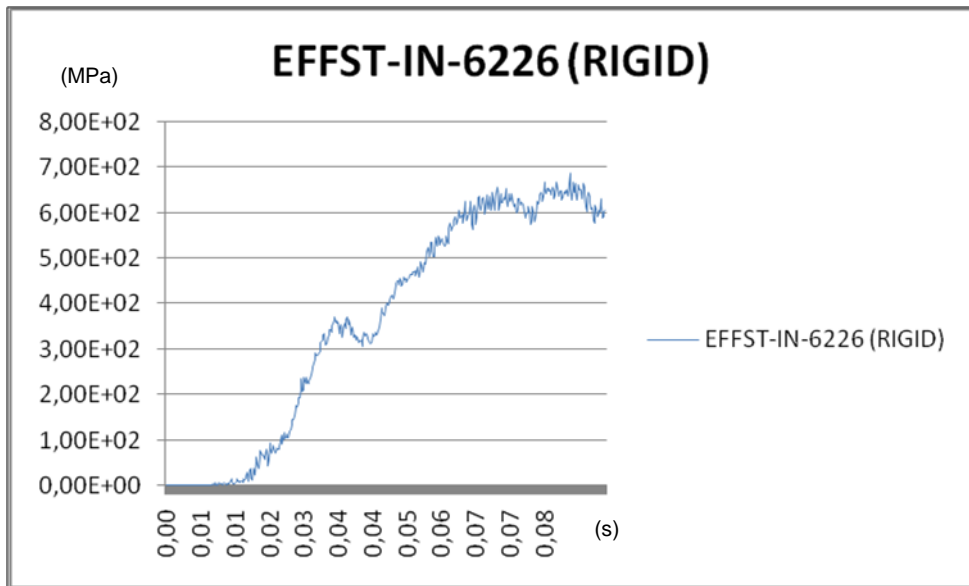


Figure 67 Stress (MPa) vs. time graph for $[45]_{12}$ (rigid surface)

Figure 67 shows the maximum stress (MPa) vs. time (s) graph. Maximum stress is exerted on the inner layer of Element 6226. Stress contours at different instants are given in Figure 68.

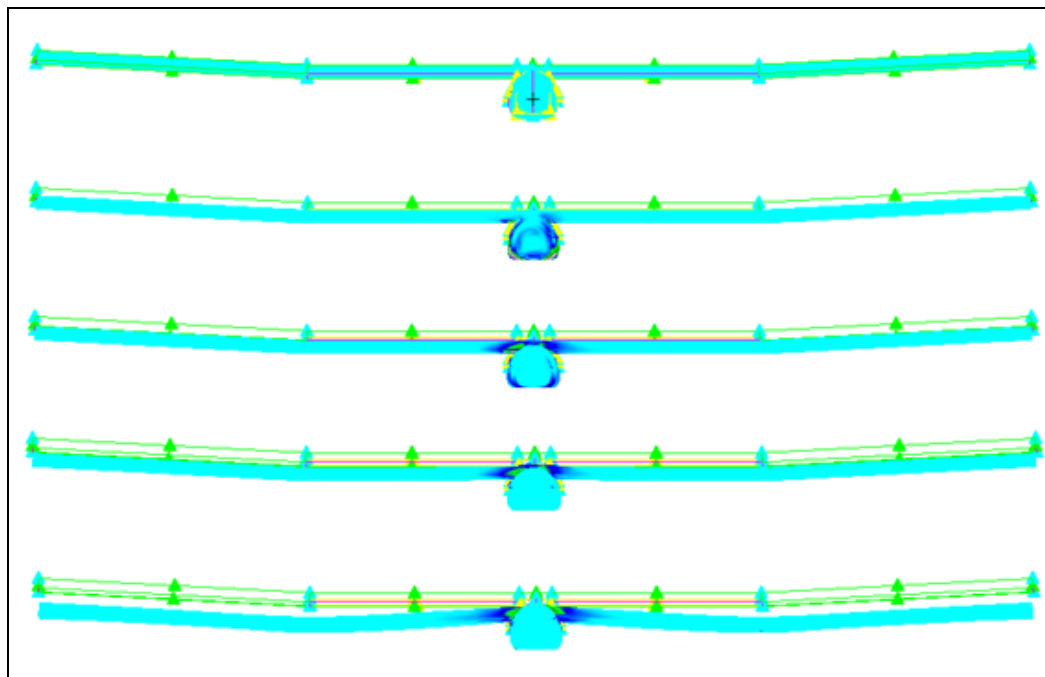


Figure 68: Stress contours at $t=0$, $t=0.022$, $t=0.045$, $t=0.056$, $t=0.075$ (s)

Figure 68 shows that for the fuselage with internal structure and wing with internal structure the stress waves are concentrated at the wing-fuselage junction of the air vehicle. That brings out the need that the designer should give necessary attention to that region.

As the wing-fuselage assembly impacts to the rigid surface the stress waves start forming at the bottom of the fuselage. The waves then move towards the top of the fuselage and pass to the wing. The Figure 69 shows the place at which maximum stress is observed.

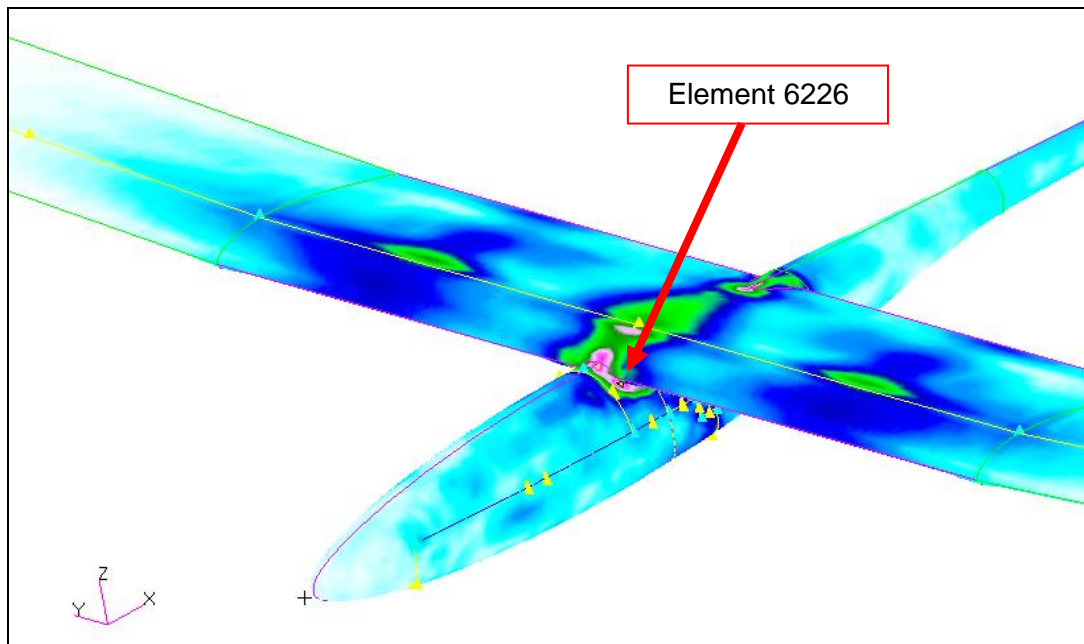


Figure 69: Location of maximum stress

As it can be seen the region of maximum stress is at a close proximity to the wing-fuselage junction. It should be noted that in the current model the wing-fuselage junction is composed of limited number of nodes. The connection of the fuselage to the wing is made through the boundary nodes along the edge of the cut-out fuselage as shown in Figure 70. Figure 70 shows the nodes through which fuselage and wing are attached together. As it can be seen, wing-fuselage association is made along a curve only, and stress transfer occurs through the nodes on this curve. However, in the actual manufactured airplane the cut-out in the fuselage is only partial and wing does not only sit on the boundary edges of the cut-out fuselage. Wing is placed on a flange which extends towards the interior from the boundary edges. Therefore, the

stress transfer from the impacted fuselage to the wing takes place over a wider area which will definitely reduce the stress concentration. It should be stressed that as the stress is passing from fuselage to wing, lack of a wider physical load transfer surface causes stress concentration at the fuselage cut-out edge and wing intersection region

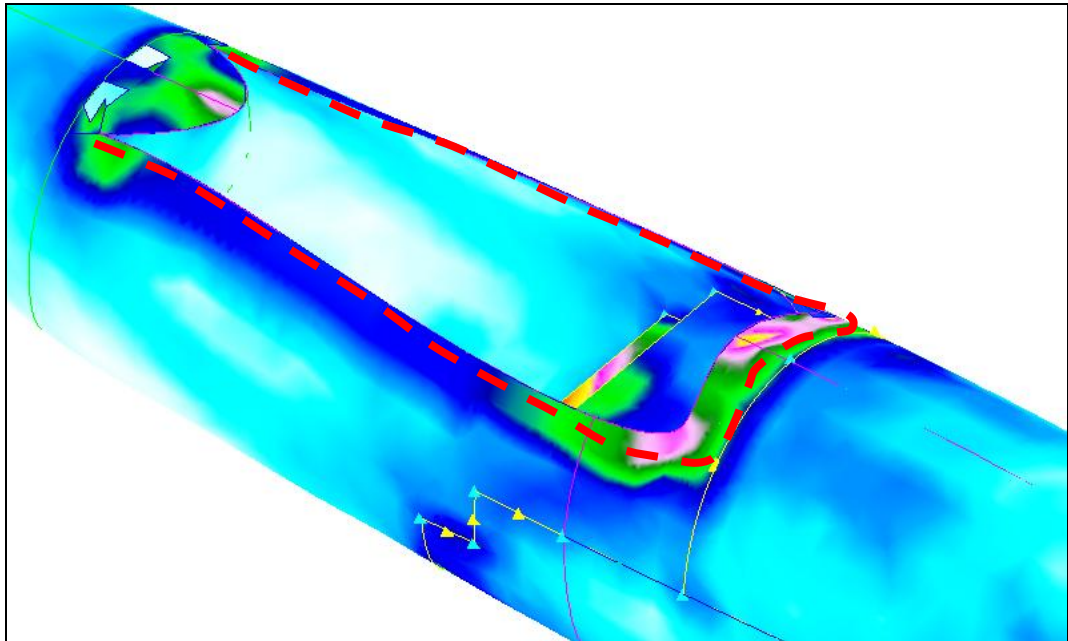


Figure 70: Wing-fuselage junction nodes (dashed line)

The effective stress vs. time graph shown in Figure 67 indicates that the stress rises up to 700MPa at Element 6226. The stress in this element may be reduced to lower levels if the wing-fuselage junction model is improved and the flange surface, which provides a wider load path, is included in the cut-out region.

CHAPTER 6

CONCLUSION

6.1. REVIEW OF RESULTS

The increasing value of human being's life brings out the demand on unmanned systems. For risky environmental conditions in aviation unmanned aerial platforms are employed. Among the all unmanned platforms, mini UAV's became popular because of low budget requirements in manufacturing, ease in operation and flexibility in maintenance. Hand launching/belly landing and application of composite technology are common features of UAV's in this category.

In this study, belly landing analysis of a mini UAV is conducted. The key question to be answered was how the design of composite parts affects the stress capability of whole airframe. To have a consistent answer to this question a number of analyses have to be done.

When the impact velocity is considered, the belly landing case can be treated to be low velocity impact. Observing a belly landing case one can see that short durational impulsive forces are exerted on the fuselage of the airframe. Contact area also changes in time as deformation and bouncing occurs. These characters of the problem address explicit finite element solution techniques; therefore, a commercial finite element solver, MSC.Dytran, is used.

Although impact is a short durational nonlinear phenomenon, an alternate simplified analytical method which assumes low velocity impacts as quasi-static is also experienced. The method is known as "Hertz Contact Law" and calculates the force distribution and its time dependency caused by a low velocity impact. After modeling a case with ball impactor and steel plate target, the problem is solved by both applying Hertz Contact Law approach and explicit finite element solution technique. The results of different approaches are given in Figure 21-23, 26.

Examining the figures it can be said that, since the magnitude of error in deflection is small, analytical method can be employed for low velocities. However, for higher velocities, the difference between results of analytical and explicit finite element method becomes larger. Mass of the impactor is also an important parameter that the deflection increases linearly with the mass of the impactor. This brings out the fact that, one should be suspicious about the reliability of the results of “Hertz Contact Law”, especially if the kinetic energy of impactor is high.

After comprehending that analytical method can only be applied for a certain region of impact problems, solutions conducted with MSC.Dytran are focused on.

As an initial series of analyses, since a large and complex structure requests more computational power, simple geometry of a flat plate is examined. Application of “Laminate Modeler Tool” is first introduced in these preliminary analyses. By building different laminates with combination of 8 carbon layers target plate is formed. An impulsive load of 100kN is then applied to the geometric center of the composite plate for 0.5 s. For each combination of laminae stacking sequence the maximum stress and maximum deflection of plate is tabulated. (Table 12)

The simple study mentioned above relieved the fact that stacking sequence of a layup directly affects the response of the composite laminate. Both maximum stress exerted on the plate and maximum deflection of the plate is absolutely related to stacking sequence. In the light of this information, further analyses are conducted.

“Güventürk” Mini UAV, designed and built in METU Aerospace Department UAV Research Center, is a small sized, hand launching, belly landing unmanned aerial vehicle. In order the design of the “Güventürk” to optimize and in order the belly landing performance to maximize; belly landing analysis of “Güventürk” by MSC.Dytran is completed. The main purpose of this study is to guide the designer to decide the design of the mini UAV’s composite parts by observing the nature of low velocity impact. In this way, a set of choices of stacking sequence for carbon/epoxy laminate is given.

Modeling and pre/post processing is completed in MSC.Patran. Mainly two types of output files are requested from MSC.Dytran. Files with “arc” extension are archive files and includes the result information at each time step and can be processed by MSC.Patran. Model information is also embedded in archive file. Files with “ths” extension are the time history files. Time history files can contain particular result information about any grid and/or element. Since the element and grid number in the

model of "Güventürk" is high, the output files are large in row and column number. Large time history files are exported into "txt" format and imported into Microsoft Excel 2007. This very current version of Microsoft Excel is capable of handling large files. Determination of maximum stress is conducted in Microsoft Excel 2007.

A progressive analysis approach is followed for "Güventürk". First, the skin of the fuselage is meshed and projected to a rigid surface at a vertical velocity found from the stall velocity of the aircraft and the glide angle. The deformation on the body is observed and since no internal structure like bulkhead was modeled, the deformation is found to be very large. Yet, the movement of stress waves gives the idea about the next steps. The same fuselage skin is projected into an elastic surface which is designed as a model of gravel-sand. Comparing both cases it is seen that the impactor penetrates into the elastic target surface.

Secondly, internal structure of the fuselage is modeled and associated with fuselage skin. This combined body is projected into the rigid surface and then into the soil model. For the first case, very detailed analysis is carried out. The analysis is repeated for different stacking sequences of carbon/epoxy laminate. Table 19 shows the maximum stresses exerted on the fuselage for different cases. The results are parallel to the ones made in preliminary analyses. Maximum stress exerted on a composite part is directly related to stacking sequences. According to Table 19, best case is found, which is the case with minimum stress. The further analyses are completed according to best case stacking sequence. In the second case of this second part, rigid surface is changed with soil model. As it can be predicted, maximum stress exerted on the fuselage is decreased. It is observed that elastic surface eliminates some part of the impact force.

Thirdly, the whole wing is imported into MSC.Patran. It is scaled and located so that it fits with the fuselage model. Then, the necessary links and associations are established. The fuselage, internal structure and wing completion is projected into rigid surface and soil model. The results are similar to previous ones. The stress exerted on the body is decreased as the target surface becomes elastic. In this part it is also examined how the stress wave moves from fuselage to wing and how wing deforms after the impact.

In the final part leading and trailing edge spars are added to the wing skin. As a result of this the structural stiffness of the wing is increased. In this final case stress

concentration is especially observed at wing-fuselage junction. That brings out the fact that the designer should be ready to observe cracks or fractures at that point if necessary precautions are not taken.

6.2. RECOMMENDATIONS

After all the analyses are completed, author's recommendation can be summarized as follows:

The literature survey and analyses including composite plates show that stacking sequence is an important part of manufacturing composites. When the subject of the study is a belly landing UAV, special attention should be focused on the composite parts of the fuselage. After accomplishing this study, it is observed that the best stacking sequence is composed of 45 degree layup of laminates for "Güventürk" Mini UAV System. However it should be noted that there are an infinite number of possibilities of creating a composite layup. 45 degree stacking sequence gives the optimum stress values among the other layups analyzed in this study.

Nevertheless, this work gives the opportunity of optimizing the current design of "Güventürk" Mini UAV and understanding the importance of composite design of the unmanned aerial vehicles in "mini" category.

6.3. FUTURE WORKS

Following works can be made in the future.

- Analysis of belly landing including whole aircraft model: Fuselage, Wing, Tail.
- Aircraft model can be improved to include all details like stiffeners, fairings and other internal and external parts.
- Fuselage wing connection region can be modeled by providing a wider load path through the generation of a flange surface which exists in the actual manufactured airplane. The existence of the flange surface is expected to reduce the stress concentration along the intersection of the present cut-out in the fuselage and wing.
- Failure and type of failure (delamination, crack, complete failure) can be analyzed. Results can be compared with experimental results of Choi, H.Y., Chang, F.K. [34]

- Elastic soil model can be improved: DYMAT14, “Soil and Crushable Foam Model” can be employed and resulting model can be solved in LS-DYNA.
- Variation of landing conditions can be examined:
 - Landing in cross wind: velocity component in y direction appears.
 - Gust and impulsive wind: angular components of velocity appear.
 - Landing at a nonzero pitch angle: nose first / tail first impact
- Examining ground conditions: assuming Turkish Armed Forces may fly this UAV, possible area of operations can be guessed. Design can be optimized according to the characteristic of the landing zone.
- IMPACT, a free explicit dynamic finite element program can be used to solve the belly landing case and results can be compared to MSC.Dytran. [35]
- Preliminary analysis can be extended by using different impactor shapes and the results can be compared with experimental results of Mitrevski, T., et al. [36]

REFERENCES

1. Maj. Jones, C.A., "*Unmanned Aerial Vehicles (UAVs) an Assessment of Historical Operations and Future Possibilities*", 1997
2. Office of the Secretary of Defense, "*Unmanned Aircraft Systems Roadmap 2005-2030*", August 2005
3. Unmanned Vehicle Systems International web site, "http://www.uvs-info.com/Yearbook2007/158_UAS_Categories-Tables-Figures.pdf", as accurate of 11 March, 2009
4. W.J.Stronge, "*Impact Mechanics*", Cambridge University Press, 2000
5. Kinslow, "*High-Velocity Impact Phenomena*", Academic Press, 1970
6. Hiermaier, S., "*Structures Under Crash and Impact*", Springer, 2008
7. Erarslanoğlu, G., Ardiç, E.S., Kayran, A., Bolcan, C., "*A Method of Failure Prediction in Laminated Composites Subjected to Low Velocity Impact*", Proceedings of Second Biennial European Joint Conference on Engineering Systems Design and Analysis (ESDA), Vol. 2, pp. 111-118, 1994.
8. Tsartaris, N., Dolce, F., Polimeno, U., Meo, M., Guida, M., Marulo, F., Riccio, M., "*Low velocity impact behavior of fiber metal laminates*", 7th International Conference on Composite Science and Technology, 20-22 January, 2009
9. Chou, P., Matsumoto, G., "*DYT101*", MSC.Software Corporation, January 2005
10. de Morais, W.A, Monterio, S.N., d'Almeida, J.R.M., "*Effect of the laminate thickness on the composite strength to repeated low energy impacts*", 2004
11. Jones, R.M., "*Mechanics of Composite Materials*", Hemisphere Publishing Cooperation, 1975
12. Choi, I.H., "*Low-velocity impact analysis of composite laminates under initial in-plane load*", 2008
13. Shyr, T.W., Pan, Y.H, "*Impact resistance and damage characteristics of composite laminates*", 2003

14. Sutherland, L.S., Soares, C.G., *“Effect of laminate thickness and of matrix resin on the impact of low fibre-volume, woven roving E-glass composites”*, 2004
15. Belingardi, G., Vadori, R., *“Low velocity impact tests of laminate glass-fiber-epoxy matrix composite material plates”*, 2001
16. Denning, K., *“Design, Construction, and Testing of a High-Speed Light Weighted UAV”*, AIAA 3rd “Unmanned Unlimited” Technical Conference, Workshop and Exhibit. 20-23 September 2004, Chicago, Illinois
17. Greszczuk, L. B., *“Damage in Composite Materials due to Low Velocity Impact”*, Impact Dynamics, pp. 55-94, John Wiley & Sons, 1982
18. Whittemore, H.L., Petrenko, S.N., *“Friction and Carrying Capacity of Ball and Roller Bearings”*, Scientific Papers of the Bureau of Standards no. 201, 1921
19. Daniel, I. M., Ishai, O., *“Engineering Mechanics of Composite Materials”*, Oxford University Press, pp. 164-166, 1994
20. *“MSC.Dytran Theory Manual”*, MSC.Software Corporation, 2005
21. MSC.Patran Website, *“<http://www.mscsoftware.com/products/patran.cfm>”*, as accurate of 01 May, 2009
22. MSC.Nastran Website, *“http://www.mscsoftware.com/products/msc_nastran.cfm”*, as accurate of 01 May, 2009
23. Dassault System Website, *“<http://www.3ds.com/products/catia/welcome/>”*, as accurate of 01 May, 2009
24. MSC.Dytran Website, *“www.mscsoftware.com/products/dytran.cfm”*, as accurate of 01 May, 2009
25. Turgut, T., *“Manufacturing and Structural Analysis of a Lightweight Sandwich Composite UAV Wing”*, 2007
26. MicroPilot Web Site, *“<http://www.micropilot.com/>”*, as accurate of 01 May, 2009
27. Turgut, T., Kayran, A., et.al *“Vakum Torbalama Yöntemi ile Kompozit Malzemedden Yapı Üretimi Örnek Bir Havacılık Uygulaması”*, Mühendis ve Makina, Vol. 48, No. 566, 2007, pp. 14-21
28. National Institute of Standards and Technology Web Site, *“<http://ts.nist.gov/standards/iges/>”*, as accurate as 1 May, 2009
29. Anderson, J. D., *“Aircraft Performance and Design”*, McGraw-Hill Publishing Co., 1999

30. Kargin, V., "*Design of an Autonomous Landing Control Algorithm to a Fixed Wing UAV*", 2007
31. Ramalingam, V. K., Lankarani, H. M., "*Analysis of impact on soft soil and its application to aircraft crashworthiness*", International Journal of Crashworthiness. Vol. 7, No. 1, 2002, pp. 57-65.
32. Bowles, J.E., "*Foundation Analysis and Design*", McGraw-Hill Publishing Co., 1996
33. Harr, M.E., "*Foundations of Theoretical Soil Mechanics*", McGraw-Hill Publishing Co., 1966
34. Choi, H.Y., Chang, F.K., "*Impact Damage Resistance of Graphite/Epoxy Laminated Composites*", Polymer Engineering and Science, September 1991, Vol. 31, 18, p.1294-1300
35. Impact- a Free Explicit Dynamic Finite Element Program, "<http://impact.sourceforge.net>", as accurate of 28 April, 2009
36. Mitrevski, T., Marshall, I.H., et al. "*The effect of impactor shape on the impact response of composite laminates*", 2004

APPENDIX A

IMPORTING CAD MODEL INTO PATRAN

In this part, importing IGES files into MSC.Patran is explained.

Figure 71:

Create a new database

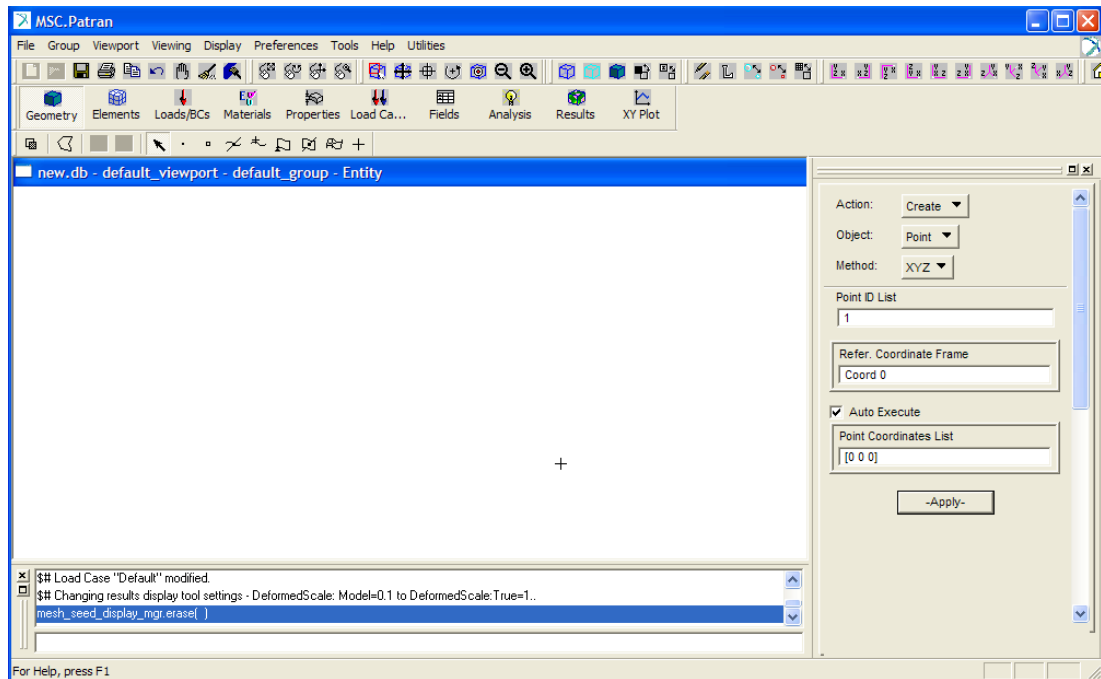


Figure 71: Importing IGES files, Screenshot -1

Figure 72:

From "File", click "Import..."

Object: "Model", Source: "IGES"

Select the igs file and click "APPLY"

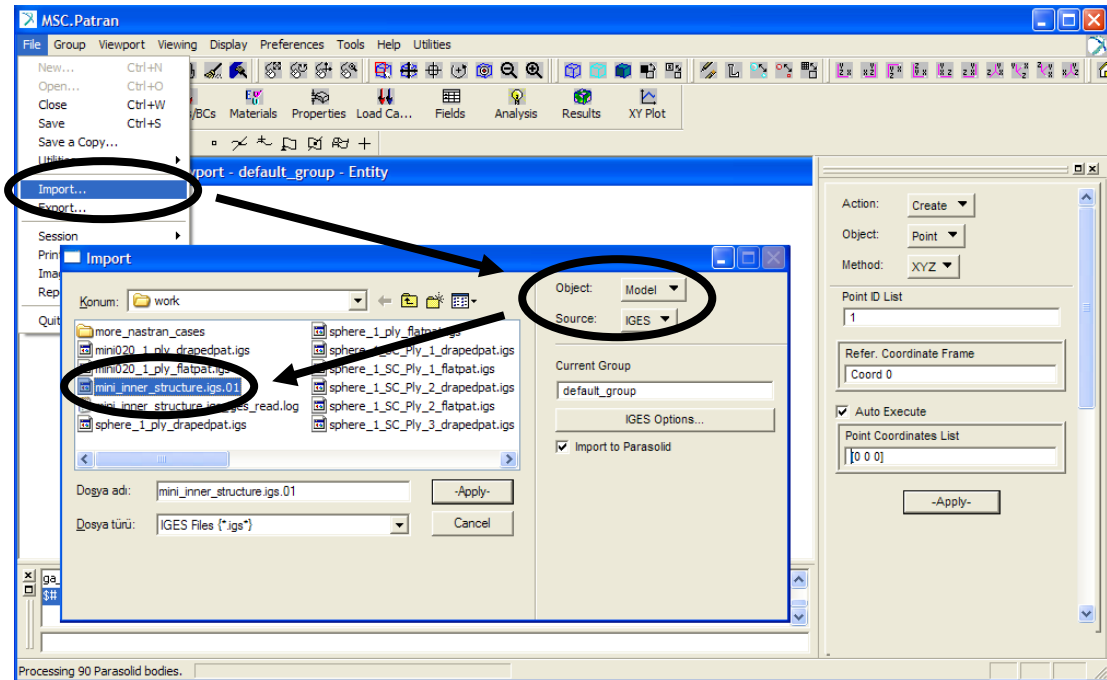


Figure 72: Importing IGES files, Screenshot -2

Figure 73:

Selected igs file is imported.

“IGES Import Summary” is shown.

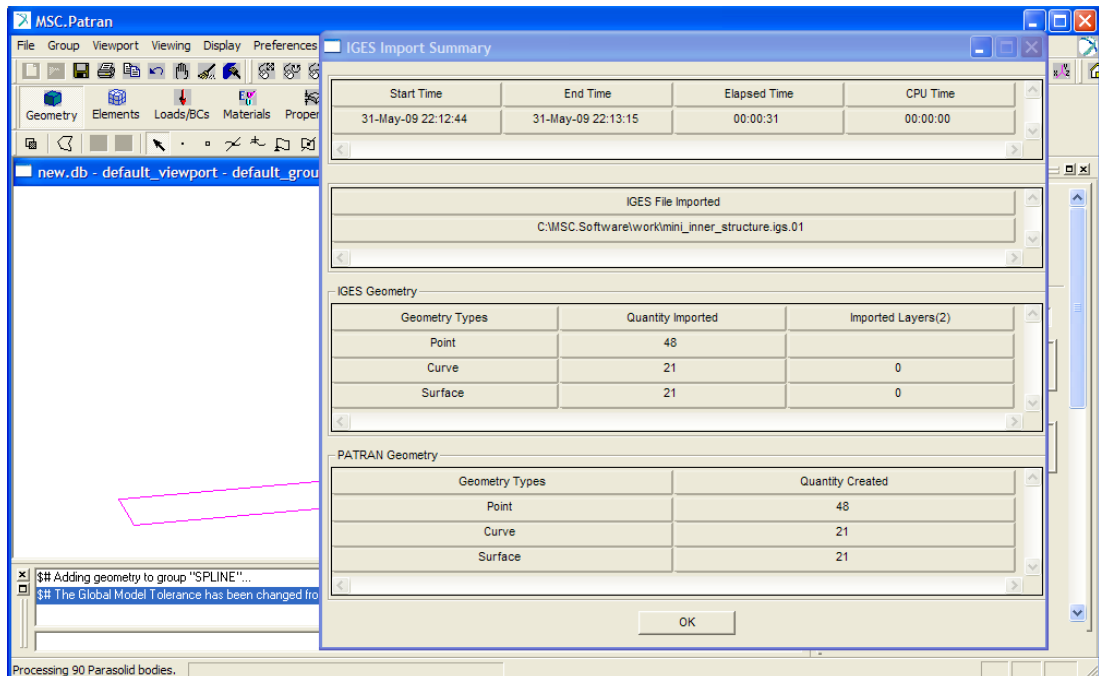


Figure 73: Importing IGES files, Screenshot -3

APPENDIX B

PATRAN LAMINATE MODELER TOOL

In this part “Laminate Modeler Tool” is explained.

Figure 74:

First, a material should be defined in the “Materials” menu. “carbon_epoxy” is defined for this example.

Action: “Create”, Object: “LM_Material”, Method: “Add”

Analysis Material: Plies will be made up of this material

Thickness: “0.133”, Maximum Strain: “10”, Warp/Weft Angle: “90” (for carbon/epoxy)

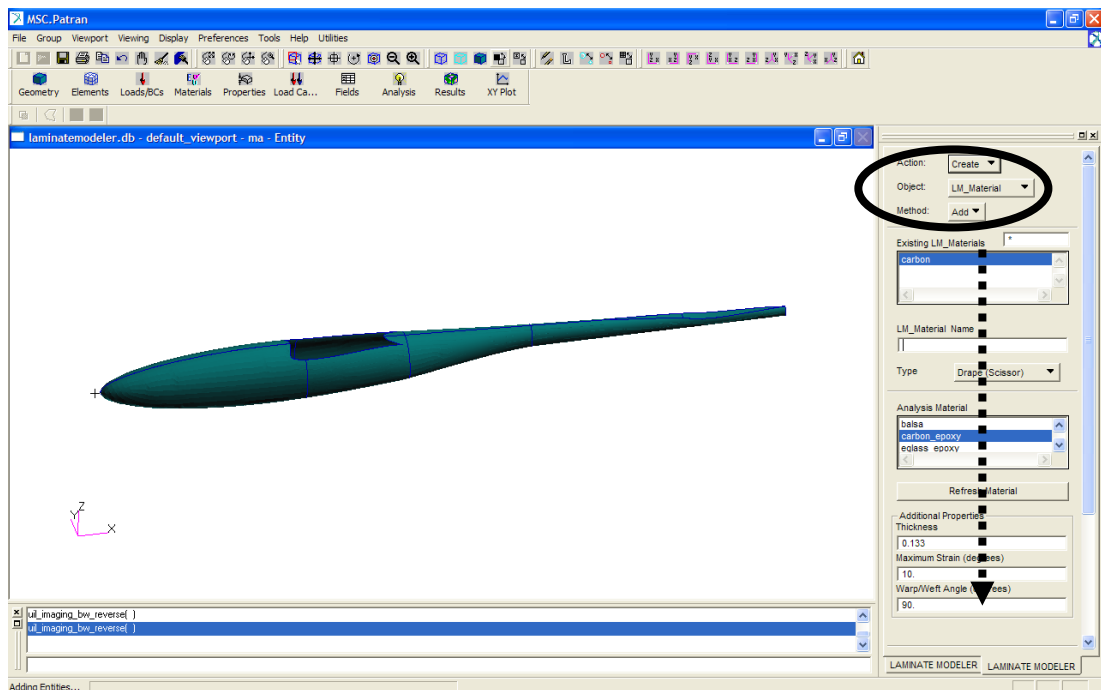


Figure 74: Laminator Modeler, Screenshot -1

Figure 75:

A ply must be generated in order to build a layup

Object: “LM_Ply”, Method: “Recreate”

Select Area: The area on which the ply is applied

Start Point: The point at which the ply first contacts the body

Select application direction: Can be normal to the surface or at any orientation

Reference Direction: The direction according to which the ply orientation takes place

Reference angle: This angle decides the orientation of the composite laminae.

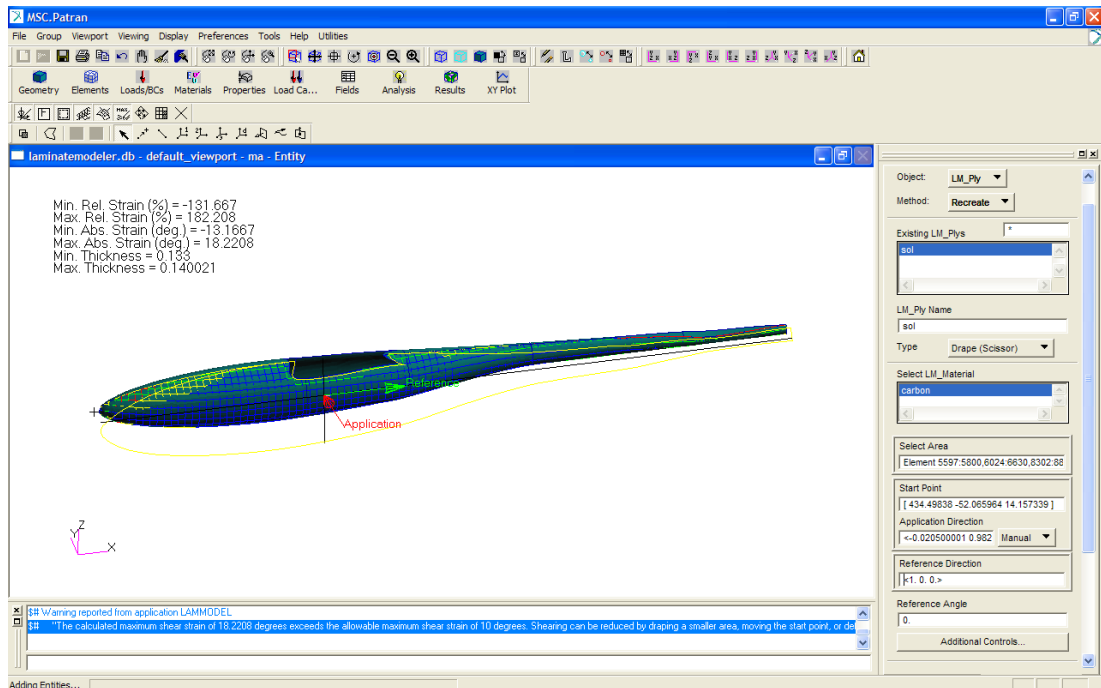


Figure 75: Laminate Modeler Screenshot -2

After ply is applied, maximum strain angles might be more than it was defined previously. In this example, absolute maximum strain angle was defined to be 10 degrees but it turned out to be -13.1667 and 18.2208 degrees after covering the body. Excessive strain angles can be reduced by defining splits. (Click additional controls)

Figure 76:

Control Parameters: “Boundaries”

Select 2D element edges: click on the element edges which are shown in red. Red means excessive strain angle.

Click “Add” and click “Apply”

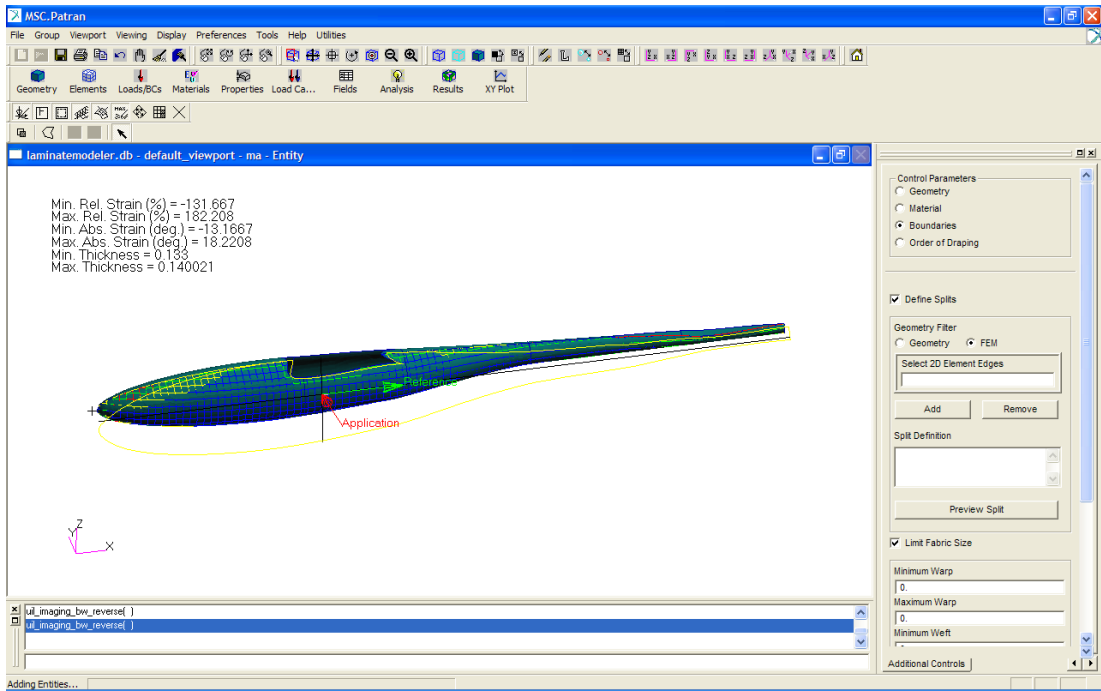


Figure 76: Laminate Modeler Screenshot -3

Figure 77:

After building several splits the absolute maximum strain angle exerted on the ply reduces below 10 degrees. The ply is now suitable for building up a laminate.

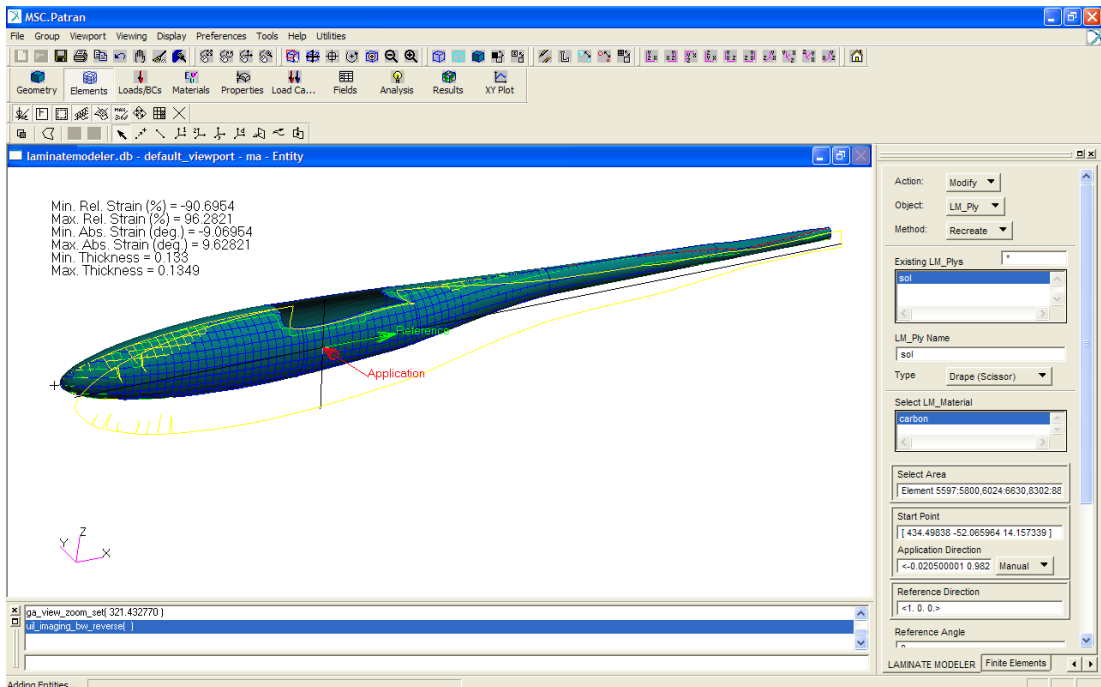


Figure 77: Laminate Modeler Screenshot -4

Figure 78:

Left hand side of the body is similarly covered by carbon/epoxy laminate. Excessive strain angles are reduced by defining splits on necessary regions.

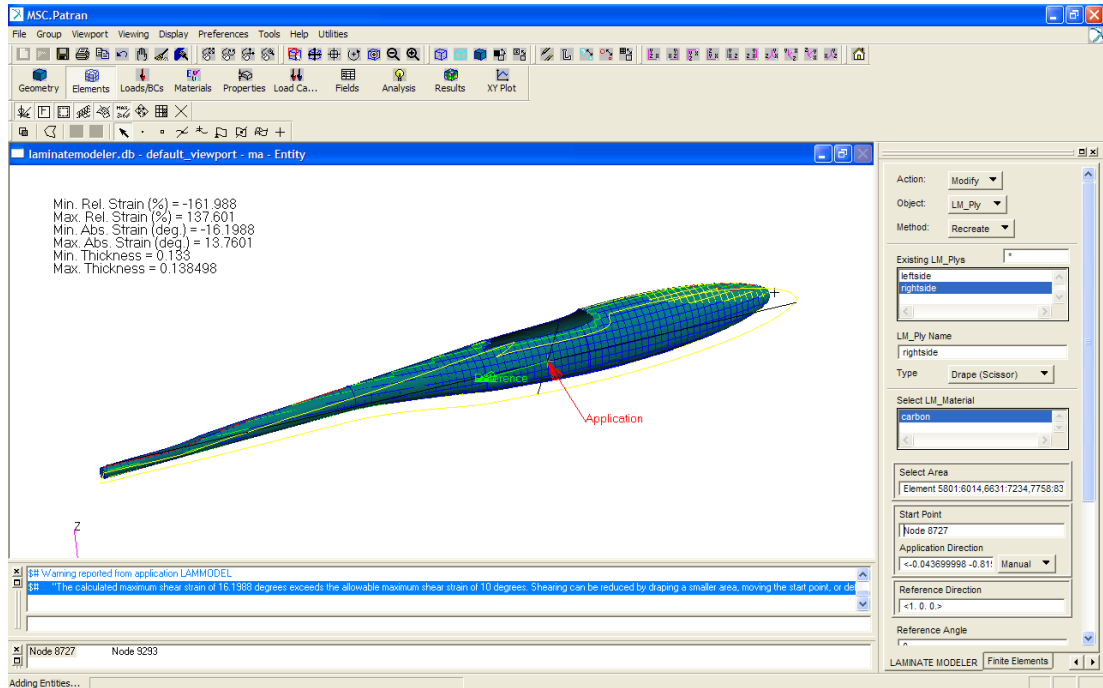


Figure 78: Laminate Modeler Screenshot - 5

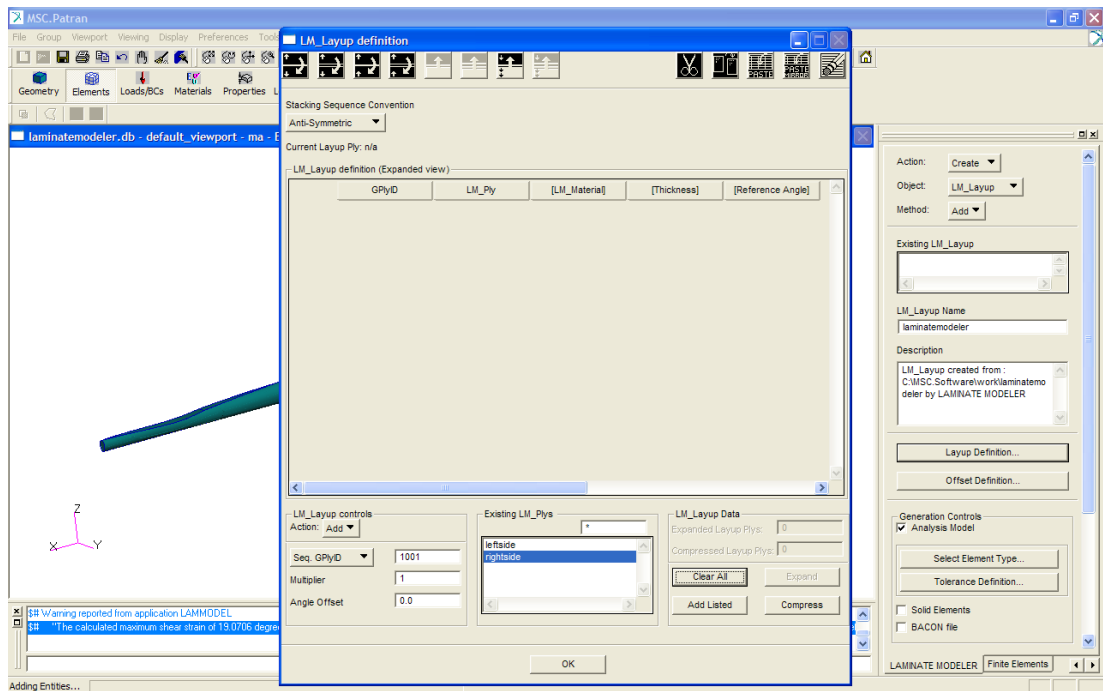


Figure 79: Laminate Modeler Screenshot – 6

Figure 79:

Since left and right hand sides of the body is covered with plies, a layup can now be established.

Action: "Create"

Object: "LM_Layup"

Click on Existing LM_Plys and build a layup

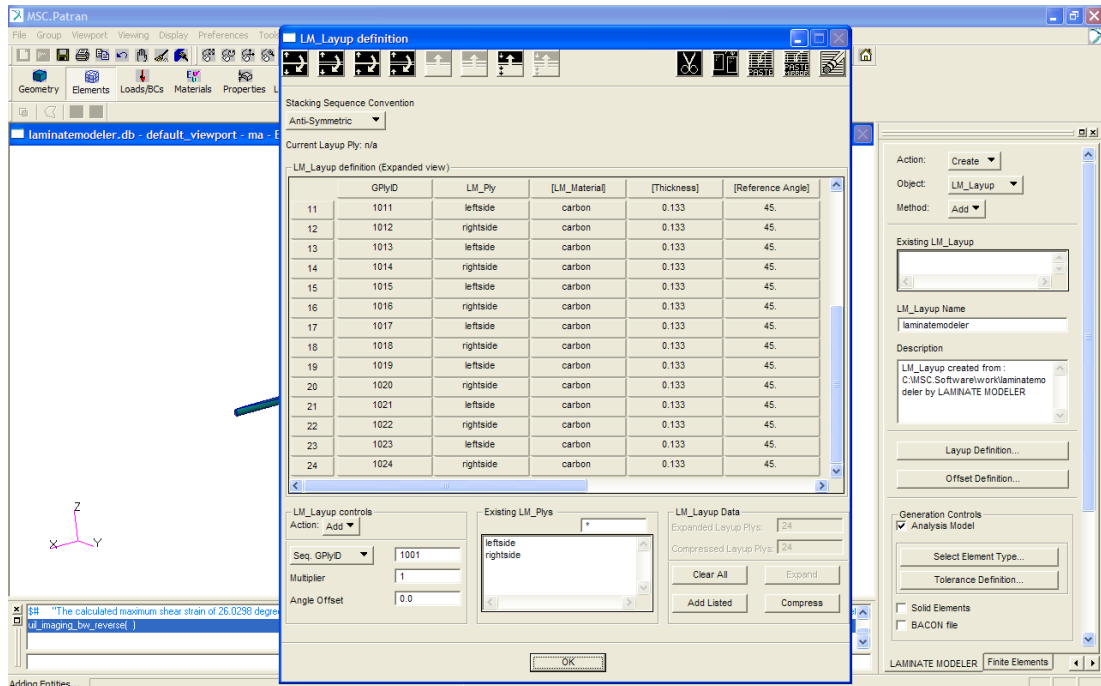


Figure 80: Laminate Modeler Screenshot – 7

Figure 80:

24 layers of ply are used to build the composite layup. Each side of the body is covered with 12 layers. Reference angle shows the orientation of the plies.

Click "OK"

Click "Apply"

Laminate Modeler will associate the properties of composite layup with corresponding elements. No any additional property definition is needed.

APPENDIX C

SOLUTION STEPS OF AN EXAMPLE PROBLEM

In this part, solution steps of a sample problem will be explained. A rigid ball is projected on a steel plate. In order to preserve simplicity of tutorial the pre-modeled geometry will be imported into MSC.Patran. Then the geometry will be meshed and properties will be defined. Boundary conditions and initial velocity of the ball will be set. Finally, analysis options will be explained and results will be shown.

Opening a new database:

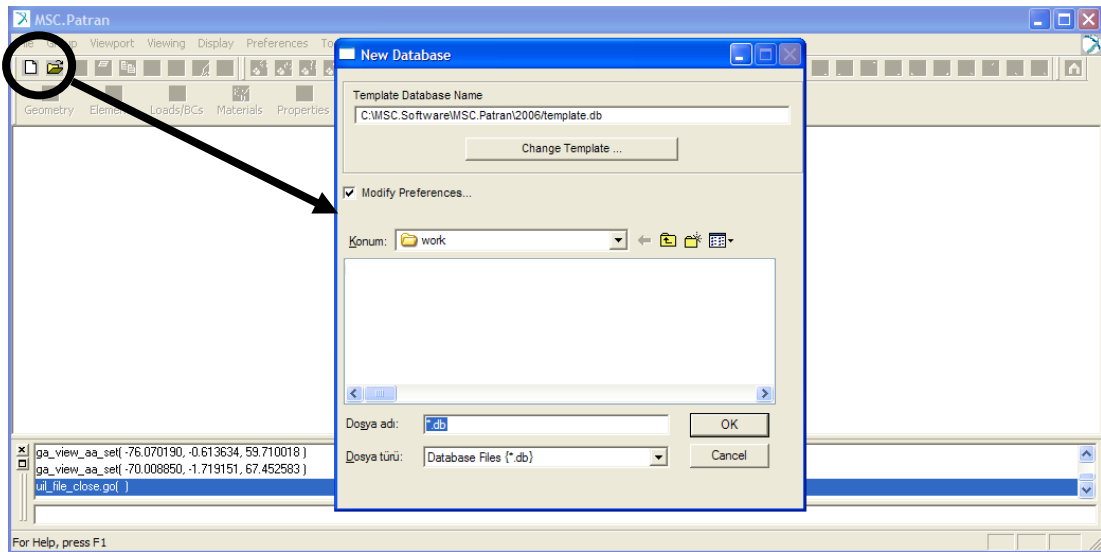


Figure 81: Solution steps, Screenshot -1

Create a new database (Figure 81) and select MSC.Dytran as “Analysis Code” (Figure 82)

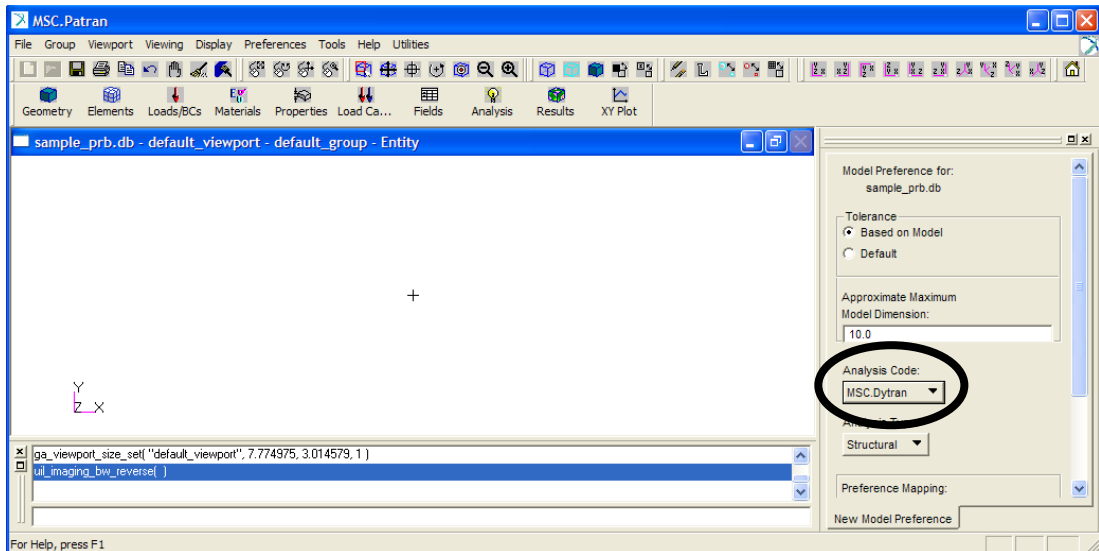


Figure 82: Solution steps, Screenshot -2

Importing geometry:

Geometry is imported by following the steps explained in Appendix A. Imported geometry has following properties:

Edge length of steel square plate = 1 m

Radius of rigid ball = 0.1 m

After importing the geometry, plate and ball will be seen as in Figure 83.

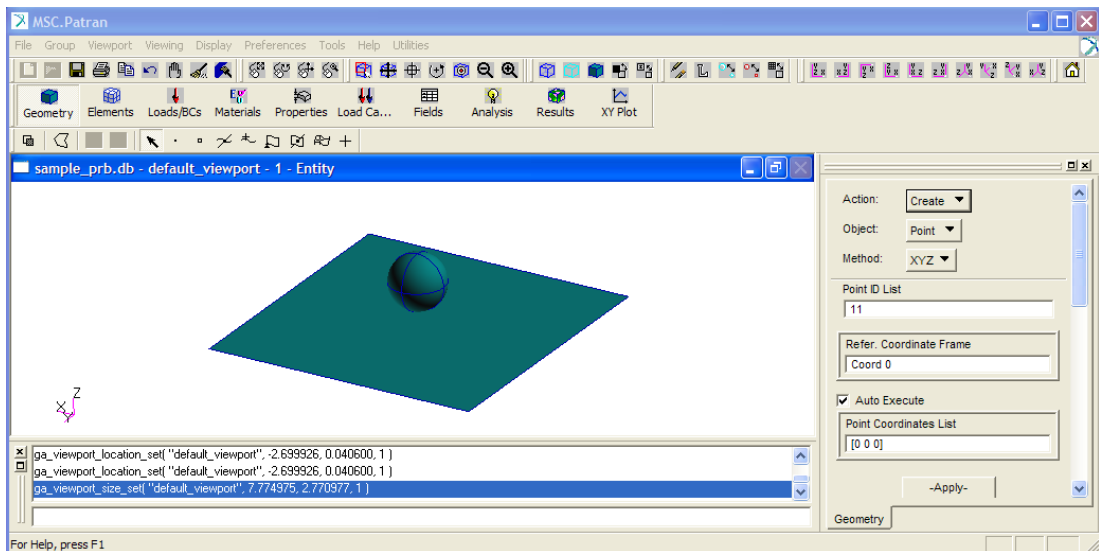


Figure 83: Solution steps, Screenshot -3

Meshing: (see Figure 84)

Click on “Elements” tab.

Action: “Create”, Object: “Mesh”, Type: “Surface”

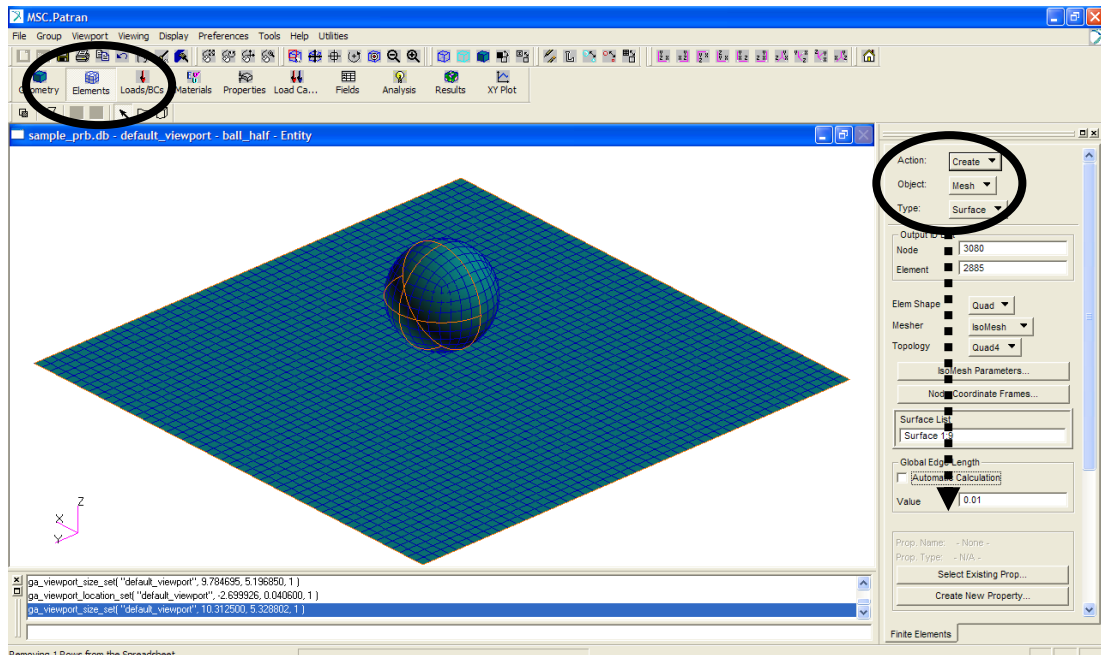


Figure 84: Solution steps, Screenshot -4

Element Shape: Selects the shape of the element. It can be “QUAD” or “TRIA”

Mesher: “ISOMESH”. For some complex geometry ISO may not be applicable. “PAVER” should be selected.

Surface List: Select all surfaces (from Surface 1 to Surface 9)

Global Edge Length: The time step size, solution time and precision of solution is affected by this value. In this example it is selected to be 0.02

Click “APPLY”

Grouping:

Click “Group”, “Create”

New Group Name: “Plate”

Entity Selection: Select all elements on the plate

Click “APPLY”

New Group Name: “Ball”

Entity Selection: Select all elements on the ball

Click “APPLY”

Boundary Conditions and Initial Velocity:

Click “Loads/BCs” tab. (See Figure 85)

Action: “Create”, Object: “Displacement”, Type: “Nodal”

New Set Name: “Fixed”

Click “Input Data” (Figure 86)

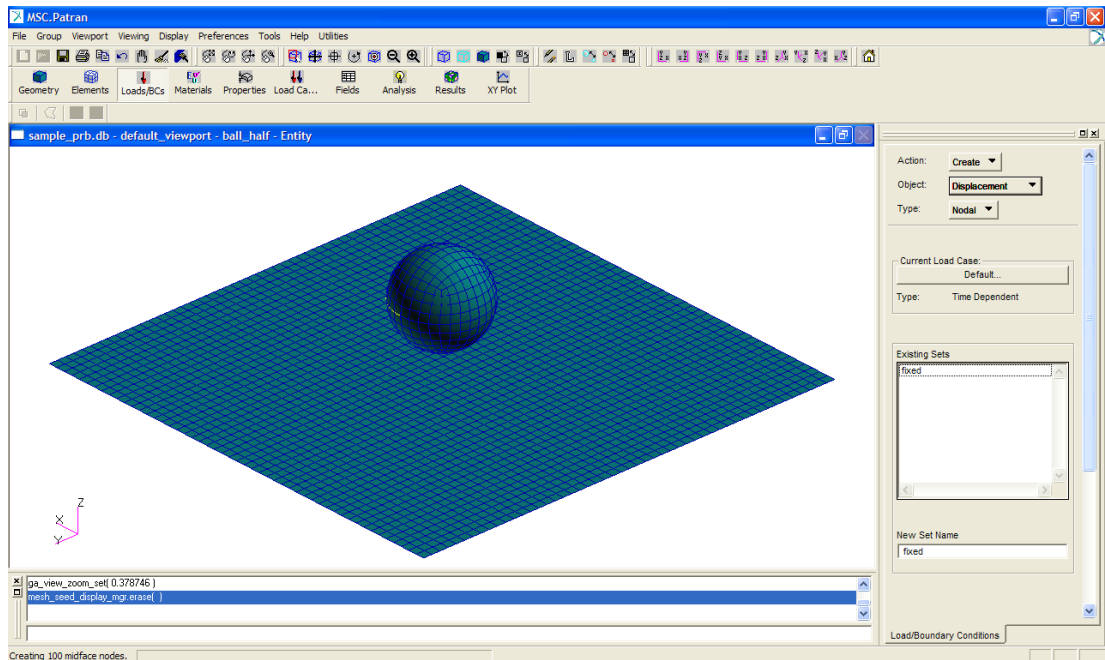


Figure 85: Solution steps, Screenshot -5

Translations: “ <0, 0, 0> “, Rotations: “ <0, 0, 0> “ (Fixed Edges)

Click “APPLY”

Click “Select Application Region”

Select: “FEM” (See Figure 87)

Select Nodes: Select all nodes at the edge of the plate

Click “OK”

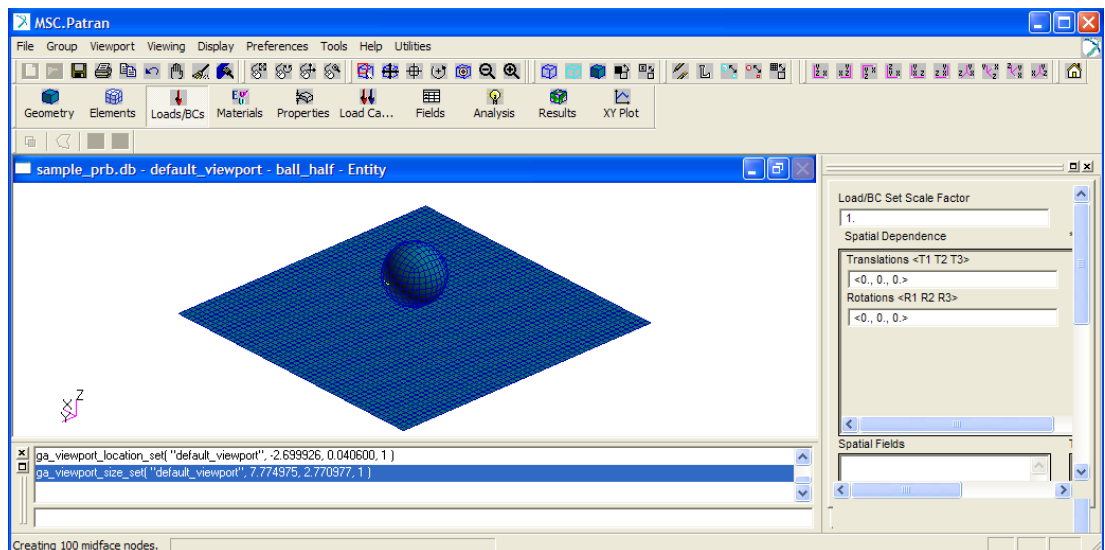


Figure 86: Solution steps, Screenshot -6

Click "OK"

Click "APPLY"

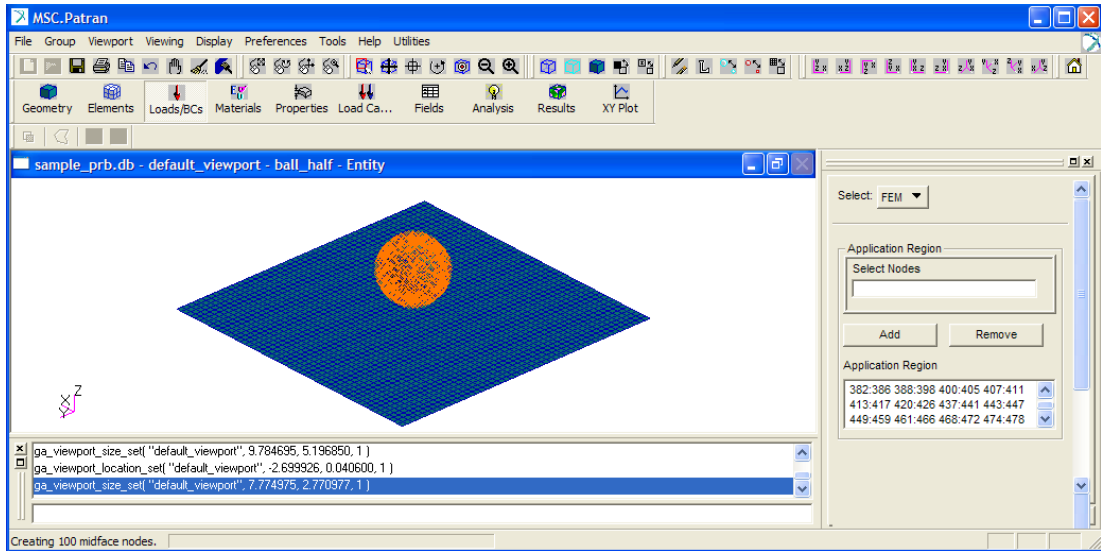


Figure 89: Solution steps, Screenshot -9

Materials:

Select "Materials" tab (See Figure 90)

Action: "Create", Object: "Isotropic", Method: "Manual Input"

Material Name: "rigid_ball"

Click "Input Properties"

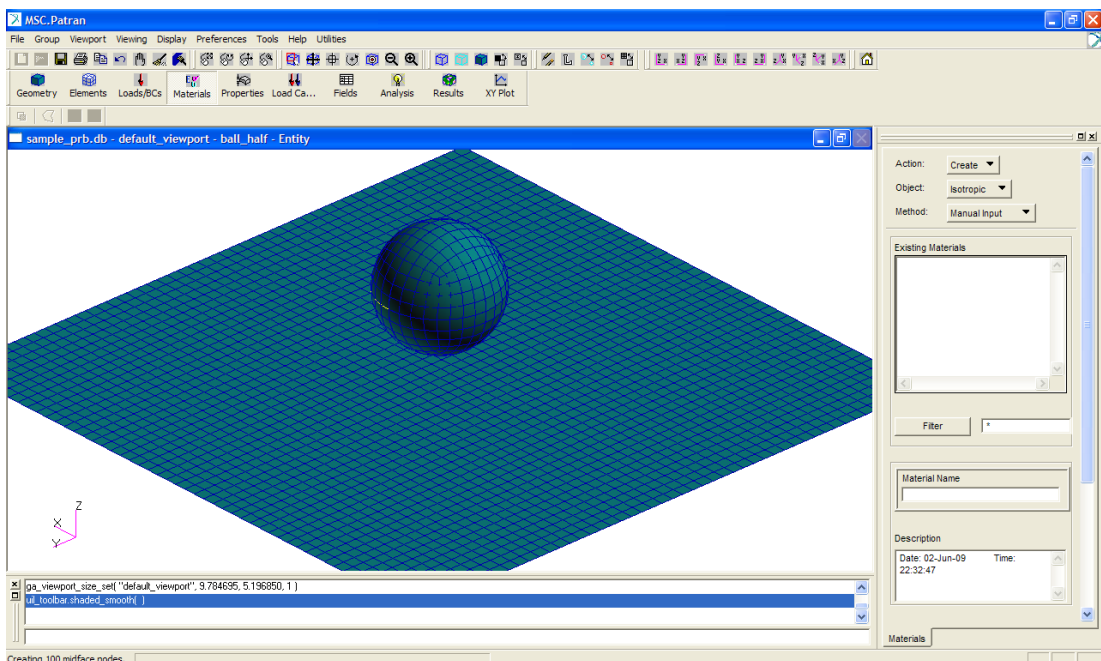


Figure 90: Solution steps, Screenshot -10

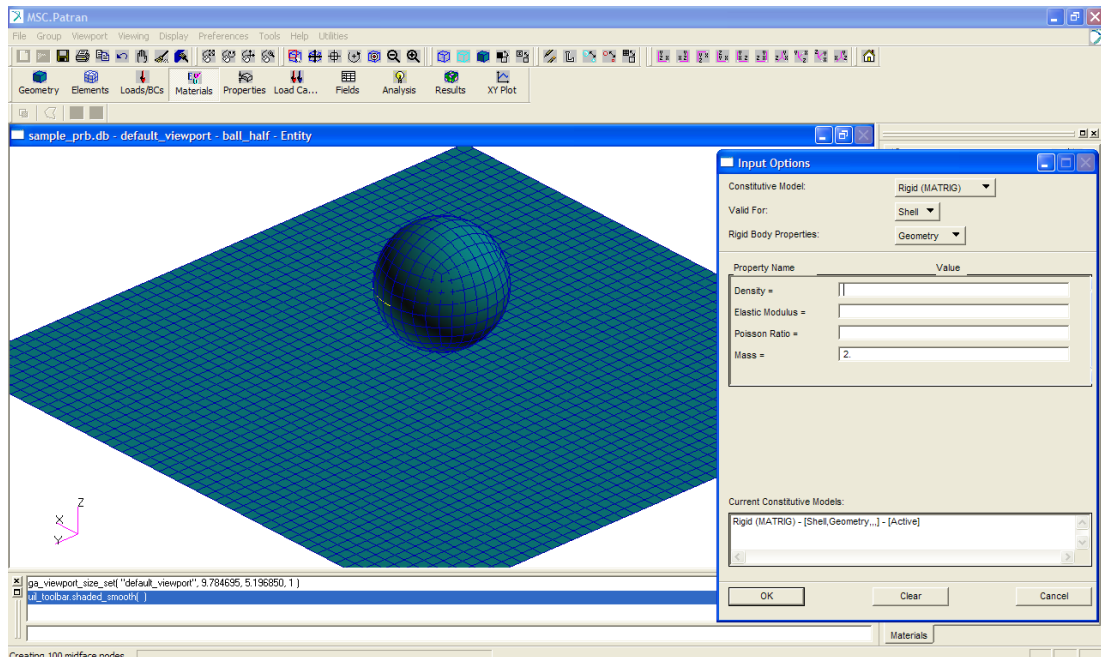


Figure 91: Solution steps, Screenshot -11

Constitutive Model: “Rigid (MATRIG)”, Valid for: “Shell” (See Figure 91)

Rigid Body Properties: “Geometry”

Mass: “2”, (2 kg mass for rigid ball)

Click “OK”, Click “APPLY”

Rigid Ball material is created,

Material Name: “steel”

Click “Input Properties” (See Figure 92)

Constitutive Model: “LinElas (DMATEL)”, Element Type: “Membrane”

Density: “7850” (7850 kg/m³ for steel)

Elastic Modulus: “300E9” (300GPa for steel)

Poisson Ratio: “0.3”

Click “OK”, Click “APPLY”

Steel material is created.

Now, these materials can be used to define properties for various sections of geometry. Ball geometry will be defined as “Rigid Ball” and the plate will be defined as “Steel”.

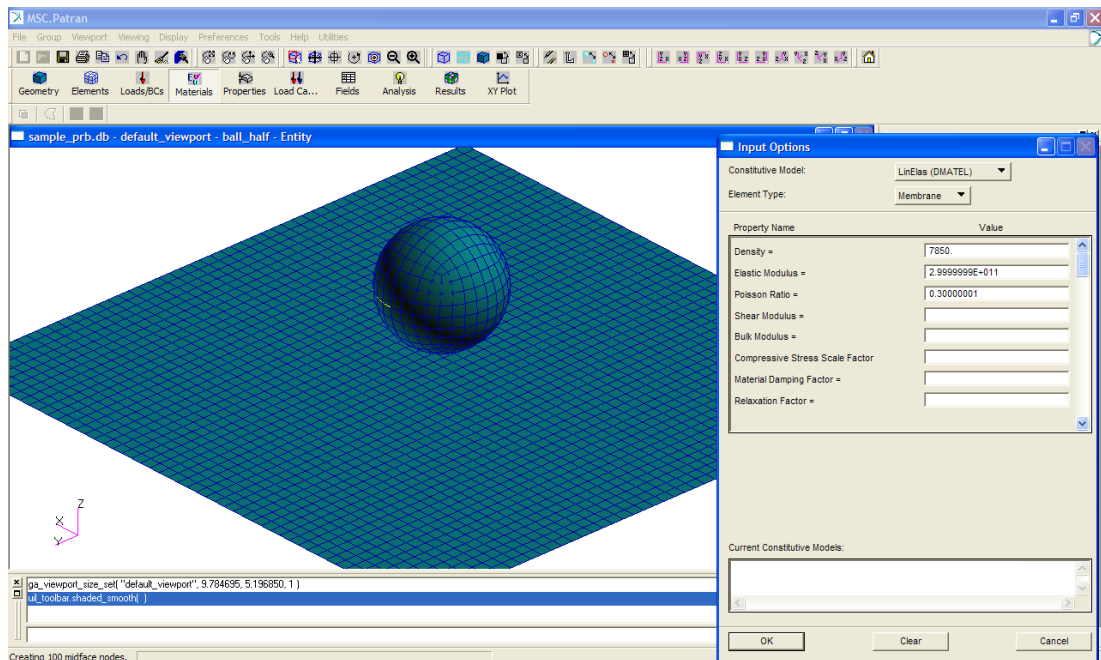


Figure 92: Solution steps, Screenshot -12

Click Properties

Action: "Create", Object: "2D", Type: "Shell" (See Figure 93)

Property Set Name: "ball_prop", click "Input Properties"

Material Name: click "rigid_ball" from materials list

Thickness: "0.05", Click "OK"

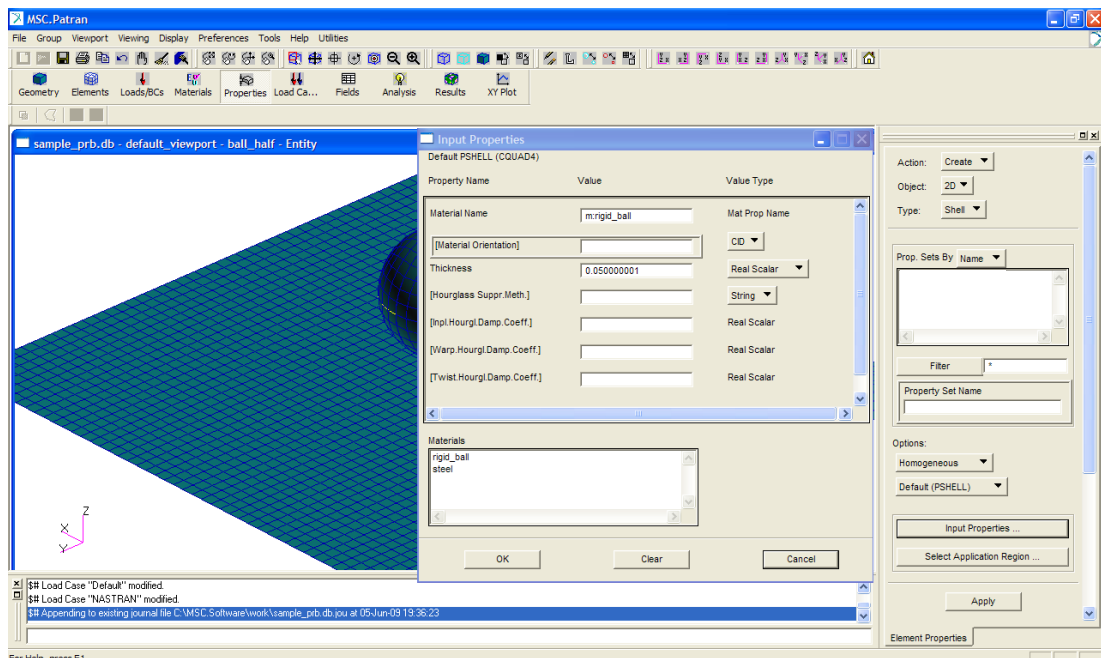


Figure 93: Solution steps, Screenshot -13

Select Application Region: Select all elements of Ball, “Element 1:384”
 Click OK, Click “APPLY”. (Ball elements are now associated with rigid material)
 Material Name: “Plate”, Click “Input Properties” (See Figure 94)
 Material Name: Click “steel” from materials list.
 Thickness: “0.005”, (5 mm)
 Click “OK”
 Click “Select Application Region”, Select all elements of plate, “Element 385:2884”
 Click “OK”, Click “APPLY”. (Plate elements are now associated with steel material)

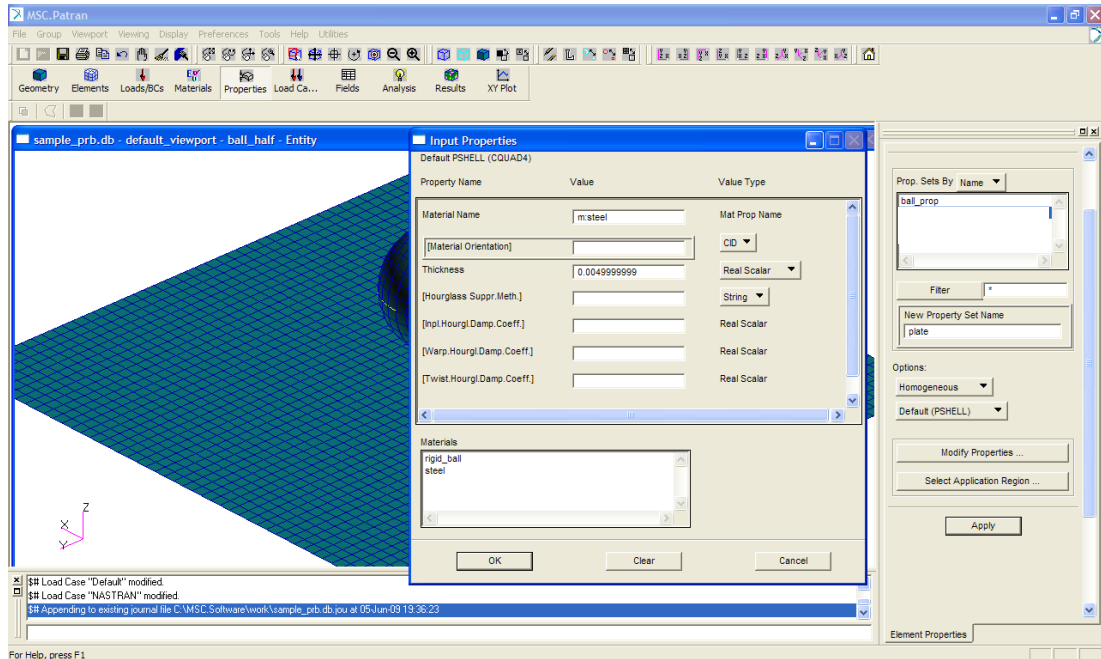


Figure 94: Solution steps, Screenshot -14

Now, it is necessary to define the geometries that will be in contact during impact.
 Since the plate will deform during impact, “contact” should adapt itself accordingly.
 Click “Loads/BCs” Action: “Create”, Object: “Contact” (See Figure 95)
 Type: “Element Uniform”, Option: “Adaptive Master-Slave Contact”
 Click “Select Application Region” (See Figure 96)
 Form Type: “Select Tool”, Type: “Master”, Element Type: “2D”, Contact Side: “Both”
 Geometry Filter “FEM”. Select all elements of ball, “Element 1:384”
 Change Type to “Slave”. Select all elements of plate, “Element 385:2884”
 Click “OK”, Click “APPLY”
 Next step is defining output requests.

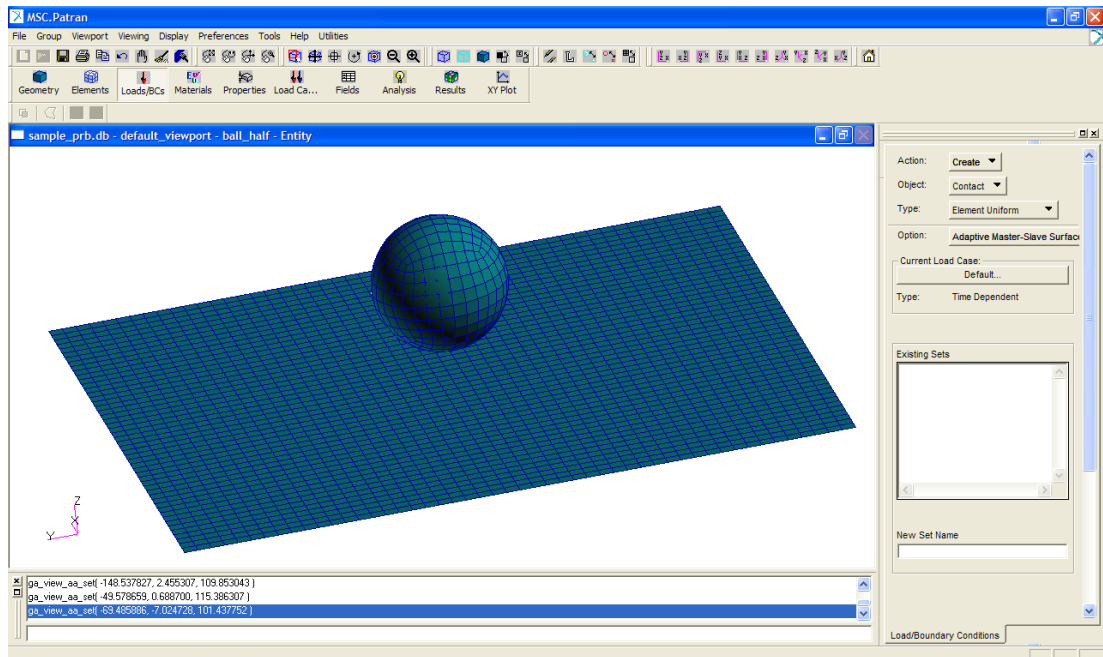


Figure 95: Solution steps, Screenshot -15

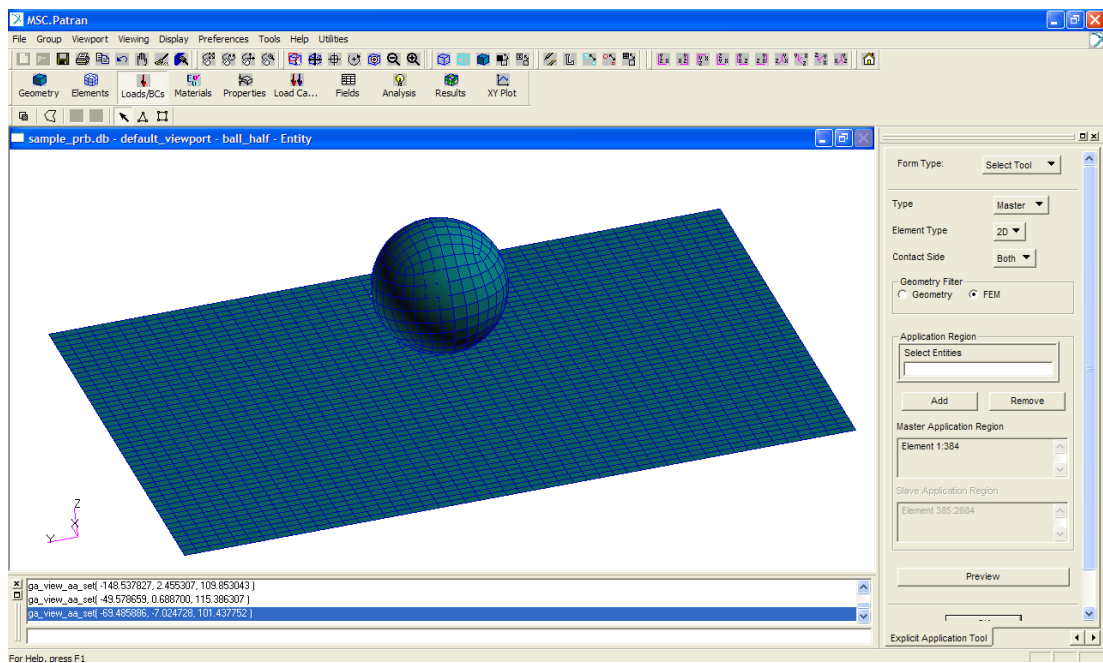


Figure 96: Solution steps, Screenshot -16

Click “Analysis”

Action: “Analyze”, Object: “Input Deck”, Method: “Translate” (See Figure 97)

Job Name: “sample_prb”, Click “Execution Controls”

Click “Execution Control Parameters”

End Step: Decides maximum allowable step size. (12000 for this problem)

Time Step Size at Start: Defines the initial time step size (1E-6 for this problem)
 Minimum Time Step: Defines the allowable minimum step (1E-7 for this problem)
 Click “OK”

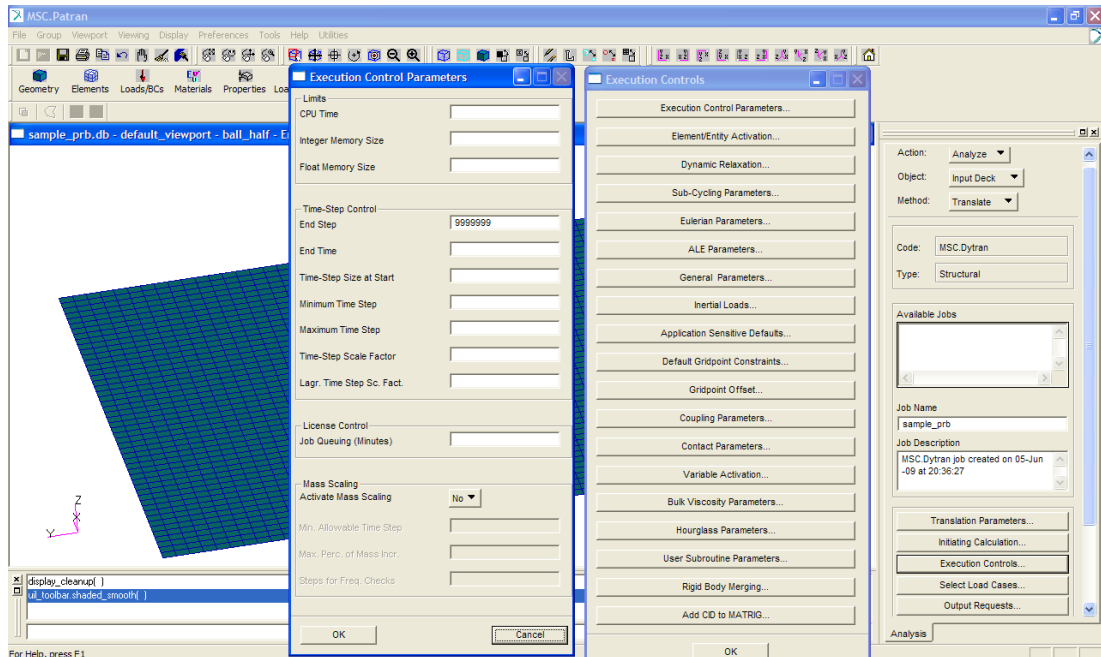


Figure 97: Solution steps, Screenshot -17

Click “Execution Controls”

Result Name: “Result” (See Figure 98)

File Type: “Archive”, Result Type: “Element Output”

Chose “Steps for Output” and “Sampling Rate”

0 THRU END BY: Defines the sequence at which the output is written on file

Click “ADD”, Select Groups for Output: “Plate”

Entity Type: “Sublayer Variables”, Click “Inner, Middle, Outer Layer”

Result Type: “EFFST”

Click “OK”, Click “APPLY”

MSC.Patran creates a file with “dat” extension and that file can be opened and processed by MSC.Dytran.

Open MSC.Dytran (See Figure 99)

Select “sample_prb.dat”, set “Memory” to desired level and click “Play” button.

After solution is completed open MSC.Patran for post processing.

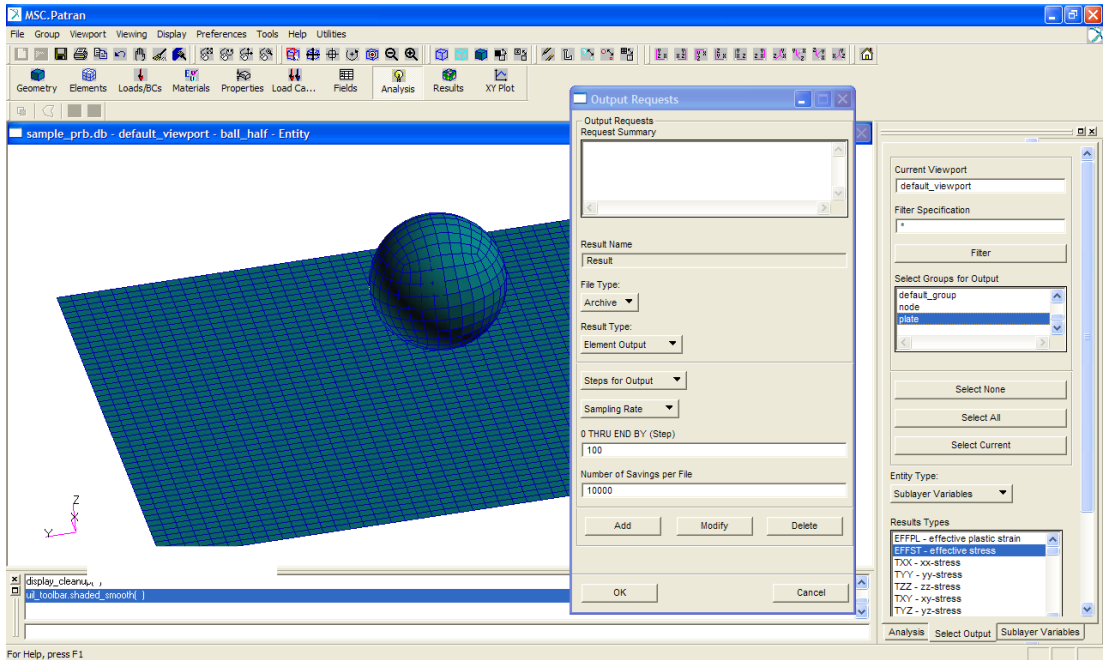


Figure 98: Solution steps, Screenshot -18

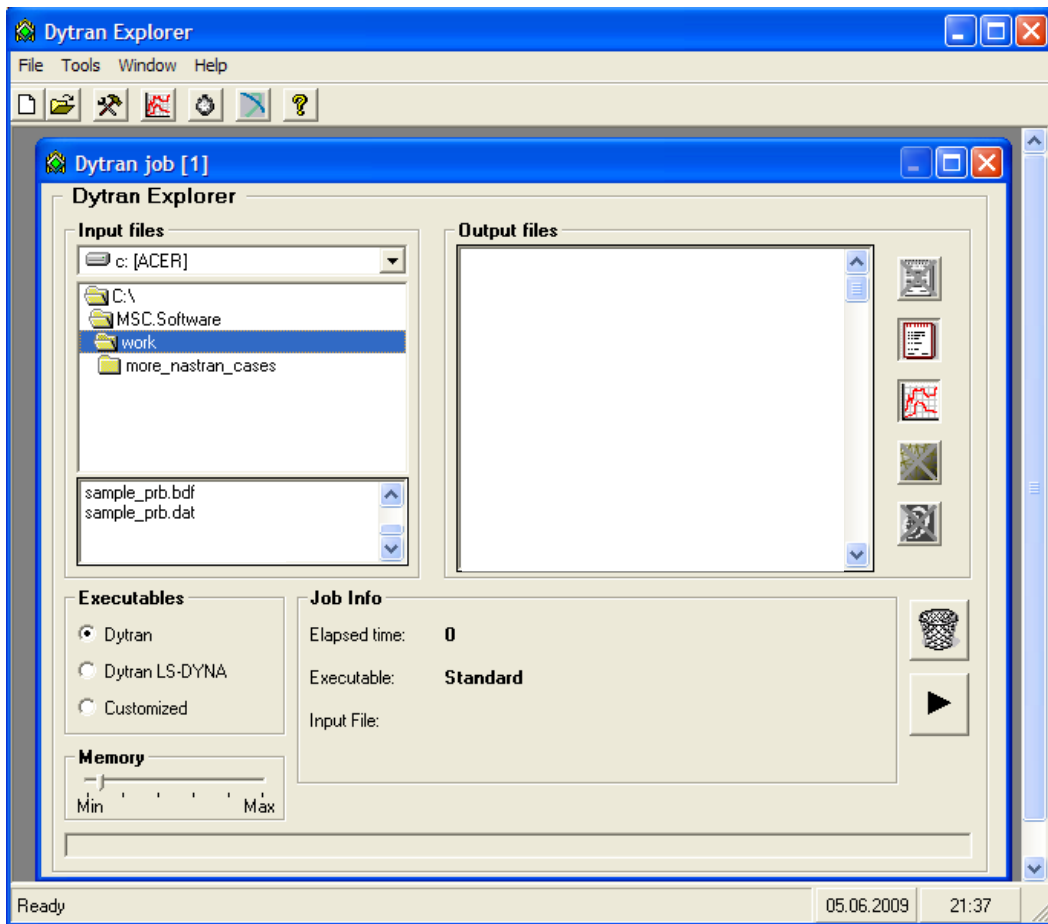


Figure 99: Solution steps, Screenshot -19

Click “Analysis” (See Figure 100)

Action: “Read Archive File”, Object: “Results”, Method: “Attach”

Click “Select Archive File”, Click “SAMPLE_PRB_PLATE_0.ARC”,

Click “ADD”, Click “APPLY”, Click “APPLY”

MSC.Patran will attach the results.

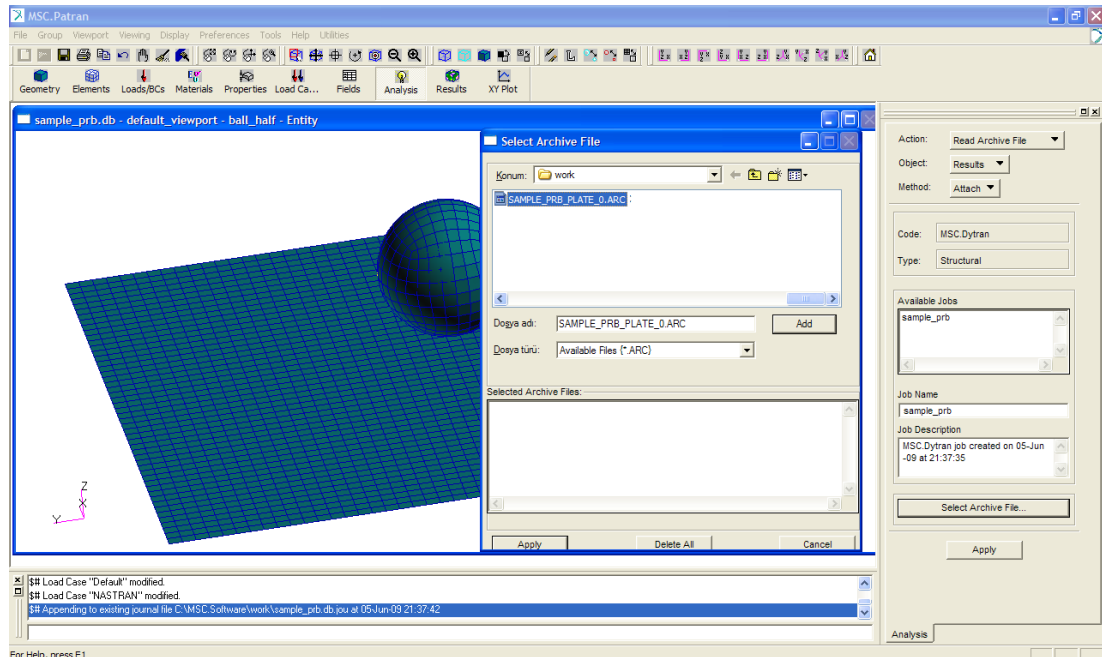


Figure 100: Solution steps, Screenshot -20

Click “Results”

Action: “Create”, Object: “Quick Plot” (See Figure 101)

Select all solution steps.

Fringe Result: “EFFST”, Deformation Result: “Displacement”

Check: “Animate”, Click: “APPLY”

The result will be shown in animation. Instead of animation a single step can also be examined. Select the requested step and click “APPLY” without selecting “Animate”.

A single solution step is shown in Figure 102.

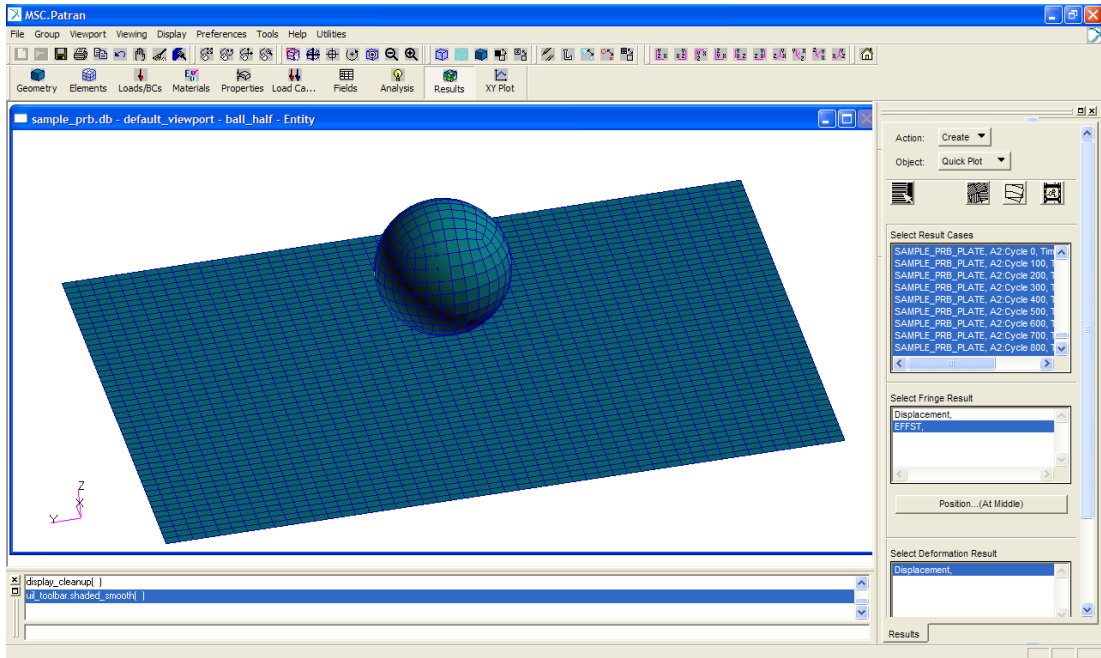


Figure 101: Solution steps, Screenshot -21

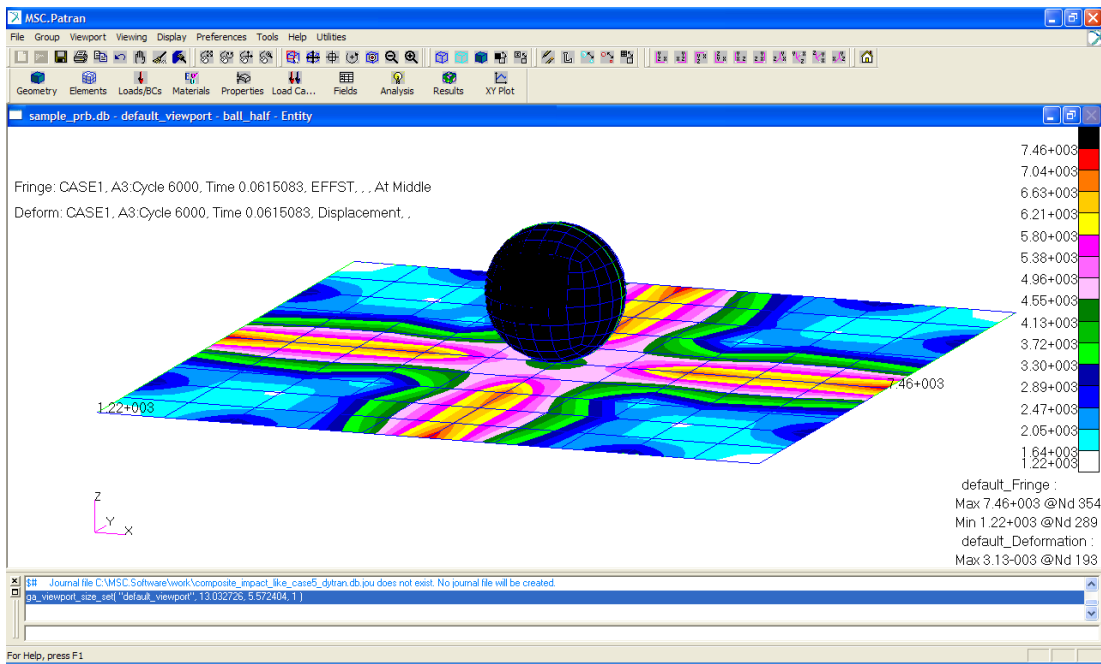


Figure 102: Solution steps, Screenshot -22

APPENDIX D

EFFECT OF MESH SIZE ON THE ANALYSIS

In Chapter 5 Part 3, fuselage shell model was meshed and covered with carbon laminate. Meshing was completed with a global mesh length of 10 mm. In this part, different mesh sizes are examined in order to observe the effect of different mesh sizes on the analysis. 15 mm, 25 mm and finally 50 mm global edge lengths are applied and the fuselage is covered with exactly same carbon laminate.

After repeating the analyses it is observed that varying mesh size changes the maximum stress exerted on the fuselage. The results are tabulated in Table

Table 22: Stress results for different mesh sizes

Global Edge Length (mm)	Number of Elements	Effective Maximum Stress (MPa)
10	2811	353.25
15	1635	433.92
25	541	881.13
50	248	1077.50

As it can be observed, the maximum effective stress increases as the global edge length increases. Considering the decreasing number of elements it can be said that bigger mesh results in less accurate results. Therefore, it is reasonable to accept the smaller element size to be more realistic.

APPENDIX E

IMPACT VELOCITY VS. MAXIMUM DEFLECTION

In Chapter 3.6.3 comparison of quasi-static and explicit finite element solutions was completed and the results were tabulated. In this part, the resolution of the graph is increased by calculating more data points. As it can be seen in Figure 103, the amount of error increases almost linearly as the impact velocity is increased.

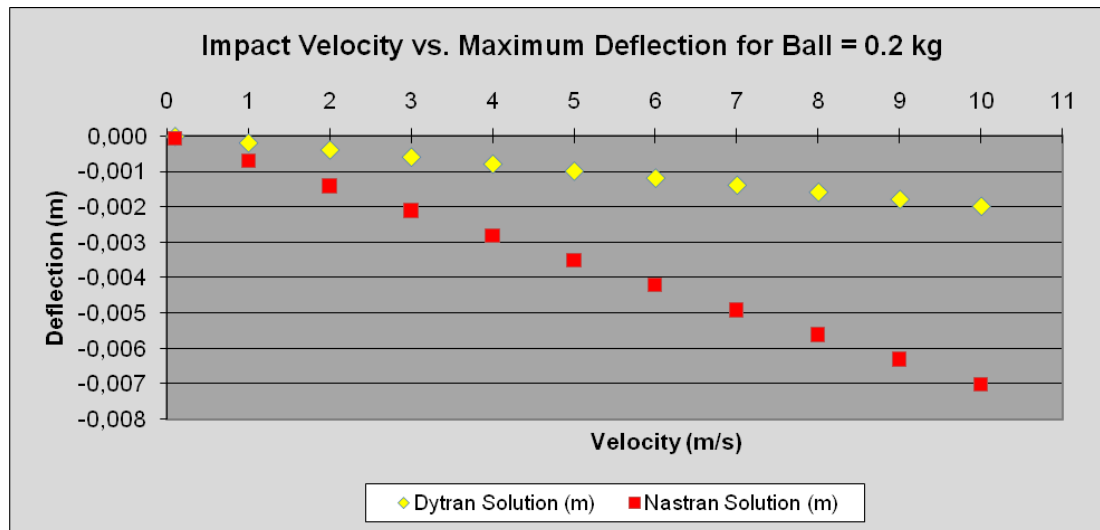


Figure 103: Impact Velocity (m/s) vs. Maximum Deflection Graph (m)